Role of the ground state structural motif in the finite temperature behaviour of small atomic clusters: Born-Oppenheimer molecular dynamics investigations

Thesis Submitted to AcSIR For the Award of
the Degree of
DOCTOR OF PHILOSOPHY
In Chemical Sciences

By
Anju Susan
10CC11A26027

Under the guidance of
Dr. Kavita Joshi

CSIR - National Chemical Laboratory
Pune - 411008, India

CERTIFICATE

This is to certify that the work incorporated in this Ph.D. thesis entitled ***"Role of the ground state structural motif in the finite temperature behaviour of small atomic clusters: Born-Oppenheimer molecular dynamics investigations"*** submitted by **Ms. Anju Susan** to Academy of Scientific and Innovative Research (AcSIR) in fulfilment of the requirements for the award of the degree of ***Doctor of Philosophy***, in ***Chemical Sciences,*** embodies original research work under my supervision. I further certify that this work has not been submitted to any other University or Institution in part or full for the award of any degree or diploma. Research material obtained from other sources has been duly acknowledged in the thesis. Any text, illustration, table etc., used in the thesis from other sources, have been duly cited and acknowledged.

Anju Susan
(Student)

Dr. Kavita Joshi
(Supervisor)

Declaration

I, Anju Susan, hereby declare that this Ph.D. thesis entitled "**Role of the ground state structural motif in the finite temperature behaviour of small atomic clusters: Born-Oppenheimer molecular dynamics investigations**" was carried out by me for the degree of Doctor of Philosophy in Chemical Sciences under the guidance and supervision of Dr. Kavita Joshi, CSIR-National Chemical Laboratory, Pune, India.

I confirm that:

- this work was done wholly by me while in candidature for a research degree at this institution.
- no part of this thesis has previously been submitted for a degree or any other qualification at this institution or any other institution.
- the interpretations put forth are based on my reading and understanding of the original articles and all sources have been duly acknowledged.

Place : . . . . . **Anju Susan**

Date : . . . . . **Research Scholar**

Dedicated to

MY FAMILY, ESPECIALLY TO MY PARENTS

Acknowledgements

I would like to take this opportunity to express gratitude towards my family members, teachers, friends, colleagues and well wishers who have always encouraged and supported me. First and foremost, I would like to offer heartfelt and sincere gratitude to my mentor, Dr. Kavita Joshi. I am grateful to her for believing and introducing me to the field of research. Being her first student, I took quite a bit time to become familiar with the environment. Working on a Linux environment was surprisingly hard for me. Being the only student, I had the opportunity to have one-on-one discussions with Kavita on a daily basis. These meetings helped me immensely, helping me deal with things on my own. I was only able to start off on my path of computational self-learning by dogging her keystrokes. I enjoy spending time with her, and am really grateful for her patience, and valuable guidance throughout my career at NCL.

At the successful completion of my thesis work, I extend my sincere thanks to The Director of CSIR-NCL, Prof Ashwini Kumar Nangia, Dr. Sourav Pal (Former director), Dr. P. A. Joy (Head, Physical and Materials Chemistry Division) and Dr. Anil Kumar (Former Head) for providing me with the opportunity to complete my research in this esteemed institution. I would also like to express my heartfelt gratitude to Dr. Nayana Vaval, Dr. Kumar Vanka, Dr. Sarika Bhattachayrra (DAC members) and Dr. Sudip Roy (Former DAC member) for their constant support and for evaluating my progress during my research tenure.

I am thankful to my first colleague Vaibhav V Kaware, for his support. I am also thankful to my labmates (DIRC), especially Xavier and Aiswarya, for the nice times and conversations have had together. I am thankful to the new members in my group, Shweta, Medhaj, Sameer, Saurabh and Sanchez with whom I enjoyed many moments of frolic, even if it was just for a few months. I am grateful to my friends Sreedhala and Ashok, for being supportive and encouraging me towards doing my Ph.D. I would also like to mention Dr. Vinod, his group members and his family. I really enjoyed all the travelling and other moments I spent with them. It will always be marked as special moments in my NCL life. Thank you for considering me an extension to your group. A special thanks to Vysakh, Sunil, Anneshettan and all those were around since my joining time and Ms. Nita Vinod for the tasty food and nice time we had spent. I am also thankful to all my colleagues, juniors and NCL Malayalee and non-malayalee friends, specially Achu, Nisha chechi, Jaya chechi, Praji, Leena chechi, Kiran and Periz. I would like to use this opportunity to repeat my gratitude to my family members, without whose support this would not have been possible. High regards to all my relatives for being with me through out. Above all I owe all this to the Almighty for showering His blessing and granting me wisdom, health and the fate to undertake research. Thank you for making me the capable being I am today.

Contents

List of Figures

List of Tables

CHAPTER 1

Introduction

1.1 Clusters

Clusters are aggregates of atoms which are intermediate in size between an atom and bulk.[1] They are considerably different from bulk and serve as a bridge between atom and bulk.[2] In comparison to bulk, clusters possess a large fraction of surface atoms. Due to these surface atoms, they display distinct chemical and physical properties, which include, enhanced chemical reactivity, changes in electronic, magnetic, optical and finite temperature properties.[1–4] For instance, bulk gold is a fascinating element for mankind and is popularly used in the area of artwork and jewellery. Gold's resistance to corrosion (chemical reactions) at normal conditions designate it as an inert material. However, experimental investigations demonstrated that gold could be turned into an active catalyst by reducing its size into the nanoscale. For example, metal-oxide supported gold nanoparticles with size ranging from 1 to 10 nm promote low temperature CO oxidation.[5] This is attributed to their large surface-to-volume ratio along with low coordinated surface atoms. Additionally, the changes in their electronic properties, i.e. presence of discrete energy levels have a strong effect on their catalytic activity.[5–7] On a similar note, interesting features were observed when exploring the magnetic behaviour of finite-sized systems. For example, both experimental and theoretical studies illustrated that clusters of Rh, Ru and Pd show magnetic behaviour, while having a non-magnetic bulk counter part.[8–10] These investigations also indicated that the finite-size systems may exhibit enhancement in magnetization, i.e. clusters possess a larger value of magnetic moment per atom.[9–13] For instance, studies on clusters of Ni, Co and Fe, showed that, these systems with a few hundred atoms ($n \leq 400$) exhibit higher values of magnetic moments/atom than their bulk.[13] Moreover, the observed enhancement was higher for clusters with size of about 100 atoms.

These properties show variations with the number of atoms present in the cluster. Based on the

dependence of observed properties with size, the clusters are broadly classified into two regions, as scalable and non-scalable. In scalable region, properties exhibit a monotonic variation with size of the system. Thus, if the size continues to increase in this region, at some point the properties of these particles will saturate to their bulk properties. On the other hand in the non-scalable regime, cluster properties show a non-monotonic behaviour with the number of atoms present in the system. In non-scalable regime, clusters exhibit irregular fluctuations upon changing the size of the system even by a few atoms. The extreme "size-sensitivity" observed in this region, where the addition of even a single atom changes the properties dramatically, motivated many experimental and theoretical studies. All the investigations presented in this thesis are focused on this extreme size-sensitive region.

1.2 Phase transition in clusters

The process of melting in clusters is one phenomenon which exhibits many size-dependent features, and is the main focus of the present studies. For bulk, the transition from solid state to liquid state occurs at a well defined temperature (T_m) and is first-order in nature. Thus, many properties like, volume, enthalpy, entropy, band gap, and density of states, change abruptly at the point of transition, and is indicated by a spike in the heat capacity (C_v) curve of bulk. However in the case of clusters, phase transition is spread over a range of temperatures and is not always first-order in nature.[14] Clusters possess a finite width in their heat capacity curves and depending on the transition, the curves could be broad or sharp in nature.[14, 15] Some clusters are characterised by the presence of secondary features such as, pre-melting (appearance of a small peak/shoulder before the actual melting), post-melting (appearance of a small peak/shoulder after actual melting) or two-step melting peaks in their heat capacity curves.[15] When compared to bulk, a reduction in the melting temperature was observed in theses systems by Pawlow via experimental studies carried out on nanosized particles.[16, 17] The detected depression in melting temperature is attributed to the increase in surface-to-volume ratio. This behaviour was further confirmed by many experimental investigations carried out on nanoparticles.[18–22] However, there exists a few exceptions like small clusters of Ga and Sn, which exhibit elevated melting temperature.[23, 24] Furthermore, in case of clusters, both the melting temperature and the nature of heat capacity curves are highly size-dependent. Thus, a basic phenomenon like phase transition, exhibits distinct features when it occurs in the finite-size region, as compared to the bulk. The main experimental methods employed for the characterisation of the melting process in finite-size systems are reviewed in the following sections.

1.3 Experimental methods

The available experimental methods to characterise the melting process in clusters are classified into two groups, indirect and direct. In the indirect methods, change in some physical properties, such as ionic mobility or diffraction pattern as a function of temperature is used to determine the melting transition. On the other hand, in direct methods, the melting temperatures are measured by probing the internal energy. Initially, most of the investigations were performed on larger and supported clusters. For instance, melting point measurements carried out on gold particles with size around 20 Å by employing scanning electron-diffraction method showed a depression in T_m.[20] In this technique, the diffraction pattern is monitored while heating the sample. The temperature at which the diffracted beam lost the characteristics of a solid structure is considered as the melting temperature. However, with a decrease in particle size, the diffraction technique becomes inaccurate due to the finite-size induced line broadening.[20] The first attempt to determine the melting transition by measuring latent heat of fusion was accomplished by Lai et.al.[22] In this experiment the melting of Sn particles with size ranging from 5 to 50 nm was characterised by employing nanocalorimetric technique.[22] The measurements of melting temperatures of unsupported metal clusters were first performed by Martin et.al.[25] In their method, the disappearance of geometric shell structure in the mass spectra of clusters with heating is considered as the signature for melting process. However, this technique was not able to provide information regarding size-selected clusters.[25] Experimental investigations carried out to probe the finite temperature behaviour of free, size selected clusters relevant to the present investigations are reviewed in the following sections.

1.3.1 Indirect method

Ion mobility experiment is one of the methods to determine the melting transition of unsupported size-selected clusters indirectly. In this method, the solid to liquid transition is characterised by a change in their shape associated with the melting process. The clusters are produced by pulsed laser vaporization of a metal rod (source) in a continuous flow of helium buffer gas. After cluster generation, they are focused into a quadrupole mass spectrometer to select a cluster with particular number of atoms. The size selected cluster ions are then injected into a drift tube, and the ions travel along the length of the drift tube under the influence of a uniform weak electric field. After travelling through the drift tube, some of the ions exit through a small aperture. These ions are directed into another quadrupole mass spectrometer and subjected to detection. Mobilities are measured by recording the arrival time distribution of the size selected clusters at the detector with a multichannel analyzer. The drift tube temperature is variable, so a

series of mobility measurements are performed for different size selected clusters as a function of temperature. Larger relative mobilities imply that the clusters have nearly-spherical structures, whereas smaller values indicate geometries have substantially deviated from spherical. Clusters are expected to adopt a roughly spherical geometry upon melting. Thus, a transformation from highly prolate structure to roughly compact spherical structure is a good indication for the melting process.[26] Hence, this method determines a lower limit for the melting point. For instance, ion mobility measurements are performed on tin cluster cations with size 10–30 atoms.[27] The Sn_n^+ clusters in this size range are found to adopt prolate like geometries.[27] The relative mobilities of these systems are measured at three different temperatures. The study indicated that these tin cluster cations retain their prolate geometries at least upto $\approx$ 555 K. While these systems do not possess a roughly spherical geometry, which is an indication for melting, these investigations concluded that all tin clusters studied here remain solid above the bulk T_m (505 K). In short, the phase-transition is characterised by a drop in the value of relative mobilities associated with the structural change from an elongated one to nearly spherical one. Owing to this, the method is not useful for the clusters with nearly spherical geometries.

1.3.2 Direct method

Experimental techniques to estimate the melting temperature in a direct way, i.e. via heat capacity measurements, are i) temperature dependent photo-fragmented mass spectrum[28] ii) sticking collisions[29] and iii) multicollision-induced dissociation.[30]

In the temperature dependent photo-fragmented method, cluster ions with known temperature are produced and are thermalized by collision with He buffer gas. A quadrople mass spectrometer is used to select a cluster of specific size. This size selected cluster with a known temperature is then irradiated with laser. This cluster undergoes fragmentation by absorbing photons from a laser beam and the fragmentation spectrum is recorded using a second quadrople mass spectrometer. Distribution of peaks in the spectra depends on the internal energy of the cluster, which is the sum of original thermal energy and energy of the absorbed photons. Thus, the fragmentation pattern varies with the internal energy, in turn with the initial temperature of the cluster. Hence, the internal energy is measured by repeating the above procedure as a function of temperature. This allows to calculate change in the internal energy with temperature, i.e. heat capacity of the system. The phase transition of sodium clusters is characterized using this method. The melting temperature is determined from the peak of the heat capacity curve, while the area under the curve gives the value of latent heat. However, the energy of the irradiated photon should be higher than the dissociation energy of the cluster. That is why this method is so far limited to clusters with weak bonds.[28]

In the second approach, the internal energy is determined on the basis of number of atoms

sticking to the cluster. A cluster of a specific size, at a well-characterised temperature is passed through a collision cell containing the vapour of sodium. After each collision, the size (n) of the cluster is increased by one ($n + 1$), thus, the total energy of the system is increased by the collision energy plus dissociation energy. The maximum number of sticking collisions depend on the initial energy. With an increase in temperature the internal energy also increases, and the cluster can withstand less sticking. There will be no more sticking when the attained internal energy prohibits further cluster growth. The number of sticking develops slowly before the phase transition, i.e. at initial temperatures. Though, an abrupt change is observed at the time of phase transition due to the rapid change in the energy which accompanies the process. Since the number of sticking depends on the internal energy, the heat capacity is calculated using the number of sodium atoms that stick as a function of temperature.[29]

In the following texts, the multicollision-induced dissociation method is discussed in detail. The basic principle behind this experiment is represented in a schematic in Fig. 1.1. The internal energy and the heat capacity curve of a solid as a function of temperature is shown in Fig. 1.1(a) and (b) respectively. The internal energy of the bulk increases with temperature in both the solid and liquid region. A sudden jump in the energy observed at the point of melting, leads to the spike detected in the heat capacity curve (See Fig. 1.1b). Thus, measurement of internal energy as a function of temperature will indicate the melting transition. In this technique the internal energy is measured by estimating the dissociation energy as a function of temperature and is illustrated in Fig. 1.1c, shown by the vertical arrows. A sharp drop observed in the value of dissociation energy is considered as the signature for phase transition.

The experimental apparatus used in this method is shown in Fig. 1.2a. In this technique, the cluster ions are produced from a liquid metal target, and are allowed to pass through a temperature variable extension. After thermalization, the clusters exit the extension and are directed into a quadrupole mass spectrometer where clusters with a specific size are selected. The mass spectra of the size selected cluster at a particular temperature is shown in Fig. 1.2b. The size selected clusters are then accelerated, and are directed into a collision cell that contains helium. The ions undergo collisions with the buffer gas in the collision cell and some of them fragment/dissociate. The parent and dissociated ions are analyzed by a second quadrupole mass spectrometer and then recorded as seen in Fig. 1.2c. The amount of fragmentation is monitored as a function of the ion's translational energy (TE) as they enter the collision cell, and the TE for 50% dissociation (TE50%D) is determined from a linear regression (Fig. 1.2d). TE50%D values are then measured as a function of the temperature of the extension (Fig. 1.2e). The heat capacity is proportional to the change in TE50%D divided by the change in temperature. Fig. 1.2f represents the heat capacity curve of a cluster. The comparison of this C_v with that of bulk (Fig. 1.2g) brings out the finite-size induced differences more clearly. In the bulk, melting occurs at a well defined temperature, whereas

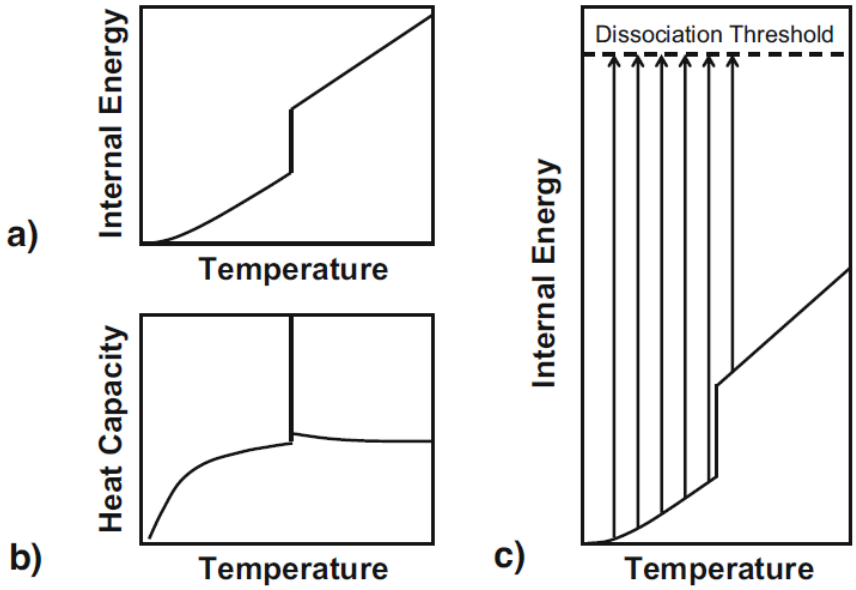

Figure 1.1: *The basic principle behind ion-calorimetry. The internal energy and heat capacity of a typical crystalline solid as a function of temperature are shown in (a) and (b) respectively. (c) Illustrates the method used to calculate the internal energy by measuring the amount of energy required to dissociate the clusters.[30]*

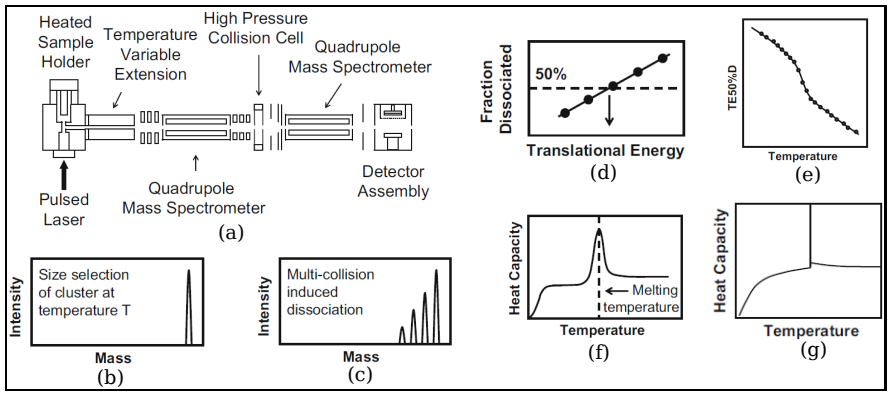

Figure 1.2: *Schematics of the experimental apparatus (a) along with the recorded mass spectra (b and c). The figures (d) – (e) illustrate the different steps involved in measuring heat capacities of isolated cluster ions. The C_v of cluster and bulk is represented in (f) and (g) respectively.[30]*

in clusters the transition is spread over a range of temperatures. Conventionally, the temperature corresponding to the peak in the heat capacity curve is considered as the melting temperature for clusters (dashed line in Fig. 1.2f). Further, a constant value of heat capacity represents both the solid-like (low temperatures) and liquid-like (after the peak) states of the system. The observed rise in the C_v refers to the initiation of melting in clusters, that is the isomerisation process. In this transition region, the solid-like and liquid-like states coexist. Unlike in the temperature dependent fragmented method, this technique is applicable to clusters which are strongly bounded.[30]

1.4 Experimental observations

1.4.1 Melting of sodium clusters

The experimental studies carried out on sodium clusters by employing temperature dependent photo-fragmented method brought out many interesting features regarding the melting process in finite-size systems.[28, 31, 32] The melting temperatures of Na_n^+ ($55 \leq n \leq 357$) clusters as a function of size of the system are presented in Fig. 1.3.[14] The melting temperatures of these clusters are lower by about 30% than that of bulk, which is 371 K. Further, this reduction in melting point does not follow the simple (1/r) rule. The measured melting temperatures exhibit an irregular variation with changing size of the system. The observed size dependent fluctuations are of the

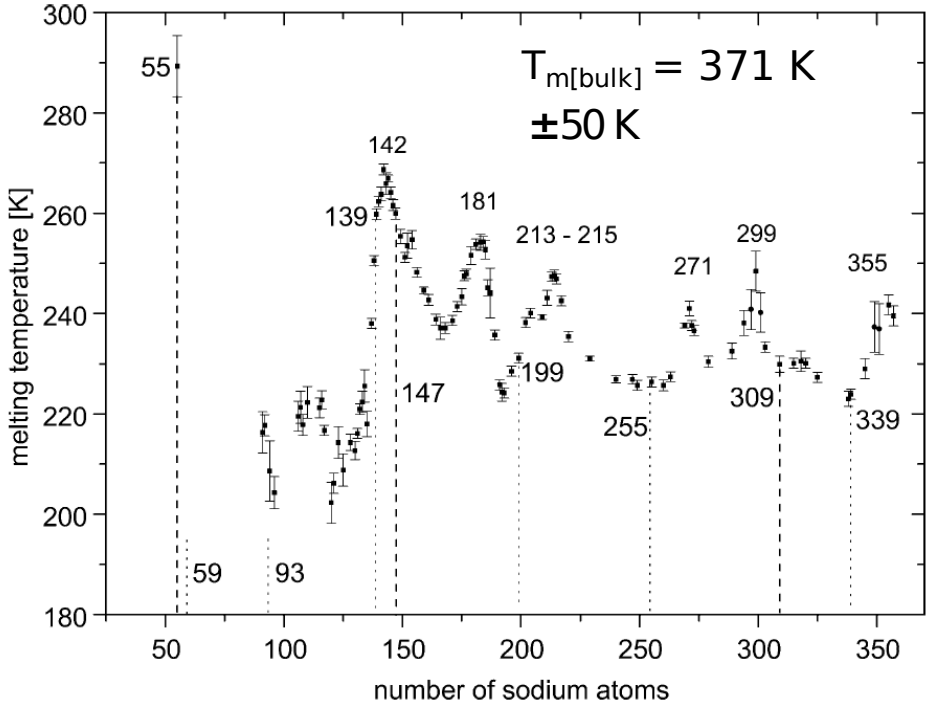

Figure 1.3: *The melting temperatures of Na_n^+ (n = 55 $\leq n \leq$ 357) are plotted against the number of atoms.[14]*

order of $\approx$ 100 K in the size range n = 55 $\leq n \leq$ 357. In the examined region, Na_{55}^+ possesses the highest melting temperature and with increase in size, many local maxima and minima are observed in the plot. The icosahedral structure of Na_{55}^+, which corresponds to the geometrical shell closing, leads to high T_m. On the contrary, higher icosahedra systems with n = 147 and 309 did not coincide with the local maxima in the graph. Moreover, the observed maxima did not concur with the sizes of known electronic shell closing. In electronic shell closure, as proposed by Jellium model, clusters with a total number of electrons equals to 2, 8, 18, 20, 34, ... leads to the

closing of shells imparting stability. Interestingly, it is noted that a few such systems have relatively lower T_m in the examined region, such as sizes with n = 59 (58 electrons) and 93 (92 electrons). Similarly, the higher sized clusters with electronic shell closure, for example Na^+_{139} (138 electrons) and Na^+_{199} (198 electrons) possess low T_m as marked in the graph. Thus, the stability imparted by the geometrical and electronic shell closing does not always led to higher T_m. Moreover, in case of these clusters, the T_m peaks at sizes are between these shell closings. For instance the local maxima at n = 142 is in between 139 and 147, which corresponds to electronic and geometric shell closing respectively. Though, the trend was not observed for larger sized clusters such as n = 181, 271, 299 etc. Thus, the experimental investigations suggested that there is an interplay between the geometric and electronic effects in determining the melting point of these clusters.[31] In addition to this, there are other factors which are responsible for these kind of size-sensitive behaviour. However, those have a complex interdependency with each other. Hence, an atomic level understanding about the process of melting, will help to unravel the observed size dependency in the measured T_m. As discussed later, the available theoretical investigations on these clusters provided a better explanations about the same.

1.4.2 Melting of aluminium and gallium clusters

Multi-collision induced dissociation experiments were performed on clusters of aluminium and gallium to measure the melting temperatures. The interesting observations from these experimental studies on the process of melting of these clusters are discussed in detail.

Aluminium clusters

The measured melting temperatures of aluminium clusters as a function of number of atoms in the system are shown in Fig. 1.4.[15] As expected, all the aluminium clusters exhibit depression in their melting temperatures. Size-dependent variations are noted in case of Al clusters, similar to that of Na. The amplitude of variations in T_m is different for different size ranges and is marked in Fig 1.4. For instance, the amplitude of fluctuations is of the order of 500 K for sizes upto n = 70. However, the value decreases to $\approx$ 100 K with increase in size of the cluster. Moreover, in this examined region, clusters with $n > 120$ do not exhibit a change in their T_m with addition of atoms. Though, further increase in size could result in variations in the T_m, until the system hits the bulk melting temperature (which is not known till date).

The nature of heat capacity curve (size and shape) also exhibits some interesting features which are size-dependent, like the variations in their melting temperatures. The heat capacity curves of aluminium clusters for the size ranging from 16–128 were measured experimentally.[30, 33–35] The main characteristics observed in case of Al clusters are illustrated by representative sizes in Fig.

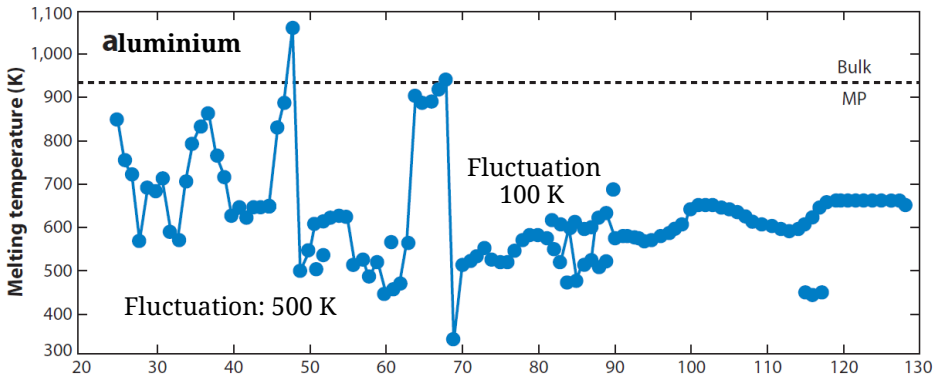

Figure 1.4: *Melting temperatures measured for Al_n^+ (n = 25–128) clusters are plotted as a function of size of the cluster.[15]*

1.5 a–c, where the heat capacity is plotted as a function of temperature. The heat capacity curves of smaller clusters of aluminium with size around 20 atoms, are flat and featureless (represented in Fig. 1.5a). The reason could be one of two; either these clusters do not possess a phase transition, or the melting temperatures may be above the temperature range examined in these experiments. The smallest experimentally probed cluster, with a significant peak in the C_v is Al_{28} (not shown).[33] Interestingly, the addition of a few atoms to the cluster changes the nature of transition from a broader one to a sharper one. For instance, one can notice this behaviour by comparing the C_v

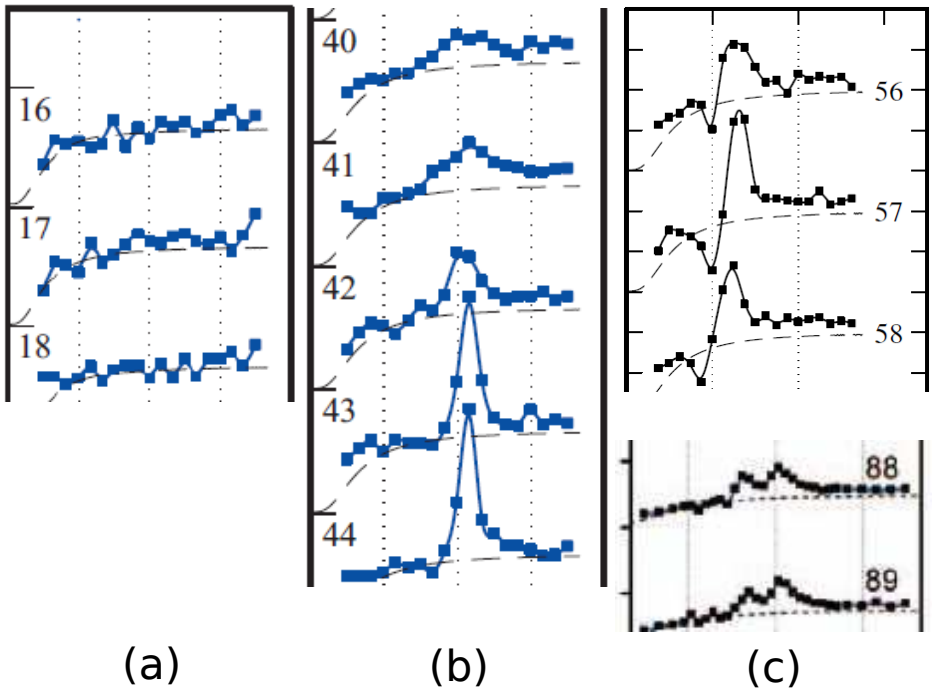

Figure 1.5: *(a)–(c) Main features detected in the nature of measured heat capacity curves of Al cation clusters are pictured using representative sizes.[33, 35]*

of 40 atom cluster (broad) with that of 44 atom cluster (sharp, See Fig. 1.5b). Additionally, a few secondary features like the presence of a dip and two peaks are observed in the heat capacity curves.[35, 36] The appearance of dip in heat capacity curve is noted for a few Al clusters and is represented using sizes n = 56–58 in Fig. 1.5c. Annealing studies carried out in these clusters showed that the dip persists for a few clusters (e.g. 56), but disappear for some other sizes (e.g. 57 and 58). These experimental studies proposed that this feature may be attributed to (i) the transition from an amorphous or badly formed geometry generated during cluster growth to the actual growth (disappearance of dip) or (ii) freezing into a high energy geometry and its conversion into the thermodynamically preferred solid (dip persists).[36] The double peaked C_v observed for Al_n with n = 88 and 89 is not well separated as seen from the lower graph in Fig. 1.5c.[35] The experimental

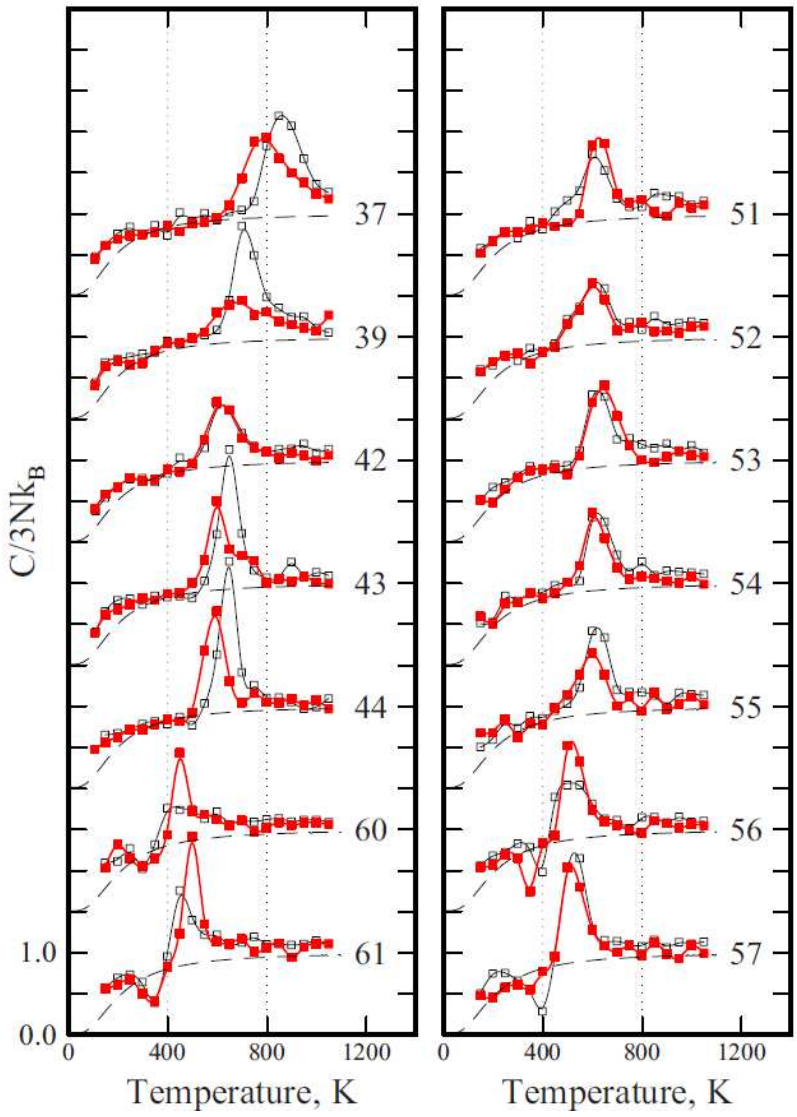

Figure 1.6: *The graph shows a comparison of heat capacities recorded for Al anions (red) and cations (black).[37]*

investigations proposed that the double peak could be the result of either a structural transition or partial melting.[35] The effect of charge on the nature of C_v and the melting temperatures was investigated experimentally for Al clusters and the results are represented in Fig. 1.6.[37] The figure plots the measured C_v of cations (open black points) and anions (filled red points). It is clear that in most cases there exist a substantial differences in the T_m (n = 37, 44), size (n = 56, 61) and shape (n = 51, 57) of the heat capacity curve due to the addition of two extra electrons into the system.[37]

Gallium clusters

Initial experimental investigations carried out on a few Ga_n^+ (n = 17, 39, 40) showed that these clusters melt substantially above the bulk T_m ($T_{m[Bulk]}$).[23] This kind of behaviour was already observed in case of small tin cluster cations.[24, 26] Though the evidence was indirect because, those measurements were performed in an indirect way (Refer Sec. 1.3.1).[26] Further, these experiments could not determine their actual melting temperatures and only showed that, the clusters are stable above their $T_{m[Bulk]}$. Further investigations showed that, those tin clusters dissociate rather than melting.[24] Whereas, in case of these Ga clusters, the experiments were able to measure their melting temperatures.[23] An extended study on the gallium clusters in the size range n = 30–50 and 55, further supported the evidence of elevation in their melting temperatures.[38] Later experimental investigations showed that, gallium clusters which consist of a few tens of atoms (till date n = 160) also exhibit the same behaviour.[39] The variations in measured melting temperatures of gallium clusters as a function of size of the system are shown in Fig. 1.7.[38, 39] The graph clearly indicates the higher than bulk melting temperature observed in these systems. However a depression in T_m is observed for larger sizes in the range $170 \leq n \leq 185$, in the experimentally studied range. The size range under investigation may be grouped into

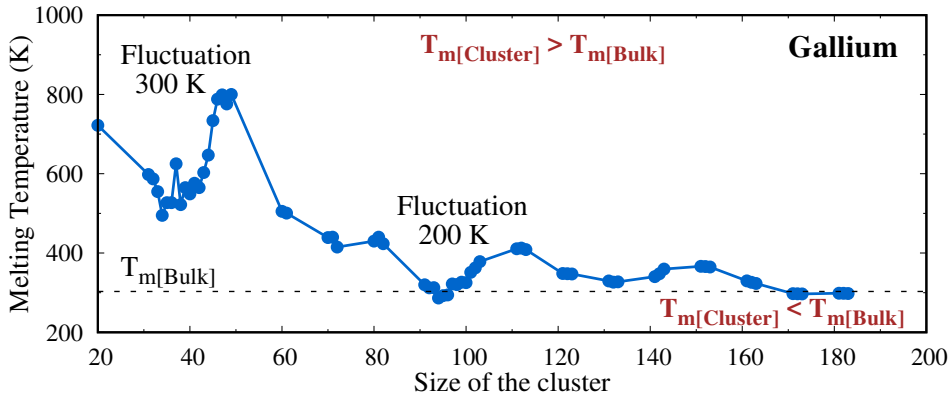

Figure 1.7: *Melting temperatures measured for Ga_n^+ (n = 20–185) clusters are plotted as a function of size of the cluster.[38, 39]*

two, based on the amplitude of fluctuations. Upto a size of $n \leq 55$ the order of noticed variations is $\approx$ 300 K with the addition of a few atoms, much like aluminium. Though, the amplitude of fluctuations for clusters with hundreds of atoms decrease to a value of 200 K. Furthermore, it is observed that adding a few atoms do not change the T_m for clusters with size $170 \leq n \geq 185$. Nonetheless, further addition may lead to depression in melting temperatures.

The main size dependent characteristics in the shape and size of the heat capacity curve of gallium clusters are presented in Fig. 1.8.[38, 39] The overall behaviour is similar to that discussed in aluminium, with subtle differences. For example, in Ga a well-defined transition is seen for a cluster which consists of 31 atoms, in the examined region.[38] Though for Al, a melting transition is detected for cluster with size, $n = 28$.[33] Further, size-sensitivity in the shape of the C_v is clearly seen for small gallium clusters. For instance, with subsequent addition of atoms the melting transition changes from a "non-melter" (Ga_{30}^+: no melting transition) to a "magic-melter" (Ga_{31}^+: sharp transition) to one with poorly defined (very broad) melting transition (Ga_{32}^+).[38] Secondary

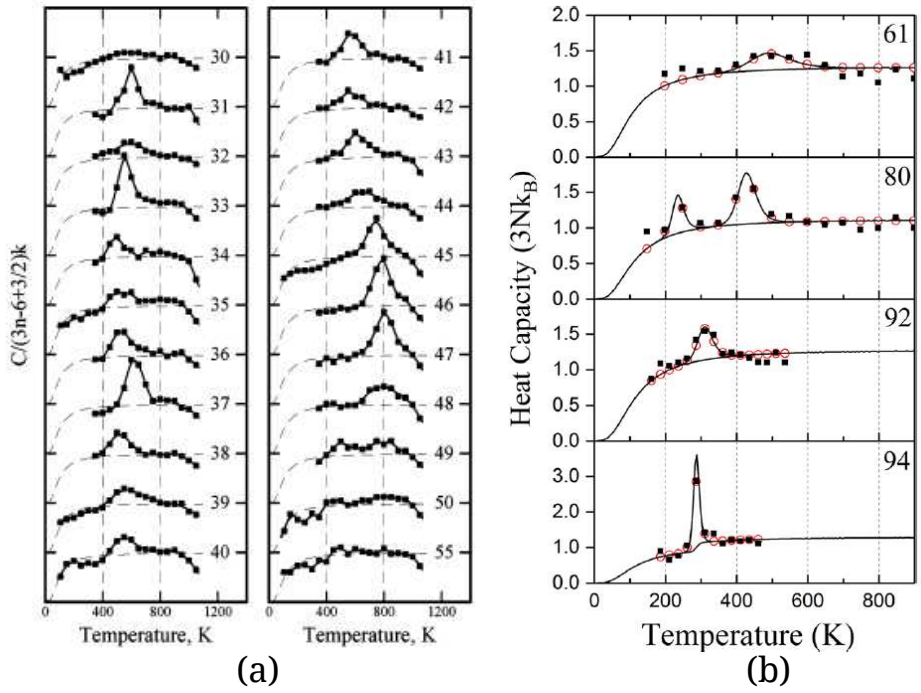

Figure 1.8: *(a): the measured heat capacity curves for Ga_n^+ (n = 30–50,55) clusters. (b): represents the diverse melting behaviours observed in case of gallium clusters in the size range n = 30–183.[38, 39]*

feature like double peaked heat capacity curves is observed for Ga_n (n = 80, 81), though a dip in the C_v is not noted in this clusters. On the contrary to Al, the detected multiple peaks are well separated ($\approx$ 200 K) in nature (see Fig. 1.8b) for gallium clusters.[39]

On similar lines, features like size-sensitive variations in the nature of the heat capacity curve and secondary features (double peaked C_v) were observed for Na clusters, mainly through

simulation studies. The proposed reasons for the double peaked nature are different phenomena like structural transition, surface melting/partial melting etc.[34, 35, 39] That means, to unravel the actual process behind these features, one should understand the process of melting at the atomic level. Further, the transition becomes narrower for (Na, Al and Ga) clusters with size around 100 atoms.[15, 35, 39] In brief, the main characteristics of the melting behaviour of atomic clusters (Na, Al and Ga) investigated by experimental methods may be summarized as follows, size-dependent variations in both the T_m and C_v of the system and the presence of secondary features in the heat capacity curve. Moreover, the charge of the cluster substantially influences the melting process.

1.5 Theoretical investigations

Interesting observations brought out by the experimental studies on the phase-transition of finite-size systems motivated many theoretical investigations. The aim of the theoretical studies was to understand the reasons behind the high size-sensitivity observed in the process of melting of small clusters (non-scalable region). The simulations provided an atomic level interpretation and improved upon the basic understanding of the process. In the early 90's, due to the limited computational power, the phase-transition of clusters were mostly explored using classical molecular dynamics. In classical molecular dynamics, the electronic structure of the system is not treated explicitly, but rather represented with paramaterised potentials. However, the developments in the field of technology made it possible to explore the melting process in clusters by employing *ab-initio methods*, which treat the electronic interactions explicitly. A brief account of phase-transition of atomic clusters, both by classical and first-principle methods is presented in the following sections.

1.5.1 Review on *paramaterised potentials* based simulations

Earlier simulations were performed on aggregates of rare gases, chiefly on argon clusters, using Lennard-Jones (LJ) potential.[40–47] In these studies, some physical properties were investigated as a function of energy or temperature to mark the phase transition. These properties include heat capacity, mean-square bond length fluctuations, diffusivities etc. and all of them show a rapid change with temperature/energy. Thus, the region where a rapid change occurs is characterised as the phase transition region for the system under consideration.[48] Extensive investigations on the meting behaviour of finite-size systems were performed by Berry et.al, by employing empirical potentials and a few models developed in their group. They explored the phase transition on a large variety of clusters such as metal clusters, dielectric clusters, gold

clusters and binary clusters using classical theories.[49–61] These initial studies brought out many interesting phenomena about the melting process in small clusters. These include, observation of depression in melting temperatures, size dependency of the melting temperatures, and a few pre-melting features which are peculiar to finite-size systems. Presence of a dynamical coexistence region is observed through these simulations.[54, 55, 62–70] The coexistence region is defined as a range of temperatures over which the solid-like and the liquid-like phases are stable, while the small systems melt. Thus, the early simulations improved our understanding of the nature of transition in finite-size systems to an extent.

In addition to this, progress in computational techniques have resulted in a larger number of simulations in clusters other than rare gas clusters.[70–87] These developments resulted in an increase in the simulation time of these calculations, which lead to a better understanding of the process. Simulations are available for sodium clusters Na_n, with size upto n = 147.[70, 74, 75] Many features of the melting process of finite-size systems were explored through these studies. It is observed that the phase transition in small sized clusters ($n \approx 100$) is a multi-stage process and is initiated by diffusion of surface atoms. With increase in size, this pre-melting features get much softer and the melting becomes a single stage process with exceptions at medium sizes like n = 133, 135.[70, 74, 75] Similarly, the simulation studies performed on a two-step melter Na_{41}^+ suggested that the pre-melting is likely due to an anti-Mackay to Mackay solid-solid transition. However, the simulated temperatures of both the pre-melting and melting peaks are not matched with that of experimental results.[78] Investigations are also available for aluminium clusters with size around 55 atoms. However, the pre-melting features like dips in C_v observed through the experimental studies are not reproduced in these simulations.[81–83]

Thus, even if these initial investigations assisted in improving our understanding of melting in clusters, none of these studies were able to reproduce the experimentally observed variations in the melting temperature with change in size of the cluster. Further, the melting results observed through these simulations were different both qualitatively and quantitatively depending on the potential used.[81] This is because in most of the cases, the parameters used in these potentials are fitted such that one or more bulk properties could be reproduced. Since the cluster properties are different from their bulk counter part, the potentials which are modeled using bulk features, could not treat the small sized systems. Hence, these parameters failed to reproduce the size specific properties of small clusters.

1.5.2 Review of simulations based on *ab-initio* methods

Advances in computer hardware and algorithms in the last couple of decades, made it possible to investigate the dynamical behaviour of atomic clusters by employing first-principle based

methods. In what follows, we present a brief overview of investigations carried out using density functional theory (DFT) based methods.[87–99] These simulations were able to reproduce the size-sensitive variations in the T_m observed in sodium clusters, unlike the classical ones.[94, 95] Most of these simulations were focused on sorting out the reasons behind the anomalous size dependence observed in the measured T_m.

Minimum energy structure based investigations were available in order to explain the observed size-sensitivity in melting temperatures.[87, 92–96] The MD investigations on representative sizes, such as n correspond to local maxima, electronic and geometrical shell closure pointed out the factors influencing their T_m.[94, 95] The irregular size dependence of T_m is observed through an orbital-free DFT MD performed on a few Na clusters.[94] These investigations illustrated that, high surface stability and compactness in the structure correlate with the local maxima in T_m.[94] Even if these simulations provided a logical explanations for the oscillation pattern, there exists a large discrepancy in the measured (325 K) and simulated T_m (190 K) of Na_{55}^{+}.[94] As noted by the authors, this conflict is due to the negligence of quantum-shell effects. As a result, the features associated with electronic shell closings could not be reproduced.[94] However, Kohn-Sham (KS) based DFT studies on Na_{55}^{+} estimated a melting temperature between 300 and 350 K, which signifies the importance of choosing a good method for calculations.[87, 92]

Detailed thermodynamic behaviour is available for Na_n clusters in the size range n = 8–50, 55, 57, 58, 92 and 142 employed by KS based DFT.[95, 97–99] The experimentally measured melting temperatures for Na_n, n = 55, 92 and 142, are reproduced in these calculations.[95] In addition to this, a systematic and exhaustive growth analysis was reported for the clusters in the size range n = 10–147.[96] These extensive studies pointed out the correlation between the structure of the system and the observed size sensitivity. For instance, the experimentally marked high T_m for Na_{55} and Na_{142} were explained by the presence of icosahedral order in their ground state. Moreover, these studies demonstrated that clusters around n = 92 prefer spherical shape over an icosahedral order (driven by electronic shell closure). Thus the observed low T_m in this size range (Refer Fig. 1.3) is attributed to the absence of local as well as global icosahedral order in the structure.[96] Additionally, calculations indicated that the T_m of Na_{57} and Na_{58} are $\approx$ 350 and 375 K, respectively, that is higher than Na_{55} and Na_{59}.[99] One can compare this with the trend observed in the available experimental data, i.e. the clusters those lie between shell closings possess high T_m (See discussion of Fig .1.3 in pg. 7). On similar lines, here the Na_{57} and Na_{58} are in between 55 (geometrical shell closing) and 59 (electronic shell closing) and exhibit higher T_m. The simulations depicted the structural motif of Na_{57} and Na_{58} (which is driven by electronic shell closing) as spherical in shape. Interestingly, the spherical shape of Na_{58} was supported by experimental studies.[100] Hence, it is possible to verify the prediction of high T_m observed for Na_{57} and Na_{58} with the help of experimental studies. Moreover, theoretical melting studies were available for smaller

clusters in the size range n = 8–50 these were not experimentally probed. These investigations indicated that these clusters display an irregular pattern similar to that which was experimentally observed for larger clusters. Further, the effect of size-sensitivity in the nature of heat capacity was brought out through these simulations.[97–99] For example, it is demonstrated that clusters with ordered geometries are likely to exhibit relatively sharper transition. However, those which possess disordered ones are expected to display broader peaks in their specific-heat curves.[97–99]

In addition to the above discussed analysis, the isomerization and detailed dynamics were investigated in the simulations. Multi stage melting is observed in many of the systems and the processes are attributed to solid-solid transition, diffusion of surface atoms/vacancies and different types of deformations. [92, 93, 101–105] These first-principle based simulations helped refine the results obtained from classical simulations. For instance, in case of Na_{41}^{+}, temperatures were not reproduced in the earlier classical simulations.[78] Though, the first-principle based simulations were able to reproduce the experimentally measured temperatures.[106] Further, the simulation studies on Na_n^q (for n = 40 and 41, q = 0 and $+$, while for n = 39 the $q = -$, 0 and $+$) depicted the effect of charge on the melting.[107] It is showed that a change from anionic to cationic could affect both the shape and melting temperature of the clusters. A similar experimental observation is already discussed for aluminium clusters (See Fig. 1.6). Thus, these simulations on sodium clusters were able to reproduce the observed size-sensitivity in the measured T_m. Further, the studies elucidated the interplay between the geometric and electronic shell closing in melting behaviour.[98, 99] However, it is rather difficult to separate and understand their effects. Hence, this opens up a chance for new investigations and such sort of research is presented in the Ch. 5 of this study.

Moreover, these initial studies on Na clusters motivated to employ quantum based simulations on other atomic clusters.[108–112] Comparative studies of the melting process across the clusters of alkali elements showed that they generally show a surface melting stage prior to the homogeneous melting. Pre-melting effects and the width of the phase transition region are more for heavier alkali clusters. Further, as the atomic number increases the percentage of decrease in the melting temperature is substantially larger.[108] Similarly, investigations carried out on the elements of group-IV clusters like Si, Ge and Sn, showed that their structures are different from that of the bulk and that they exhibit higher-than-bulk melting temperatures.[109] First-principle simulations performed on different Si and Sn clusters (n = 10, 20 and Si_{15}) indicated that these systems exhibit some similarities in their finite temperature behaviour. The simulations depicted that all these clusters undergo fragmentation. However, Si_{20} and Sn_{20} do not show a liquid like behaviour.[110–112]

On the same note, variations in melting temperatures and heat capacity curves with size observed in Al and Ga clusters were investigated through DFT based simulations. The different

size-sensitive behaviour observed for Al clusters in the range 31–48 were explored through simulations.[113] The relatively higher T_m observed for the sizes 35–39 ($\approx$ 900 K) is explained on the basis of higher connectivity present between the core and surface atoms. These investigations also showed that the presence of a less connected and opened structure leads to a broader transition in their curve. While, the clusters with compact and well connected geometries give rise to a narrow peak in their curve.[113]

The role of a low energy structure on the melting temperature was also depicted in another theoretical study.[114] The diversity in the melting behavior of aluminium clusters for sizes 53–57, 64 and 68 were investigated by Kang *et. al* using an *ab-initio* method.[114] A broad transition with a noticeable single peak in the heat capacity curve is observed for clusters of size 53–55. A drop in the melting temperature by a value of 120 K is seen for the neighbour sizes 56–57, and are characterised by a dip in their heat capacity curve. However, the clusters with sizes 64 and 68 do not exhibit a peak in their heat capacity curves. Analysis of minimum energy structures of these systems give an indication of these experimental observations. It is noticed that the symmetry of these structures reduces with increase in size. For instance, a symmetry reduction from T_d to D_{2d} while the size changes from 55 to 56 results in a sudden drop in the melting temperature. Further, symmetry changes from a high symmetry D_{2d} to a low symmetry C_s in case of 64 and 68, based on which the absence of peak is explained. Moreover, these simulations were able to reproduce the observed dip in the heat capacity curve for Al_{57}, which was not obtained through classical studies. Further, the presence of low symmetry meta stable states is explained as the reason for the dip in the curve at low temperature region.[114]

In addition to this, the effect of charge on the process of melting was explored using first-principle simulations.[115–117] Size evolution studies in the clusters of aluminium cations and anions in the size range 34–84 correlate the minimum energy structures with that of the observed T_m variations.[115] The lowest energy structures found through these simulations are grouped into four different types. The calculations showed that the variations in melting temperatures correspond to a change in their structural motifs.[115] Investigations indicated that clusters with same size and structure (differing only in the number of electrons) possess the same melting mechanism. Further, clusters with higher electronic stability melt at a higher temperature and exhibit a well-defined, narrow heat capacity curve.

Additionally, extensive first-principle simulation studies performed on Al_{55} cluster brought out an interesting phenomena.[118] The simulations showed that at a temperature below T_m, the system undergoes spontaneous, collective structural transformations to another solid-like state but with different configurations of surface atoms. This reconstruction of structure is termed as "Half-Solidity", a new form of flexible solid-state. The elementary motions (processes) involved in this 'nanotransformation' were demonstrated in this study. This kind of behaviour at finite

temperatures ("half-solidity") provides an useful insight into the stability, flexibility, and functionality of nanosystems near or below their melting temperatures.[118]

Simulation studies were available to explore the size-sensitivity in the T_m and nature C_v for gallium clusters in the range n = 31–55.[119, 120] Clusters with a defined peak in their heat capacities are termed as "magic melters". Calculations based on *ab-initio* simulations showed that "magic melters" have a geometrical origin.[119] These investigations indicated that Ga_{30} a non-melter, possesses a "disordered" ground state structure. On the other hand, the ground state of a magic-melter like Ga_{31} is an "ordered" one, where the term "order" means that a large number of atoms experience a similar environment in the cluster. Thus, these atoms will "melt" together, giving rise to a well defined narrow peak in the heat capacity curve.[119] In order to explain the fluctuations observed in the melting temperatures of this size range, finite temperature studies were carried out on a few gallium clusters.[120] Investigations on cluster geometries demonstrated that systems with local order exhibit a sharp peak in curve, while otherwise undergoing a broad phase transition from solid-like to liquid-like state. Further, the analysis indicated that strong bonds between core and surface atoms give rise to higher melting temperatures.[120] Even if variations in the nature of heat capacity have been explored thoroughly, the large fluctuations in the melting temperatures were not examined systematically, which calls for the need for more exploration.

Another important and atypical characteristic found in the phase transition of Ga clusters is the elevation in melting temperatures.[23] This higher-than-bulk T_m is also observed through density functional molecular dynamical simulations performed on small gallium clusters (Ga_{17} and Ga_{13}).[121] The nature of bonding present in these small gallium clusters was characterised by performing ELF analysis. This study showed that gallium clusters are covalently bonded, in contrast to the mixture of metallic and covalent bonding in bulk. Thus, the higher than bulk melting temperature is interpreted based on this change in nature of bonding.[121] However, another theoretical study on the ground state of gallium clusters showed that small gallium clusters are structurally more similar to the extended gallium surface, which is metallic in nature.[122] Thus the study concluded that the higher-than-bulk melting temperature of gallium clusters is attributed to this metallic behavior.[122] Similarly, molecular dynamics simulations studies carried out on liquid phase of gallium clusters in the size range n = 32–36 supported this observation.[123] These clusters adopt a flattened-prolate shapes in their liquid-like state, which exhibit a resemblance with that of α-Ga(010) surface. These studies explained the elevation in melting temperature based on the enhanced metallic character observed in clusters, in comparison to that of α-Ga. In conclusion, the explanations for higher melting temperature observed in small gallium clusters are two fold, covalent vs metallic bonding in clusters, in nature. The issue is still under debate and calls for further investigation.

Additionally, the process of phase transition in small clusters with atoms n = 7–12 is examined using first-principle based simulations.[124] The investigations showed that 7 and 8 atom clusters do not exhibit a signature of melting. The simulations also indicated that Ga_{12} represents the first gallium cluster which shows a depression in the melting temperature and melt at a temperature of 178 K. The lower-than-bulk melting temperature of the 12-atom cluster is suggested based on the existence of pair bonding, similar to the pairing observed in α-gallium.[124] Electronic effects on the melting of gallium clusters was also investigated by DFT based molecular dynamics simulations of Ga_{20} and Ga_{20}^{+}.[125] Analysis showed that, cations exhibit a broader peak in heat capacity and melt at a lower temperature than that of neutral cluster.[125]

1.6 Scope of the work: Phase transition in small atomic clusters, current status and open questions

As discussed in the previous texts, developments in the experimental technologies enhanced the generation of small atomic clusters as well the studies of their finite temperature properties. The interesting features observed in the phase transition of small atomic clusters motivated many theoretical investigations. Atomic level understanding about the melting process was improved by these simulations. The controversial observation of elevated melting temperature in small gallium and tin clusters was explored by theoretical methods. This characteristic is attributed to the change in nature of bonding found in clusters compared to that in bulk. Two different arguments are present in case of gallium clusters, as presented in the previous section and the problem is still a paradox. Features like size-sensitive variations in both heat capacity curves and melting temperatures were investigated through the simulation studies. The dependence of phase transition on the low-lying geometry and its properties was examined in various studies and was able to explain many features to an extent.

Even though theoretical calculations played a crucial role in understanding the finite-size effect on phase transition, there are many issues which are yet to be resolved. The high size-sensitivity observed in the measured T_m of small Ga clusters is still a puzzle and need more investigations. Through the extensive studies on Na and Al clusters, the influence of GS structural motif in the process of melting was discussed. Though, there exist other factors like, number of electrons, atoms and the underlying electronic structure which affect the process. All these factors are interdependent in nature, hence, the exact role of GS in the phase transition needs to be explored more. Further, interestingly, a recent experiment on Ga nanoparticles demonstrated that a single 80 nm gallium particle exhibits a distinct phase transition between four different structural states. This opens up a possibility of its usage as a rewritable all-optical quaternary memory

element.[126] Similarly, the presence of two well-separated peaks in the measured C_v of Ga_{80} is proposed to be due to a solid-solid structural transition.[39] In addition to this, one of the first principle simulation study on Al_{55} reported a solid-solid transition in small clusters.[118] Further, in one of our virtual experiments we have also noticed a distinct cage to non-cage structural transition for 12 atom cages, which is accompanied by a significant variation in their HOMO-LUMO gap. Thus, these experiments and simulations emphasize the importance of investigating the finite temperature behaviour of small atomic clusters which could open up their usage in various technological applications.

1.7 Plan of the thesis

Chapter 2: A brief overview of the theoretical framework used for the present calculations is discussed. The basics of Density Functional Theory, the formalism implemented in the simulations are also discussed in the chapter. This includes a discussion concerning the different tools used for characterising the melting transition in the clusters. An overview of different error analysis performed is also stated.

Chapter 3: This chapter deals with the details of the finite temperature studies carried out to explore the fluctuations observed in small gallium clusters with size n = 31–48. The growth pattern of small positively charged gallium clusters is investigated to understand the observed variation in T_m. The correlation with change in their GS structural motif and the size-sensitivity by analysing various ground state and finite temperature properties is elucidated.

Chapter 4: The diverse behaviour observed while Ga clusters melt are explored by simulating representative Ga systems. The role of GS structural motif in the process of melting is investigated in this study. Characteristics like sharp vs broad transition and high vs low T_m are explained through these simulations. Extensive isomer analysis carried out on these clusters explained the broad vs sharp transition. An analysis of distribution of short bonds in the clusters spelled out the high vs low T_m.

Chapter 5: The change in the GS structural motif and its influence on the process of melting are illustrated in previous studies. Though, in previous cases, a structural change is associated with a change in the number of atoms, electrons, and the underlying electronic structure. Owing to their interdependencies it is a challenging task to rationalize the exact role of GS in the phase transition. However, through this work the role of GS motif in the phase transition is demonstrated using a unique pair of clusters (Ga_{36} and Al_{36}). These clusters have the same number of atoms, valence electrons, and similar GS structural motif. The only difference is, they melt at temperatures which differ by 300 K. An extensive BOMD simulations brought out that, the isomers accessible before the melting are similar and are structurally analogous to that of the GS motif.

Chapter 6: This chapter presents an extensive analysis of the thermodynamic process of Pb_n clusters in the size range, n = 16–24. This study demonstrated that all these clusters undergo fragmentation. Some interesting phenomena like restricted diffusion, solid-solid structural transition, and half-solidity exhibited by these clusters are brought out by these finite temperature simulation studies. The interrelation between the structural motif and its properties with these features is explained.

Chapter 7: Investigations performed as a function of temperature in twelve atom nano cages, Sn_{12}^{2-} and Pb_{12}^{2-}, are presented in this chapter. The study brought out that these cage like structures are highly stable and exhibit an interesting phenomenon at a particular temperature, termed as transition temperature. At this temperature, these cages swap between a cage and non-cage like structure which is accompanied by a substantial change in their HOMO-LUMO gap.

Chapter 8: Conclusions of the present studies and the future scopes are presented in this chapter.

CHAPTER 2

Theoretical Background

The theoretical framework used for the present calculations is discussed in this chapter. A brief overview of Density Functional Theory (DFT), pseudopotentials, plane wave basis set and Born-Oppenheimer Molecular Dynamics (BOMD) is described in the following sections. A detailed description of these formalisms are available in the literature [127–130]. A discussion of different indicators used for data analysis as well as error analysis is presented in this chapter.

The total energy operator Hamiltonian for a system of 'n' electrons and 'M' nuclei is:

$$\hat{H} = -\frac{\hbar^2}{2m_e}\sum_{i=1}^{n}\nabla_i^2 - \frac{\hbar^2}{2M_I}\sum_{I=1}^{M}\nabla_I^2 + \sum_{i=1}^{n}\sum_{I=1}^{M}\frac{Z_I e^2}{\mid r_i - R_I \mid} + \sum_{i=1}^{n}\sum_{j>i}^{n}\frac{e^2}{\mid r_i - r_j \mid} + \sum_{I=1}^{M}\sum_{J>I}^{M}\frac{Z_I Z_J e^2}{\mid R_I - R_J \mid} \tag{2.1}$$

where the terms represent the kinetic energy (K.E.) of electrons, kinetic energy of nuclei, electron-ion interaction, electron-electron interaction and ion-ion interaction respectively. This equation is a multicomponent many-body system, making its quantum mechanical solution impractical. Furthermore, the electron-electron interaction term does not allow the factorisation of the complete wavefunction. One important approximation which decouples the electronic degrees of freedom from that of nuclei is Born-Oppenheimer (BO) approximation.[131] This approximation is based on the significant difference between the masses of nuclei and electrons. Since nuclei move much slower due to the large mass associated with them, the whole system can be considered as electrons moving in the field of fixed nuclei. The uncertainty in the position of nuclei is small, so considering nuclei as stationary while describing the electronic state of a molecule is justifiable. This means that as the nuclei follow their dynamics, electrons instantaneously adjust their wavefunctions according to the nuclear wavefunction. This allows the separation of the full wavefunction into electronic and nuclear wavefunctions, where the electronic wavefunction depends parametrically on the nuclear wavefunction. The simplified Hamiltonian of

electrons after applying the Born-Oppenheimer approximation for a fixed nuclear configuration is,

$$\hat{H}_{el} = \hat{T}_{el} + \hat{V}_{el-Nu} + \hat{V}_{el-el} + V_{Nu-Nu} \tag{2.2}$$

where, T_{el} is the kinetic energy of the electrons,

$$\hat{T}_{el} = \sum_{i} -\frac{1}{2}\nabla_i^2, \tag{2.3}$$

$\hat{V}_{el-Nu}$ is the potential acting on the electrons due to the nuclei,

$$\hat{V}_{el-Nu} = \sum_{i=1}^{n}\sum_{I=1}^{M} \frac{Z_I e^2}{\mid r_i - R_I \mid}, \tag{2.4}$$

$\hat{V}_{el-el}$ is the electron-electron interaction,

$$\hat{V}_{el-el} = \frac{1}{2}\sum_{j>i} \frac{1}{\mid r_i - r_j \mid}. \tag{2.5}$$

The term V_{Nu-Nu}, which includes the nucleus-nucleus interaction is only a classical additive term in electronic structure calculations.

The electronic energy of the system is the expectation value of the Hamiltonian,

$$E_{el} = \frac{\langle \Psi | \hat{H}_{el} | \Psi \rangle}{\langle \Psi | \Psi \rangle} \tag{2.6}$$

Since electrons are fermions, the Ψ must be antisymmetric with respect to the exchange of two electrons. Even with the Born-Oppenheimer approximation, finding the solution of the Schrödinger equation for 'n' interacting electrons is difficult, due to the electron-electron interaction term. In other words, the exact solution for any system with more than one electron is not known till date. Further approximations/theories have been introduced allowing total energy calculations of multi-electron systems to be performed in a more accurate and efficient way. The chief methods are either based on electronic wavefunction or electronic density (ρ). Among the available approximations, the principle behind density functional theory implemented in the present calculations is discussed in the next section.

2.1 Density Functional Theory

In density functional theory, the basic variable used for calculation is electronic density. In wavefunction based methods the electronic wavefunction is the basic variable. The replacement of '3n' dimensional Ψ (three spatial variables for each of the 'n' electrons) with '3' dimensional electron density reduces the computational expenses. This idea (electronic density as a fundamental variable) was first proposed by Thomas and Fermi. Even though the model was inaccurate for most applications, it laid the basis for the later development of density functional theory.

In 1964, Hohenberg and Kohn proposed and proved two theorems which laid down solid mathematical foundation to the idea of DFT.[132] The first theorem states that the external potential V_{ext} is (to within a constant) a unique functional of $\rho(r)$. This means that the ground-state density $\rho(r)$ uniquely determines the potential (up to an arbitrary constant) hence, energy is a functional of density $E[\rho]$.

The second theorem states that for any positive trial density $\widetilde{\rho}(r)$, such that $\int \widetilde{\rho}(r)d(r)$ = N then $E[\widetilde{\rho}] \geq E_0$. Where E_0 is the ground state energy and is given as,

$$E_0 = E[\rho] = F[\rho] + \int d^3(r) V_{ext}\rho(r) \tag{2.7}$$

The first term in Eq. 2.7 $F[\rho]$ is the universal functional which explicitly depends on the kinetic and potential energy of a system of interacting electrons. This quantity depends only on the electronic density and is defined as,

$$F[\rho] = T[\rho] + E_{ee}[\rho] \tag{2.8}$$

Thus by the second theorem,

$$F[\widetilde{\rho}] + \int d^3(r) V_{ext}\widetilde{\rho}(r) = E[\widetilde{\rho}] \geq E[\rho] \tag{2.9}$$

this is nothing but the variational principle.

In Thomas-Fermi model, the K.E. is expressed in terms of local density of a system. As a result, it fails in many cases such as in systems with bound states. In 1965, Kohn and Sham proposed a new concept in order to approximate the K.E. term.[133] In this formalism, the system of many-electron problem is replaced by a system of non-interacting (one-electron equations) electrons moving in an effective (KS, v_s) potential due to all other electrons. The KS K.E. is given by,

$$T_s[\rho(r)] = \sum_i^N -\frac{1}{2}\int \psi_i^*(r_1)\nabla^2\psi_i(r)dr \tag{2.10}$$

where $\psi_i(r)$ is the single-particle orbital and the density is given by:

$$\sum_{i=1}^{N} \mid \psi_i(r) \mid^2 = \rho(r). \tag{2.11}$$

The total energy equation of non-interacting reference system moving in an effective potential is

$$[-\frac{1}{2}\nabla^2 + v_s(r)]\psi_i(r) = \varepsilon_i \psi_i(r) \tag{2.12}$$

where v_s is Kohn-Sham potential as follows:

$$v_s(r) = v_{ext}(r) + v_J(r) + v_{xc}(r) \tag{2.13}$$

The exchange-correlation potential v_{xc} is the functional derivative of the exchange-correlation energy E_{xc} with respect to the density and is given as:

$$v_{xc}[\rho(r)] = \frac{\delta E_{xc}}{\delta \rho(r)} \tag{2.14}$$

The total energy functional, renamed as $E_{KS}[\rho]$ by including all these terms can be expressed as follows:

$$\begin{aligned} E_{KS}[\rho] &= T_s[\rho(r)] + E_{ie}[\rho(r)] + E_J[\rho(r)] + E_{xc}[\rho(r)] \\ &= \sum_{i}^{N} -\frac{1}{2}\int \psi_i^*(r_1)\nabla^2\psi_i(r)dr + \int dr\rho(r)v_{ext}\rho(r) \\ &+ \int\int dr dr^{'} \frac{\rho(r^{'})}{\mid r - r^{'} \mid} + \int \rho(r)E_{xc}dr \end{aligned} \tag{2.15}$$

The remaining part of the true K.E. is included in the unknown correlation part of the system (E_{xc}). This means that the crucial part in calculation of the total energy of a system is the correct formulation of E_{xc}. The accuracy of density functional theory solely depends on the approximations to E_{xc}. There are ongoing efforts to construct better functionals for expressing this quantity. A few main approximations available for E_{xc} are presented in the next section.

Exchange and correlation

Local Density Approximation (LDA): This approximation simply depends upon the value of ρ at each point in space. In this theory the exchange-correlation functional of a system is constructed in a manner that the E_{xc} per electron at a point r is equal to that of a

homogeneous-electron gas that has the same ρ, and is given by:

$$E_{xc}[\rho(r)] = \int \rho(r)\varepsilon_{xc}(\rho)dr \tag{2.16}$$

This is best applied to solids that are similar to a homogeneous gas, and is usually good in reproducing bondlengths. However, in case of weaker bonds LDA overestimates the binding energy. The first approach proposed to improve LDA was generalized gradient approximation.

Generalized Gradient Approximation (GGA): In this approximation E_{xc} is expanded as a series in terms of the density and gradients, and is expressed as follows:

$$E_{xc}[\rho(r)] = \int \rho(r)\varepsilon_{xc}(\rho, \nabla\rho)dr \tag{2.17}$$

GGA gives reasonably good results for systems in which density varies by small degrees in space. This approximation modifies the LDA by locally introducing features of inhomogeneity in the system. The most used exchange-correlational functionals in GGA are BP, BLYP, PBE etc. GGA approximations were able to improve upon the calculated bond energies and bond lengths. They were capable of better handling weakly bonded (hydrogen bond) systems. However, there were a few problems related to band gap calculation, dielectric constant and lattice constants of noble metals etc.

Hybrid functionals: These approximations combine a portion of exact exchange from Hartree-Fock theory with exchange and correlation from other sources. e.g. B3LYP, PBE0, B98 etc.

2.2 Pseudopotential

To an extent, the above discussed method (DFT) and further approximations to it, reduced complexity of problems. However the implementation of pseudopotentials helped reduce the complexity further. In this formalism, all electrons are divided into two different sets, core and valence. This concept was introduced based on the knowledge that core electrons which are strongly bound to the nucleus do not participate in chemical bonding. Further, physical properties mainly depend on valence electrons. Hence, core electrons alongside the nucleus could be considered as an inert core. The pseudopotential approximation is based on this assumption. In this model strong nuclear potential and core electrons are replaced by an effective interaction called as pseudopotential which is weak and acts on a set of pseudo wavefunctions. The schematic of the principle behind this approximation is represented in Fig. 2.1. Usually these pseudopotentials are constructed to reproduce the scattering properties of the full ionic potential. The core and valence wavefunctions are mutually orthogonal. In order to maintain this

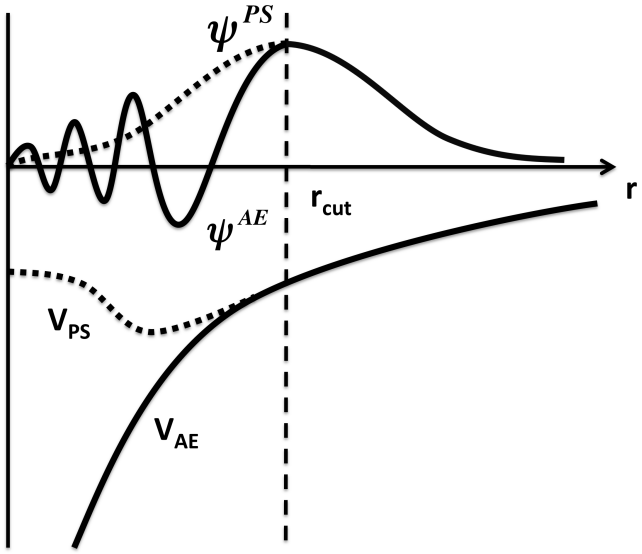

Figure 2.1: *Comparison of all electron (black thick graph) potential and wavefunction with pseudo (black dotted graph) potential and wavefunction.[128]*

orthogonality the valence wavefunctions oscillate rapidly in the region occupied by the core electrons. The pseudopotentials are constructed in such that there are no radial nodes in the pseudo wavefunctions in the core region. Moreover, the pseudo wavefunction and pseudopotential are identical to the all electron wavefunction and potential outside a cut-off radius (r_{cut} in the Fig. 2.1, outside the core region), where the two potentials (V_{AE} and V_{PS}) are identical. The most common pseudopotentials used for calculations are:

Norm-conserving Pseudopotentials: Norm-conserving pseudopotentials are constructed in such a manner that, (i) the norm of each pseudo wavefunction is identical to its corresponding all-electron wavefunction inside the cut-off radius (r_{cut}). (ii) All-electron and pseudo wavefunctions are identical outside the cut-off radius. This condition ensures the correct reproduction of the scattering properties. (iii) The logarithmic derivatives of the all-electron and pseudo wavefunctions agree at r_{cut}.

Ultrasoft Pseudopotentials (USP): In this scheme pseudo wavefunctions are allowed to be as soft as possible within the core region, so that the r_{cut} energy can be reduced effectively. This modification is attained by introducing a generalized orthonormality condition. Ultrasoft pseudopotentials are much softer than norm-conserving potentials. The USP generation algorithm guarantees good scattering properties over a pre-specified energy range, which results in much better transferability and accuracy of pseudopotentials.

Projector Augmented Wave method (PAW): In this method, the valence electron wave

functions are kept orthogonal to the core state. The core functions are treated using muffin-tin spheres. In this approach, the rapidly oscillating valence wavefunctions transform into smooth wavefunctions which are more computationally convenient, providing a way to calculate all-electron properties. Generally PAW potentials are more accurate than ultrasoft pseudopotentials since PAW potentials reconstruct the exact valence wavefunction with all the nodes in the core region.

2.3 Plane wave (PW) basis set

Basis sets are series of known functions introduced to represent KS orbitals. Localised and plane wave basis sets are two commonly used basis sets. All the computational studies presented here are based on plane wave formalism. Both these methods have their own advantages and disadvantages. Even if the localised basis sets are efficient and easier to compute, the functions are not mutually orthogonal. In addition to this, the representation of electron probability is poor both near and far away from the nucleus, also possessing a Basis Set Superposition Error (BSSE). On the contrary in plane wave formalism the electronic wavefunctions expanded in terms of discrete plane waves are orthogonal and do not possess BSSE. Additionally, the implementation is easy (FFT) and allows a systematic convergence, while also being useful for periodic systems. The quality of PW basis set can be adjusted using a single parameter, the cut-off energy. Since plane waves are delocalised, the error due to Pulay forces is absent compared to localised basis sets, also being more efficient for neutral systems. However, in this formalism vacuum costs the same as matter and is hard to converge for systems with tight-orbitals (3d). A huge number of PWs are required to describe the localized features.

2.4 Born-Oppenheimer Molecular Dynamics (BOMD)

Molecular dynamic simulation is a method by which one derives the atomic trajectories of a system of 'N' particles by the numerical integration of Newton's equations of motion for a specific interatomic potential. The forces acting on each particle at a given time are computed from interatomic potentials which represent the potential energy of the system for a specific geometric arrangement of particles. The current positions and velocities will be updated by these calculated forces to generate new positions and velocities. Accordingly, the forces will also be updated using the new positions, with these steps repeating. Thus, the simulations produce atomic trajectories which describe the progress of the system with time.

In classical MD, parameterised interatomic potentials (force-fields) are used to describe the system and to compute forces. These force fields possess a predefined functional form for the

potential and contain many parameters fixed in accordance with experimental data or theoretical calculations. These calculations are fast and are able to treat larger systems (several thousands atoms), but the electrons are not treated explicitly. Hence, they failed to describe processes where electronic degrees of freedom play an active role. However, quantum theory based MD simulations which describe the electrons, overcame the limitations of force-field based MD studies. In this method systems are described using quantum mechanical methods like DFT.

In Born-Oppenheimer molecular dynamics, the forces for the dynamics of ions are derived from the total electronic energy using Hellman-Feynman theorem as follows;

$$\begin{aligned} F_I &= -\nabla_I \langle \Psi_0 | H_{el} | \Psi_0 \rangle \\ &= \langle \nabla_I \Psi_0 | \, H_{el} \, | \Psi_0 \rangle - \langle \Psi_0 | \nabla_I H_{el} | \Psi_0 \rangle - \langle \Psi_0 | \, H_{el} \, | \nabla_I \Psi_0 \rangle \\ &= - \langle \Psi_0 | \nabla_I H_{el} | \Psi_0 \rangle \end{aligned} \tag{2.18}$$

and the ions are moved accordingly. For this new configuration, the total electronic energy and the new forces on the ions will be computed by solving the KS equation (See Eq. 2.15) self-consistently. These calculations are then repeated. Thus, in this formalism the electronic structure problem is repeatedly solved self-consistently for a given set of configurations of nuclei. In other words, electrons are allowed to fully relax and reach its minimum energy configuration for given positions of nuclei (BO surface). The basic equations for BO dynamics are,

$$E_0 \Psi_0 = H_{el} \Psi_0 \tag{2.19}$$

$$F_I = M_I \frac{d^2 R_I}{dt^2} = -\nabla_I \min_{\Psi_0} \langle \Psi_0 | H_{el} | \Psi_0 \rangle \tag{2.20}$$

All molecular dynamics simulations described in the present investigations were performed by implementing Vienna *Ab-initio* Simulation Package (VASP). VASP computes an approximate solution to the many-body Schrödinger equation within the DFT framework. In VASP, the interactions between valence electrons and ions are described using norm-conserving or ultrasoft pseudopotentials, or the projector augmented wave method as discussed earlier. Further, one-electron orbitals are expressed using plane wave basis sets.[134–140]

2.5 Techniques used for Data Analysis

The theoretical framework behind these performed simulations is discussed in the previous sections. Different analysis tools used to extract data from simulation trajectories and output files are discussed in this section. Various techniques are used for characterising the phase transition in finite size systems (both qualitative and quantitative) and explaining the nature of bonding.[141,

142] Mean square displacement (MSD) and root mean square bond-length fluctuations (δ_{rms}) are the qualitative parameters used to characterise transitions. The heat capacity curve which quantifies the transition is computed by implementing multiple histogram (MH) technique.

2.5.1 Mean square displacement (MSD)

Mean square displacement indicates the displacement of an atom in the cluster as a function of time, and is defined as,

$$\langle r^2(t)\rangle = \frac{1}{N_a M}\sum_{m=1}^{M}\sum_{I=1}^{N_a}[R_I(t_{0m}+t) - R_I(t_{0m})]^2 \tag{2.21}$$

where, t represents a time delay, The average is performed over N_a ions and over M time origins t_{0m} taken at regular intervals throughout a molecular dynamics simulation.[141] In solid-like region the atoms oscillate in their equilibrium positions, which results in negligible displacement of atoms. However, in liquid-like regions the atoms diffuse throughout the cluster and exhibit a saturated value. Whereas in the transition region, where the system hops between the solid-like and liquid-like state, the MSD rises with time.

2.5.2 Root mean square bond-length fluctuations (δ_{rms})

Root mean square bond-length fluctuations (δ_{rms}) is a measure of fluctuations in the bondlengths averaged over all atoms and total time span. It is defined as,

$$\delta_{rms} = \frac{1}{N}\sum_{i>j}\frac{\left(\langle r_{ij}^2\rangle_t - \langle r_{ij}\rangle_t^2\right)^{1/2}}{\langle r_{ij}\rangle_t}, \tag{2.22}$$

where N is the number of particles in the system and r_{ij} is the distance between the particles i and j. $\langle ...\rangle_t$ denotes a time average over the entire trajectory. The schematic of a typical behaviour of δ_{rms} as a function of temperature for atomic clusters is presented in Fig. 2.2. For a typical δ_{rms} plot, there are three distinct regions for a finite size system i) solid-like region ii) transition region iii) liquid-like region. In solid-like and liquid-like region δ_{rms} increases linearly, whereas in the transition region the system hops from one phase to another, resulting in large fluctuations. In case of solids, a value > 0.1 indicates the liquid state while this is not the case for finite size systems. For clusters, a value of $\delta_{rms} < 0.05$ denotes the solid-like state. An isomerisation region is seen above this value. In clusters it is observed that for liquid-like state the δ_{rms} saturates to a value of 0.2. Though, the present investigations in this thesis showed that a value of 0.2 does not always correspond to liquid-like state. A detailed discussion related to the shortcomings of δ_{rms} to

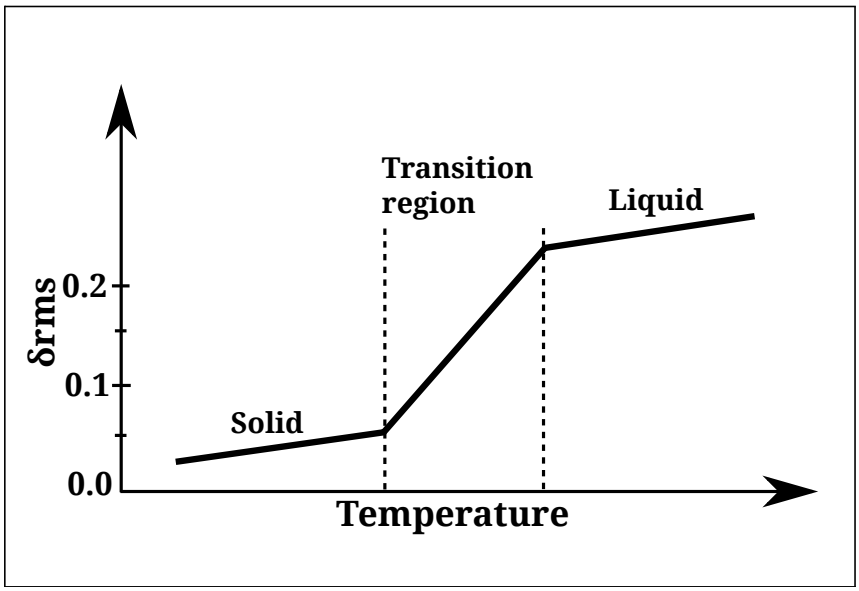

Figure 2.2: *Schematic plot for the behaviour of δ_{rms} as a function of temperature in case of clusters.*

characterise the melting in finite size systems is presented in 6.3.2 (See pg. 82).

2.5.3 Multiple histogram (MH) technique

The above discussed parameters are qualitative in nature and the changes in their values with temperature/time indicate the transition in a qualitative way. However, it is useful to calculate other thermodynamic quantities like entropy and specific heat to characterise the melting transition in a quantitative way. In theory, for a better estimation of the thermodynamic properties of a system one should perform a series of simulations over a range of temperatures those are close enough for a longer time. However in practice, since finite temperature simulations are computationally expensive the number of simulations performed must be optimal. Hence, we need a technique which will reliably interpolate the behaviour of a system, while minimizing the number of simulations to be carried out. Multiple histogram technique is one such method to interpolate the behaviour in intermediate temperatures. It is also able to calculate the entropy and heat capacity of the system by extracting the classical density of states ($\Omega_C(E)$.

For a given finite number set of data of some physical quantity, e.g., N_i potential energies per temperature and τ temperatures, we would like to interpolate reliably the values over a range of temperatures including the ones for which the simulations have not been carried out. The contribution of a point in the phase space of a system to the statistical quantity being observed is, in the canonical ensemble, proportional to the Boltzmann factor at that temperature. Hence, given a data point from the simulations of one temperature point, its contribution at another temperature would be proportional to $exp^{(\beta(E-E_0))}$. This observation is the basic approach to extract an

estimate of the classical density of states.

The first step in extracting $\Omega_C(E)$ is to construct a histogram of the potential energy at each of the τ temperatures used for the sampling runs. For this purpose, the potential-energy scale, which ranges from V_0 to some maximum observed value V_{max}, is divided into N_V intervals (or bins) of width δV = (V_{max} - V_0)/N_V. The same bins should be used for all temperatures. Each temperature is denoted by an index i satisfying $1 \leq i \leq \tau$, and each bin by an index j satisfying $1 \leq j \leq N_V$, with V_j the central value of the potential energy in the j^{th} bin.

The number of times the potential energy assumes a value lying in the j^{th} bin at a temperature i is termed as n_{ij}. Then, the probability that the system takes a potential energy in the j^{th} bin at an inverse temperature β_i = 1/($k_B T_i$) is estimated from the simulation as follows:

$$p_{ij}^{sim} = \frac{n_{ij}}{\sum_j n_{ij}} \tag{2.23}$$

On the other hand, the theoretical probability is given as,

$$p_{ij}^{theo} = p(V_j, T_i)\delta V = \Omega_C(V_j)\delta V \frac{exp(-\beta_i V_i)}{Z_C(\beta_i)}, \tag{2.24}$$

where $Z_C(\beta_i)$ is the canonical partition function at temperature T_i, required for normalization. Equating p_{ij}^{sim} and p_{ij}^{theo} and taking logarithms yield,

$$S_j + \alpha_i = \beta_i V_j + ln p_{ij}^{sim}, \tag{2.25}$$

where

$$S_j = ln[\Omega_C(V_j)\delta V], \tag{2.26}$$

$$\alpha_i = -ln Z_C(\beta_i). \tag{2.27}$$

So, Eq. 2.25 is a system of equations whose right-hand side is known and left-hand side is unknown. Since we have τN_V equations but only $N_V + \tau$ unknowns, this system is over-determined. We therefore solve it in a least-squares sense. Thus, from Eq. 2.25, we are led to choose S_j and α_i such as to minimize

$$\chi = \sum_{ij} \frac{(W_{ij} - S_j - \alpha_i)^2}{(\delta W_{ij})^2}, \tag{2.28}$$

where,

$$W_{ij} \equiv \beta_i V_j + ln p_{ij}^{sim} \tag{2.29}$$

and δW_{ij} is the statistical error in the quantity W_{ij}. From Eq. 2.29 this error satisfies

$$\delta W_{ij} = \frac{\delta p_{ij}^{sim}}{p_{ij}^{sim}} \approx c n_{ij}^{-1/2} \tag{2.30}$$

where c is an unimportant constant. Putting together Eqns. 2.28, 2.29, 2.30, final least-squares problem is thus to minimize

$$\chi = \sum_{ij} n_{ij} (\beta_i V_j + ln p_{ij}^{sim} - S_j - \alpha_i)^2 c n_{ij}^{-1/2} \tag{2.31}$$

with respect to S_j and α_i, which requires solving the linear equations $\partial\chi/\partial S_j$=0 and $\partial\chi/\partial\alpha_i$=0 for S_j and α_i. The S_j gives us the configurational density of states (Eq. 2.26), while the α_i gives us the configurational partition function (Eq. 2.27). Using these we can compute the partition function, internal energy, and the specific heat as follows:

$$Z(T) = \sum_{j=1}^{N_v} exp(S_j - \frac{V_j}{T}) \tag{2.32}$$

$$U(T) = \frac{3T(n-1)}{2} + \frac{1}{Z} \sum_{j=1}^{N_v} exp(S_j - \frac{V_j}{T}) V_j \tag{2.33}$$

$$C_v = \frac{3(n-1)}{2} + \frac{1}{T^2} (\langle V^2 \rangle - \langle V \rangle^2) \tag{2.34}$$

where $\langle V \rangle = U(T)$

2.5.4 Electron Localization Function (ELF)

The nature of bonding between atoms in atomic clusters is investigated using electron localization function. It is a useful tool to analyse the bonding present in atomic clusters, in association with the charge density and molecular orbitals. For a single determinantal wave function built from the Kohn-Sham orbitals ψ_i, ELF is defined as,

$$\chi_{ELF} = [1 + (D/D_h)^2]^{-1}, \tag{2.35}$$

where

$$D_h = (3/10)(3\pi^2)^{5/3} \rho^{5/3}, \tag{2.36}$$

$$D = (1/2) \sum_i \mid \nabla\psi_i \mid^2 - (1/8) \mid \rho \mid^2 / \rho, \tag{2.37}$$

and $\rho \equiv \rho(r)$ is the valence electron density. D and D_h are excess local kinetic energy density due to Pauli repulsion, and Thomas-Fermi kinetic energy density respectively. The numerical values of ELF are normalized to a value between zero and unity. A perfect localization of the valence charge is represented by a value of 1, while for uniform electron gas the value is 0.5. A high value of χ_{ELF}, like 0.70 signifies a localized bond.[142]

2.5.5 Shape analysis

Planar arrangement: The planar nature of a structural geometry is determined with the help of a regression plane. In this method, a regression plane is calculated for the set of atoms associated with a distinct plane in a particular system. Depending on the planarity, deviations may be seen from the set of atoms from the regression plane.[143]

Spherical arrangement: On a similar line, 2D mapping of atoms is used to verify the spherical shell formation among the clusters. 2D mapping is the projection of atomic coordinates onto xy, yz, or zx planes in the spherical (θ,ϕ,R) coordinate system. This projection is obtained by plotting the distance of each atom from the x, y, and z axes (along planes y-z, z-x, x-y, respectively), and plotting it against the x, y, and z co-ordinates, respectively.[143]

2.5.6 Distance-Energy (DE) plots

In this method, a matrix is introduced to measure the dissimilarities between configurations in the high dimensional configuration space.[144] The elements of this matrix depend on the configurational distance computed by taking the difference between KS eigenvalues of local minima and the ground state. The matrix based on KS eigenvalues is a good choice for calculations within the DFT framework, since the eigenvalues are a byproduct of these calculations.[144] The distance-energy plots based on this matrix method characterize the potential energy surface (PES) of clusters.[145] A representative DE plot is shown in Fig. 2.3, where the x and y axes plot the difference in energy (ΔE) and KS eigenvalues (fingerprint distance) of a particular isomer with respect to the GS. Since different arrangements of atoms lead to distinct KS eigenvalues, the corresponding distance matrix could be used as a fingerprint for that particular arrangement of atoms (isomer). Thus, each point in the graph represents the distinct isomer observed for a particular system. The plot would then convey the character of the PES of that particular system. For instance, simulation studies showed that a distinct gap is observed if one plots the DE plot for a non-glassy structure. However, the same shows a continuous distribution in its DE plot for a glassy structure.[144, 145]

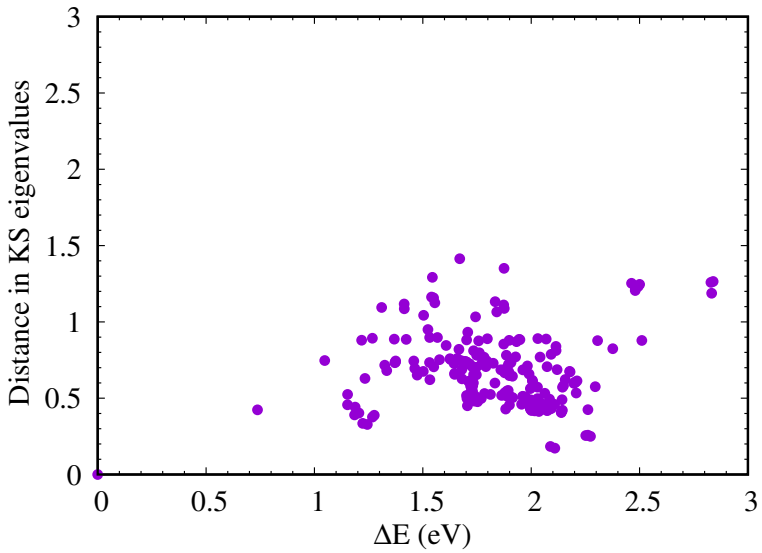

Figure 2.3: *A representative DE plot.*

2.5.7 Nudged Elastic Band (NEB) method

This method is used for finding saddle points and minimum energy paths (MEP) between known initial and final states.[146–148] This technique is employed in conjunction with electronic structure calculations, especially in particular plane wave based DFT calculations and empirical potentials. In NEB, MEP is obtained by constructing a set of images of the system typically of the order of 4–20 between the initial and final states. A constrained optimization of these images is carried out by adding spring forces along the band between images, projecting out the component of the force due to the potential perpendicular to the band. An important feature of the NEB method which distinguishes it from other elastic band methods is this force projection, also referred to as "nudging". This force projection ensures that the spring forces do not interfere with the convergence of elastic band into the MEP, and the true force does not affect the distribution of images along the MEP. Further, this controls the spacing of images along the band. If this projection scheme is not used the spring forces tend to prevent the band from following a curved MEP and the true force along the path causes the images to slide away from the high energy regions towards the minima (local optimization).[146–148]

2.6 Error analysis

Numerical simulations are liable to many kinds of errors. It is necessary to follow different methods to reduce these errors as much as possible. The different approaches and convergence tests that are carried out to reduce numerical and statistical errors are described in this section.

The term error means the difference between true value and estimated or approximated value. Comparisons with experimentally available results are a good way to estimate the percentage of error in the simulations. The pseudopotential, cut-off energy and size of the simulation box are a few parameters that should be checked before starting the final set of calculations.

Statistical data

Thermalisation time

In all these calculations, an initial 30 ps of the simulation data is always discarded to account for the thermalisation. This time is found to be sufficient for attaining the thermalisation for the systems under study. To decide this time, we computed the δ_{rms} by varying the time left for thermalisation, as is shown in Fig. 2.4. The red graph plots the initial 30 ps/temperature without discarding any data for thermalisation. Whereas the other three graphs show the δ_{rms} computed after removing

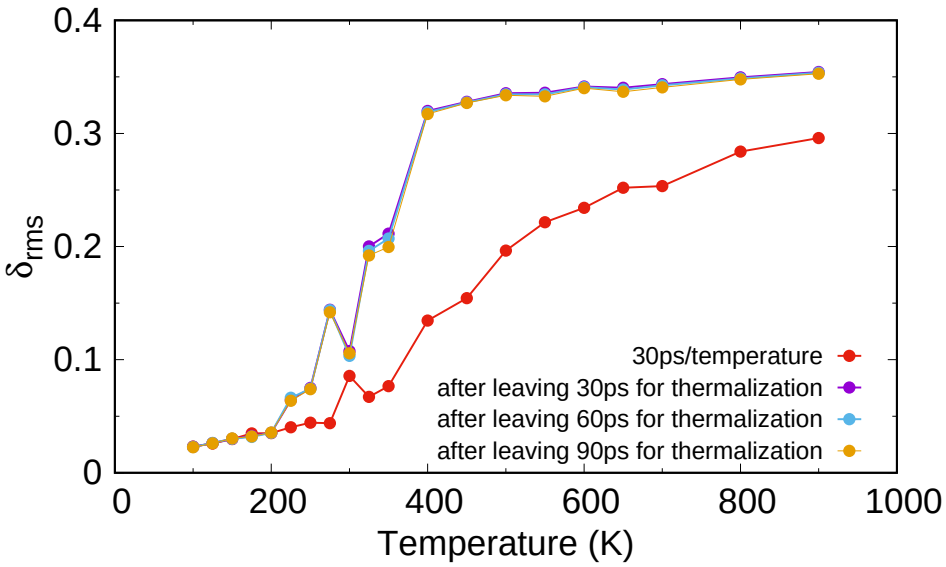

Figure 2.4: *δ_{rms} computed with initial 30 ps is shown by red graph. The same calculated after discarding initial 30 (purple dots), 60 (blue dots) and 90 ps for thermalisation gives identical graphs.*

30 (purple dots), 60 (blue dots) and 90 ps (golden dots) for thermalisation. It is seen that the δ_{rms} calculated with initial 30 ps (not the thermalised one) leads to inaccurate results. The other sets of data give logically sound similar values for δ_{rms}. Since values computed by discarding 60 and 90 ps are identical, one can safely proceed to all other calculations by leaving out the first 30 ps for thermalisation.

Simulation time

Once the time for thermalisation is decided, we next figure out how much simulated data is needed for calculating the parameters in an accurate way, within the limit of computational expense. One can decide this by testing the convergence of any of the computed quantities as a function of simulation time. Fig. 2.5 plots the δ_{rms} at three different total times. The purple graph plots the δ_{rms} computed over the total simulation time after discarding 30 ps for thermalisation. The green and golden graphs plot the δ_{rms} computed over a time period after removing the last 30 and 60 ps along with the initial 30 ps from the total simulation time. The total simulation time is different at each region. For instance, in solid-like and liquid-like states the δ_{rms} is calculated over a time of 120 and 210 ps respectively for the case represented in the figure. Whereas in transition region, the same is computed over a time of about 600 ps. It is clear from the plot that the calculated δ_{rms} does fairly converge with the simulation time.

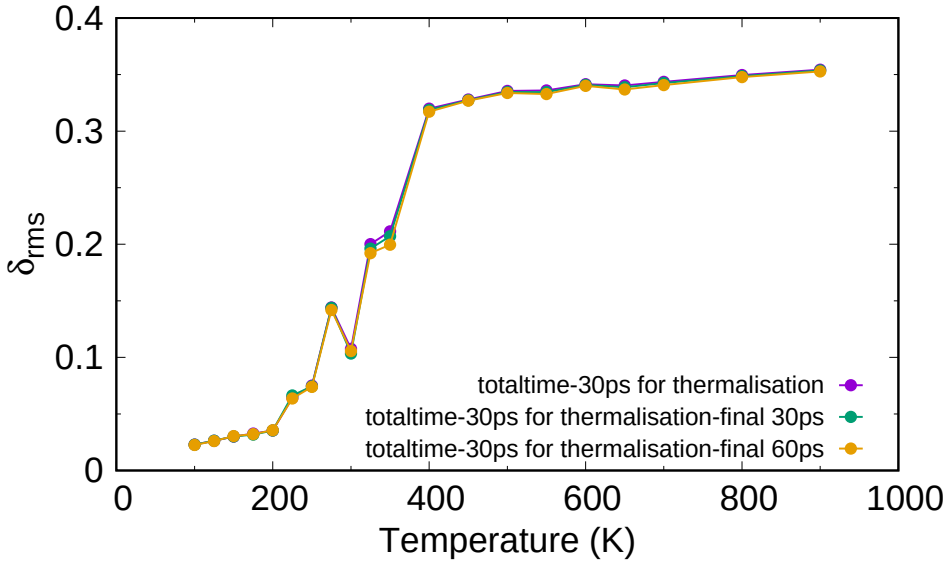

Figure 2.5: *δ_{rms} computed with total simulation time after discarding the initial 30 ps for thermalisation shown as purple dots. The δ_{rms} calculated by removing the last 30 (green dots) and 60 (golden dots) ps along with the initial 30 ps from the total simulation time.*

Thus, these error analysis indicate that the available simulated data is reliable enough to explain finite temperature behaviour of small clusters by computing different parameters.

CHAPTER 3

Role of GS motif in the variation of melting temperature

3.1 Motivation and definition of the problem

Size sensitive variations in measured melting temperatures are a generic feature observed for clusters of Na, Al and Ga.[14, 15, 39] Incase of Na, the variation is of the order of $\approx$ 100 K for clusters in the size range of 55–357.[14] However, the noticed fluctuations are of the order of $\approx$ 400 K, with addition of a few atoms for Ga and Al clusters.[15, 39] First principle based investigations are available to understand these size induced variations. The initial simulation studies performed on Na clusters reasoned out these observations to an extent. For instance, calculations on a few sizes like n = 55, 92, 147, 181, 189, 215, 249, 271, 281, and 299 demonstrated that clusters with high surface stability melt comparatively at a higher T_m.[94] Further, the bondlength analysis illustrated that, shorter the distance between bulk and surface atoms, higher the melting temperature.[94] Growth pattern investigations carried out on sodium clusters (Na_n) in the size range n = 55–62 showed an icosahedron based GS structures in the size range 55–57.[99] Whereas the GS motif becomes roughly spherical at a size of n = 58, and thereafter possesses disordered structures for n = 59–62.[99] Moreover, a comparative study of the bond length distribution on Na_n, n = 55, 57 and 58 illustrated that 58 atom cluster possesses relatively more shorter bonds, thus giving rise to higher T_m. In addition to this it is showed that, clusters with disordered structure display a broader peak in their heat capacity curve.[99] The growth pattern studies on Na_n (n = 39–55) clusters demonstrated that the geometries are nearly spherical for n = 39–43, and exhibit partial icosahedral structures. Whereas that of n = 44–52 are disordered ones and may be considered as a transition region from a two-shell icosahedron Na_{40} to a three-shell complete icosahedron Na_{55}. Further a three-shell icosahedral structure is identified for clusters of the size $n \geq 53$.[98] Thus the growth

pattern exhibits a transition cycle from an ordered one to another ordered one through a disordered structure.[98] A corresponding transition in the nature of heat capacity curve from a peaked to very broad to a peaked one was also noticed in this size range (n = 39–55).[98] Thus the sharp vs broad transition noticed for many of the Na clusters is described using the ordered vs disordered nature of GS structures. Besides, the higher T_m observed for a few Na clusters is explained based on the distribution of short bonds in those clusters.[98]

Similarly for Al clusters, the variations observed in the size range n = 31–48 were explained based on higher connectivity between the core and surface atoms. Also, the broader transition in their heat capacity curve was interpreted based on the presence of a less connected and opened GS structure.[113] Furthermore, in another study the changes noticed in the melting temperatures for larger clusters, with size around 55 atoms, were related with that of symmetry reduction in their GS structures.[114] Growth pattern observed in the aluminium clusters in the size range n = 30–70 showed that, these systems pass through different structural motifs.[37] This study pointed out that a drop in the measured T_m is correlated with the corresponding change in their GS motif.[37] On similar lines, a few studies on Ga clusters interpreted the sharp vs broad transition based on the "orderness" of the GS structure.[119] An examination of connectivity on a few Ga clusters (n = 31–48) indicated that, stronger the bonds higher the T_m.[120]

Thus in brief, the initial simulations carried out on Na, Al and Ga clusters were explained the observed size-dependent variations on the process of melting to an extent. Even if these investigations brought out the structural changes in the clusters, the influence of changes in properties associated with these structural transitions, on melting, has not been explored completely. Though the analysis of bondlength distribution and connectivity between different shells were able to relate the higher T_m observed for a few clusters, a thorough systematic study with size of the cluster is not available. Moreover, the size-sensitive fluctuations detected in small Ga clusters in the size range n = 31–48 have not been fully explored till date. The observed fluctuations in the measured T_m of Ga clusters in this size range are shown in Fig. 3.1. The whole range is divided into two regions, termed as high-melters and low-melters, and are shown in red and blue ellipse respectively in the Fig. 3.1. Clusters with size n = 46–48 melt at a T_m of about 800 K and are classified as high-melters, whereas those with atoms 31–42 are low-melters and posses a T_m in the range 500–600 K. Thus it is evident that adding a few atoms changes the T_m by a value of few hundred Kelvin. It is important to understand the factors which lead to this shift in temperature for gallium clusters in this size regime. Growth pattern of positively charged gallium clusters with sizes between 31–48 atoms is investigated to address this problem. Thus the present study provides a possibility to explore the evolution of clusters in this size range as well as its impact on the fluctuations in their measured T_m. The details of computational methods are provided in the section 3.2. The ground state (GS) geometries and their different properties are

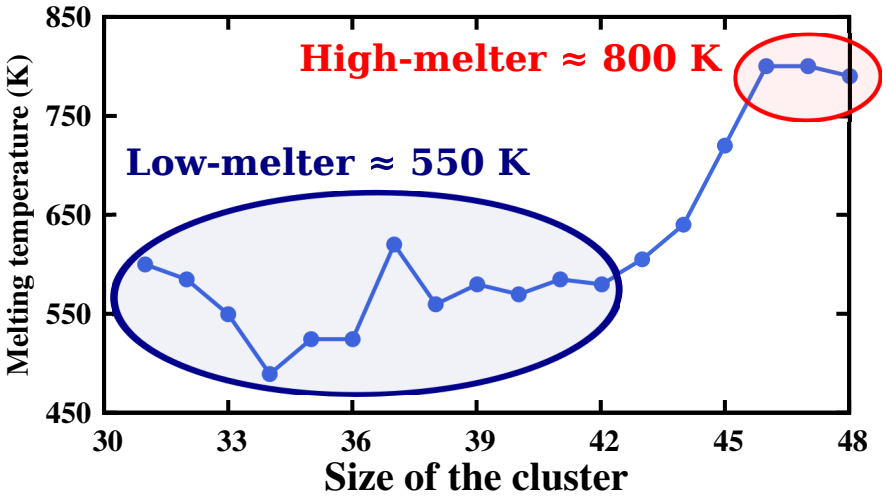

Figure 3.1: *The measured T_m of Ga clusters in the size range n = 31–48 is plotted as a function of size of the cluster.[38] The high and low melters are grouped based on the melting temperature are highlighted in red and blue ellipse respectively along with the approximate T_m.*

discussed in the section 3.3. The summary and the conclusions of the current study are presented in the section 3.4.

3.2 Computational details

The structures were optimized using Born-Oppenheimer molecular dynamics based on the Kohn-Sham formulation of density functional theory. The interactions between the ion and valence electrons were described using projector augmented wave potentials, with the generalized gradient approximation, and the Perdew-Burke-Ernzerhof (PBE) exchange-correlation functional as implemented in Vienna *Ab-initio* Simulation package. The size of simulation box was 25 Å which was found to provide sufficient convergence in the total electronic energy. The search for the global minima was a multi-step process. In the initial step, the previously published geometries of neutral Ga and Al clusters were optimized after appropriately scaling the bondlengths to that of Ga.[113, 120, 149] Additionally, local optimizations were performed using the geometries available for different clusters obtained by employing empirical potentials.[150] The lowest energy structure within all these quenches was taken as a starting point for the next level of search for the GS. Since the melting temperatures were already known from the experiments, all clusters were maintained at three different temperatures near their respective T_m for a few hundred pico seconds (300 ps or more). Structures for local optimizations were then selected from these high temperature MD runs. Several geometries were also constructed by adding (removing) atoms to smaller (larger) clusters. Through all these procedures at least 150 geometry optimizations per system were performed which resulted into about 3000 geometry

optimizations for the whole series. The structure with the lowest energy was treated as the global minima found within this search.

3.3 Results and discussion

The result part begins with the discussion of ground state structures found for these clusters within this simulation study (See section 3.3.1). The details about extensive isomer analysis are described in the section 3.3.2. Effect of the GS motif on the finite temperature behaviour is outlined in the section 3.3.3. The main conclusions are described in the section 3.4.

3.3.1 The Ground state structures

The low-energy structures of gallium clusters in the size range 31–48, are represented in Figs. 3.2–3.4. The structures are classified into three different families. For clusters with size 31–39, the ground states are dominated by the formation of planes, and are shown in Fig. 3.2. Clusters in the range 40–42 are the transition region and their GSs are characterised by the presence of both planar and spherical like arrangement of atoms as shown in Fig. 3.3. The systems with size 43–48 are dominated by spherical polyhedra with distinct core and shell and are shown in Fig. 3.4. A rotated view where the parallel planes are evident for three representative systems is labeled as "**a**" and is shown in the last column of Fig. 3.2. The rotated view for Ga_{31}^{+} indicates that the GS is a three layered structure with A–B–A packing (see **31a** in Fig. 3.2). The three layered base structure is same up to the size of 34 atoms cluster. However, depending upon the position of ad atom (shown by white sphere in Fig. 3.2), the stacking pattern varies from A–B–A to A–B–C. At a size of 35, the base structure changes from a three layered structural motif to one consist of four planes, termed as distorted decahedral fragment (DDF), which is accompanied by a corresponding change in T_m. Till n = 38, the atoms add to this base structural motif, DDF. The motif again changes to a three layered pattern at a size of 39, and the ad atoms to the base structure are shown in white color. A structural transition region is seen in size range n = 40–42, as presented in Fig. 3.3. These structures indicate a transition of the GS towards spherical shape. As seen from the figure, part of the cluster is still dominated by the formation of planes and other part tends to be more spherical. The GS motifs with spherical geometry, for clusters with size n = 43–48, are shown in Fig. 3.4. All these clusters possess a distinct core in their GS structure and the core atoms are shown with red color in Fig. 3.4. Building up of core in the GS motif plays a crucial role in stabilizing these clusters at higher temperatures, which is discussed in the following sections. In brief, the GS motif upto a size of 39 is dominated by planes, and around 43 the GSs become spherical with distinct core formation.

The observed structural transition is brought out in a quantitative way by shape analysis and is

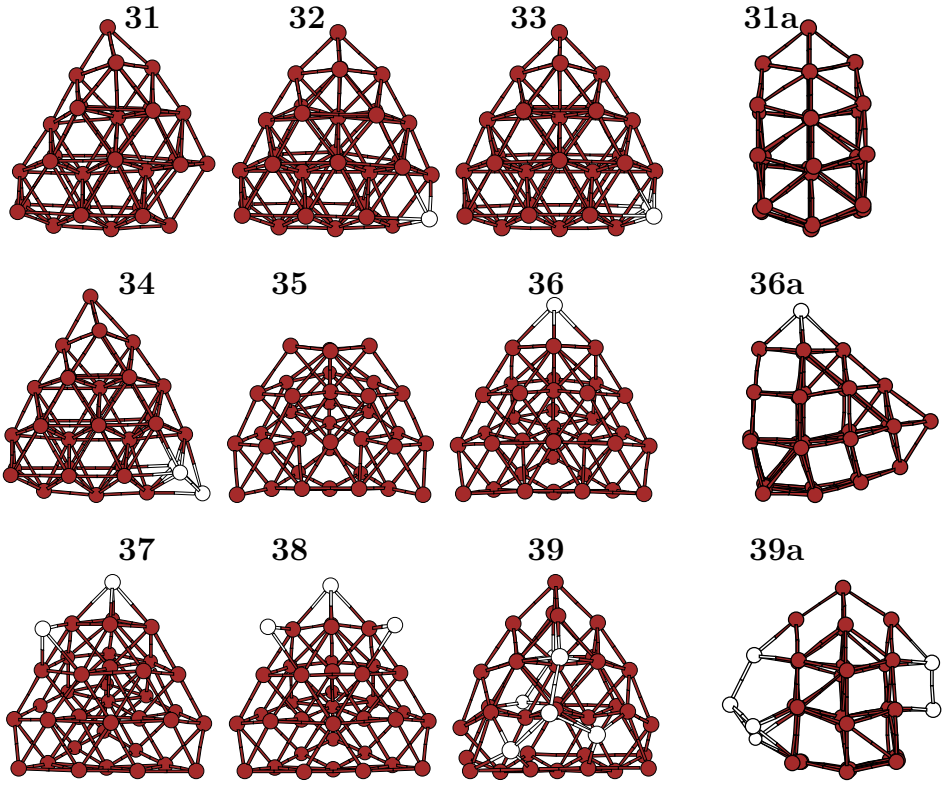

Figure 3.2: *The low-energy structures of Ga_{31}^{+} to Ga_{39}^{+} are shown. A different view obtained by rotating the cluster is presented in the last column, labeled as* ***a****. All the geometries are dominated by formation of planes. Ga_{31}^{+} is considered as the base structure till 34. Ga_{35}^{+}, with DDF structure, is considered as the reference structure till 38. The added atoms to the base structure is shown as white spheres. Ga_{39}^{+} has same structural motif as that of Ga_{31}^{+} and the atoms in white indicate additions over Ga_{33}^{+}.*

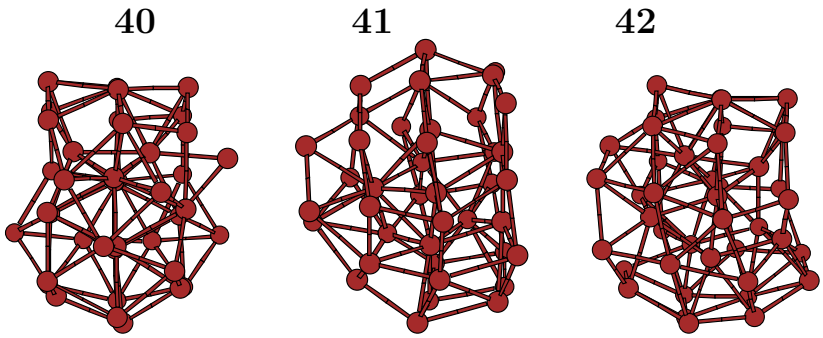

Figure 3.3: *The most stable isomers of Ga_{40}^{+} to Ga_{42}^{+} are shown. The transition from planar structures towards spherical structure is evident.*

represented in Fig. 3.5. The distribution of atoms in planes are demonstrated by fitting a regression plane for the set of atoms associated with distinct planes. The distance between the atoms and the respective regression plane fitted to these atoms, is shown in Fig. 3.5(a). For Ga_{31}^{+} to Ga_{34}^{+} there are three sets of atoms, each set represents a plane. In case of 35 to 38 four regression planes could be fitted. The deviation of atoms from regression plane is ranged between 0.002 – 0.12 Å up to size

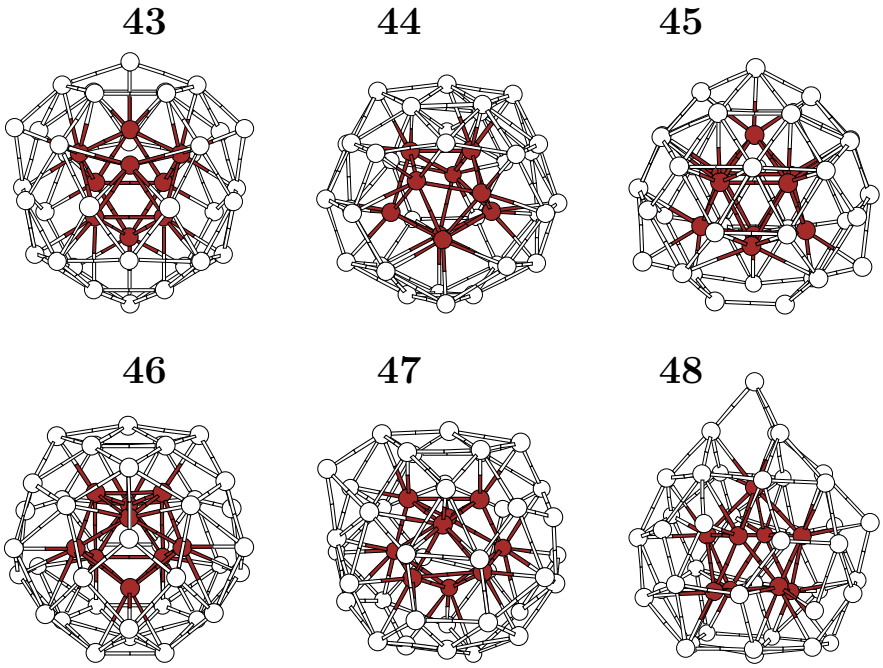

Figure 3.4: *The most stable isomers of Ga_{43}^{+} to Ga_{48}^{+} are shown. All these structures are spherical with distinct core and surface shells. For clarity, the core atoms are shown in red.*

34 and is less than 10% of plane separation ($\approx$ 3 Å) for larger clusters till size 39. In order to verify the spherical shell formation among some of the clusters, we calculated the distance of each atom from the x, y, and z axes (along planes y-z, z-x, x-y, respectively), and plotted it against the x, y, and z co-ordinates, respectively, as shown in Fig. 3.5(b). For a better representation of the data, the distances were given the sign of y, z, and x co-ordinates, respectively. For a spherical cluster (e.g., Ga_{46}^{+}), for each axis the atoms near the poles are closest to the given axis while towards the centre they move away from the axis progressively. Thus, for a cluster forming spherical shell, the above gives a circular distribution of distances along each axis. Fig. 3.5(b) shows two concentric circles for Ga_{46}^{+}, confirming the existence of distinct and well-separated core and surface shells. On the contrary, other clusters show scattered distribution which indicates absence of such shells. Thus, both the qualitative and quantitative analysis demonstrated that the GS can be broadly classified into two different structural motifs. Clusters with sizes up to 39 have "planes" (Class-I) as a part of GS, whereas clusters with high T_m have spherical structures with distinct core and surface shells (Class-II).

The effect of change in the structural motif on the connectivity among atoms is demonstrated in the following texts. The number of bonds between internal atoms (or core atoms) along with the measured T_m, as a function of cluster size are shown in Fig. 3.6. It is seen from the graph that, a change in the structural motif is associated with a substantial increase in the number of bonds between core atoms. For clusters with "planar" geometry, the number of bonds within internal

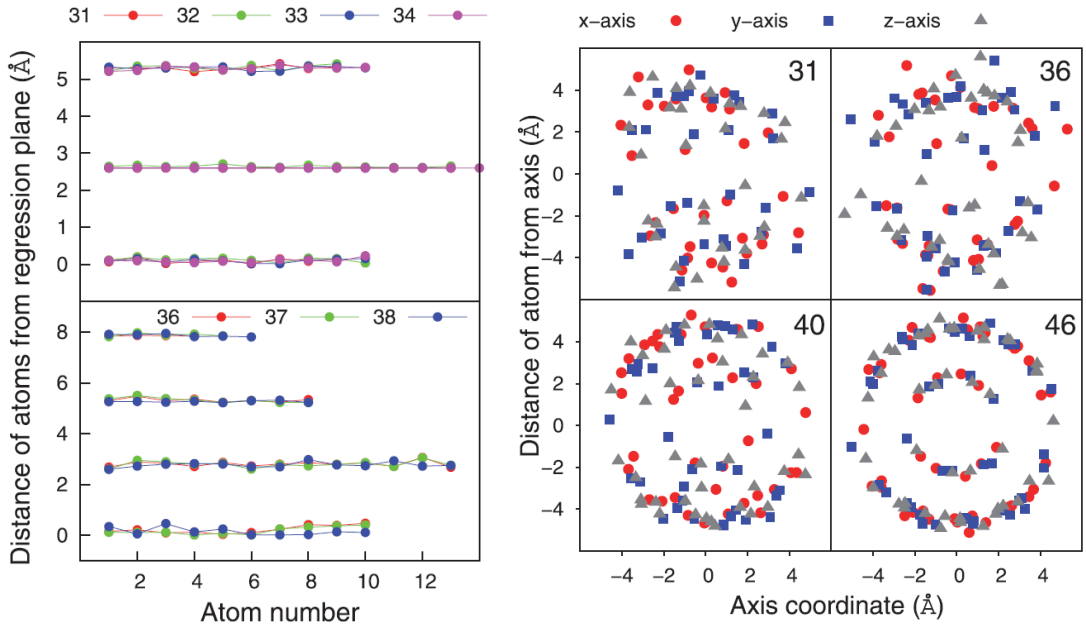

Figure 3.5: *(a) Perpendicular distance of each atom from the fitted regression plane, showing almost planar arrangement of atoms, for sizes indicated. Separation between planes is taken as 2.6 for plotting. (b) Plot of distance of each atom, for sizes 31, 36, 40, and 46, along y-z/z-x/x-y plane, against the x/y/z axis coordinate respectively. The graph signifies that core-shell type formation is symmetrically seen along all the three axes, for size 46, while others show a spread.*

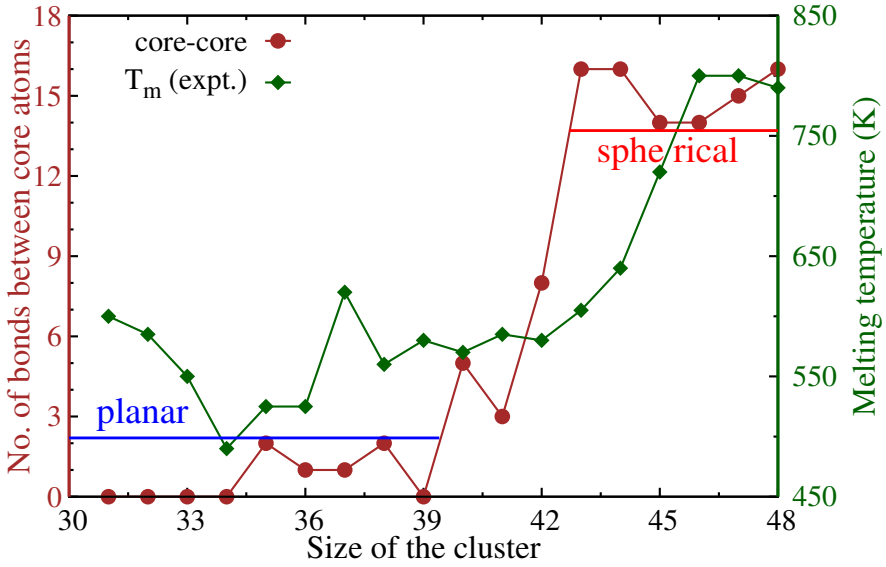

Figure 3.6: *The number of bonds between core atoms (brown) as a function of cluster size. Significant increase in the number of bonds has been observed for spherical clusters having elevated melting temperatures. Experimentally measured T_m (green) from Ref. [38] also shown in the plot.*

atoms are less than one per atom (blue line in Fig. 3.6). Whereas for clusters with "spherical" geometry there are about 2 bonds per core atom (red line in Fig. 3.6). Thus, the spherical clusters possess a strongly connected core and surface. The influence of higher connectivity on the process of melting is explained in the next section.

3.3.2 The isomer distribution

Isomerisation is the initial stage of melting in which the atoms start to diffuse through a cluster. Hence, investigation of isomer distribution of these clusters will provide an indication about the melting of these systems. Extensive isomer analysis is carried out, and the obtained distinct isomers are classified into different isomer families. The different families of isomers and their relative energies with respect to the GS are represented in Fig. 3.7. The isomer families include, three layered structures with A–B–A or A–B–C packing, distorted decahedral fragments (DDF), DDF with surface, or edge atoms missing from the base structure and located as caps (DDFs or DDFe), spherical structures with and without distinct core (Sph), and finally disordered isomers (Dist). The point corresponds to each family, represents the energy at which a distinct isomer of that particular family appears for the first time. All the isomer families span an energy range starting from the point shown in the figure. For example in case of Ga_{45}^{+} the isomer family **Sph** shown only as a

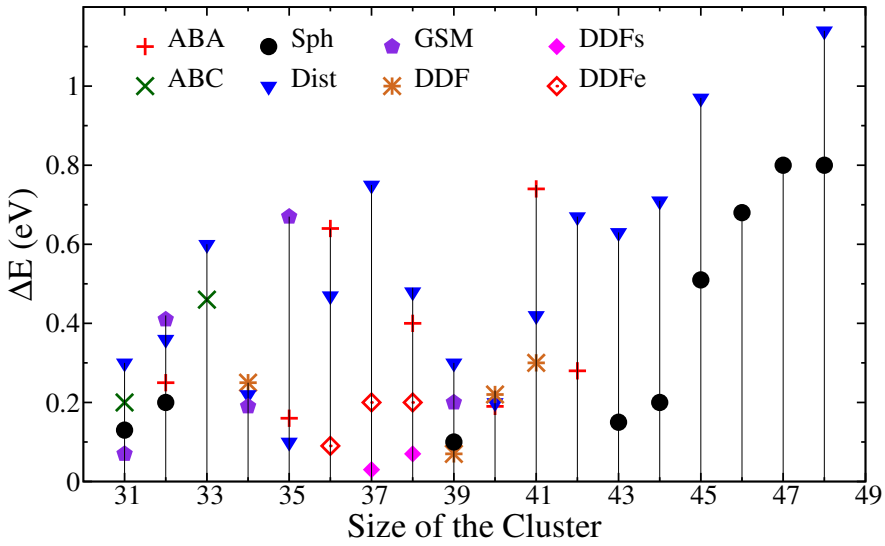

Figure 3.7: *The energy difference with respect to the GS for different families of isomers as a function of cluster size.* ***ABA*** *and* ***ABC****: three layered structures with different packing types,* ***DDF****: distorted decahedral fragment,* ***Sph****: spherical structures without core and surface distinction,* ***GSM****: geometries with minor changes to the GS but with same structural motif,* ***DDFs****: DDF structural motif with one of the surface atoms displaced,* ***DDFe****: DDF structural motif with one of the edge atoms displaced. Note that for clusters with high T_m, the energy difference between the GS and the first isomer family is about 0.5 eV or higher, whereas for clusters having low T_m, occurrence of various isomer families is observed at much lower energy difference.*

black circle at 0.51 eV has its isomers extending in energy from 0.51 eV up to 1.17 eV. Similarly, other groups have their energies extending upwards from the point shown in the figure. For all clusters smaller than 40 the first isomer family appears at 0.2 eV or less above the base energy, whereas for clusters larger than 44 the first isomer family begins at 0.5 eV or above. Thus, the appearance of first isomer family at as high as 0.5 eV indicates a delayed isomerisation. Thus, the presence of strongly connected core in case of clusters with distinct core and surface shell delays the isomerisation process and leads to higher melting temperature. The effect of a core-shell structure on the finite temperature behaviour is further elucidated by analysing distribution of atoms about their centre of mass (DCOM) as shown in the next section.

3.3.3 The finite temperature behaviour

The effect of structural motif on the finite temperature behavior is demonstrated by choosing two clusters from each class. The distribution of atoms from the COM for two representative sizes Ga_{36}^{+} and Ga_{46}^{+} is shown in Fig. 3.8. For Ga_{36}^{+} the atoms are distributed among three shells like

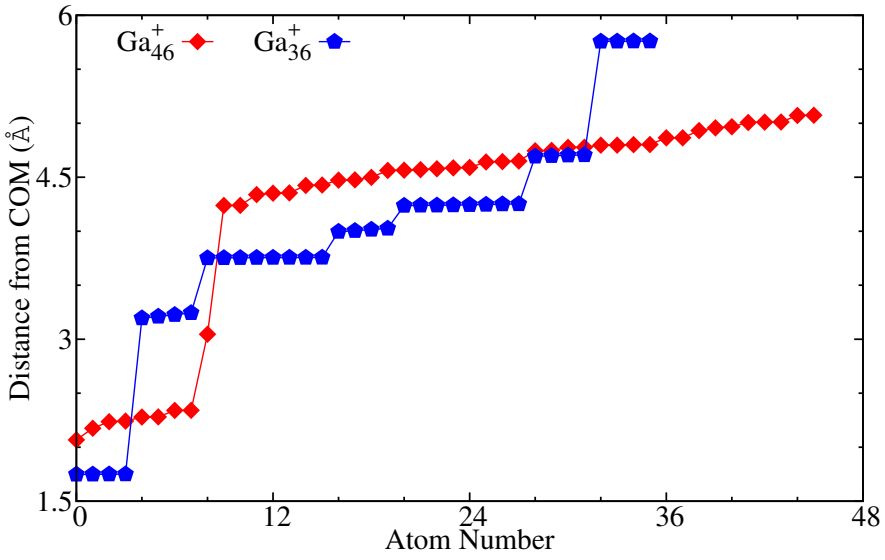

Figure 3.8: *Distribution of atoms from the center of mass of the cluster. For Ga_{46}^{+} (red graph), there are two distinct shells. Though the atoms in Ga_{36}^{+} (blue graph) are distributed mainly into three shells.*

core, shell and edge (blue graph in Fig. 3.8). Core and edge consist of 4 atoms each, and the rest (28 atoms) form the surface. The surface atoms are distributed in five subshells and are spread over 2.5 Å. Contrary to this, in Ga_{46}^{+} the atoms are distributed into two distinct shells, such as core and surface shell centered about the COM (red graph in Fig. 3.8). These two clusters are simulated at three different temperatures to illustrate the effect of distinct core-shell structure on the melting process. The measured T_m of Ga_{36}^{+} and Ga_{46}^{+} is 550 K and 800 K respectively. Both clusters are kept at 150 K, 350 K, and 650 K for a time period of 180 ps. Ga_{46}^{+} is also maintained at 900 K, i.e.

slightly above its T_m for 180 ps. Fig. 3.9, shows the distribution of atoms for Ga_{36}^+ and Ga_{46}^+ about the COM of the cluster computed over the last 150 ps, at different temperatures. For a 36 atom cluster, at 150 K, there are three distinct shells. The first peak represents 4 internal atoms, while the last peak represents 4 edge atoms. The in-between peaks are due to the remaining 28 surface atoms, which have already merged into each other indicating the initiation of inter-shell diffusion. The separate peaks for internal and edge atoms indicate that the atoms belonging to these shells are still confined. With rise in temperature, at 350 K all the sub-shells of the surface fully merged and

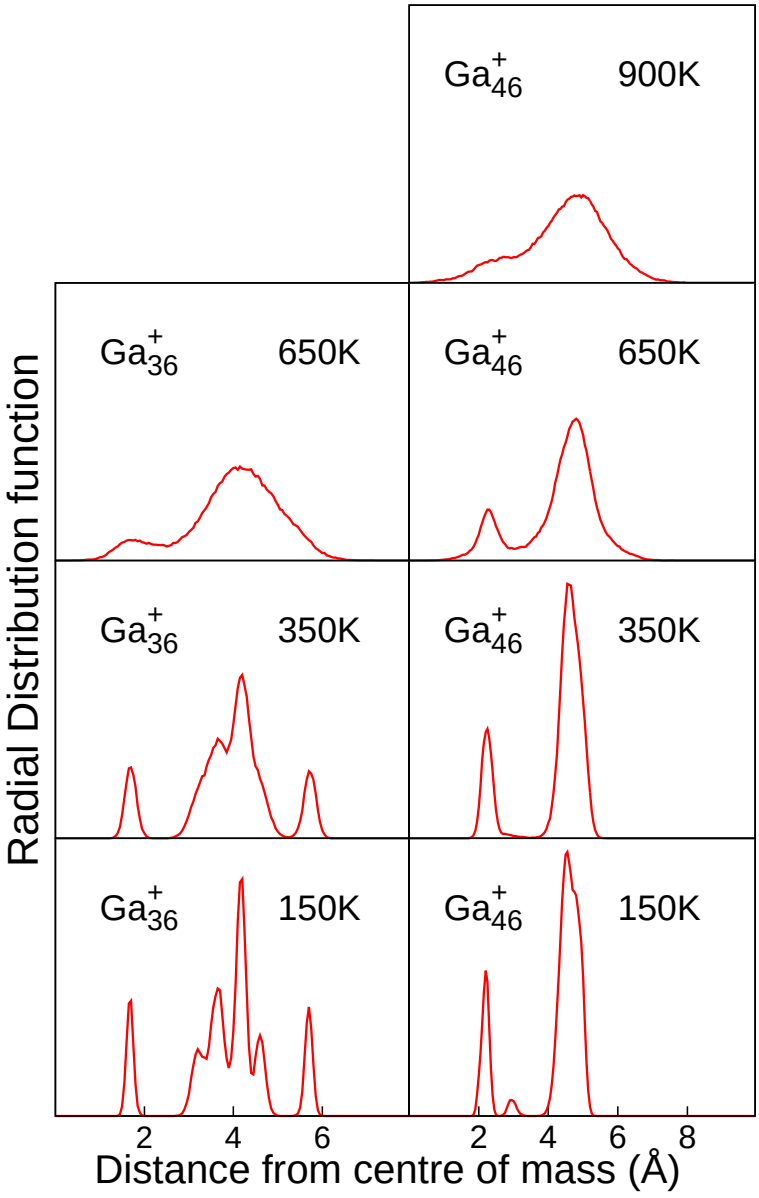

Figure 3.9: *Distribution of atoms about the center of mass of the cluster for Ga_{36}^+ and Ga_{46}^+ at various temperatures. The clusters are maintained at these temperatures for 180 ps. Interestingly, for Ga_{36}^+ at 650 K, the absence of well-separated shells indicates that the cluster is already in liquid-like state whereas, Ga_{46}^+ exhibits the same behavior at 900 K.*

are on the verge of merging with that of the edge atoms. Though, the first shell is still unaltered apart from the expected thermal broadening. However, at 650 K all the shells have lost their identity and the cluster is in liquid-like state. Comparing this behavior with that of 46 atom cluster, at 150 K there are only two shells those represent the core and surface. With increasing temperature, thermal broadening is observed due to the inter-shell diffusion, though the atoms are not diffusing from one shell to another. This cluster retains the existence of two separate shells, even at a higher temperature of 650 K, inspite of the intra shell diffusion. It is evident from the radial distribution function that at a temperature around 900 K the shells have lost their separate identity, i.e. cluster is in liquid-like state.

3.4 Summary and conclusions

Ab-initio density functional simulations have been employed to search for the putative global minima of positively charged gallium clusters Ga_n^+, with n = 31–48. The investigations brought out the factors responsible for the observed fluctuations in the melting temperatures of Ga clusters. The study demonstrated the correlation between the structural motif and the variations in the T_m. The investigations also elucidated the effect of changes of the GS properties on the variations in their melting temperatures. Bondlength analysis indicated that clusters having spherical core and shell structural motif possess higher connectivity among internal (core) atoms. Thus, these clusters have a well-separated core and surface shells which resulted into a delayed isomerisation. That means, the (well connected) atoms in both the shells are resistant to the diffusion across the shells at lower temperatures and maintain the identity of the shells intact. This leads to a higher stability of these clusters at an elevated temperatures and gives rise to higher melting temperatures. Though, for clusters with a planar geometry the connectivity among atoms is less which leads to an early isomerisation and lower melting temperatures. Thus, these investigations revealed that a change in the structural motif of the GS correlates well with the experimentally observed shift in their T_m.

CHAPTER 4

Role of the GS motif in the nature of phase transition

4.1 Motivation and definition of the problem

The observed fluctuations in the measured T_m of small gallium clusters (n = 31–48) have a correlation with the ground state structural motif, as explained in the previous studies. These simulations demonstrated that a structural change in clusters is responsible for the observed variations in T_m. Though, the effect of different structural motifs in the process of melting is not explored through the previous studies. The influence of GS motif in the nature of phase transition is investigated thoroughly and is discussed in the present study. The extensive analysis is performed on three size selected clusters which represent the diverse behaviour of melting in gallium clusters. The systems considered for analysis are Ga_{46}, Ga_{60} and Ga_{94}. Among these, Ga_{46} and Ga_{94} represent sharp melters, while Ga_{60} represents a broad melter. In addition to this, Ga_{46} and Ga_{94} represent the high vs low melter while Ga_{94} being the smallest cluster, melts at a temperature lower than that of bulk.[38, 39] Further, an overall decrease in T_m as a function of size is explored through these simulations. The computational details of the present simulations, and their results and discussion are presented in the following texts.

4.2 Computational details

An elaborate search was carried out in this work to locate the GS of Ga_{94}. GS geometries of Ga_{46} and Ga_{60} were used from our previously published work.[143, 151] Locating the GS structure of Ga_{94} involved extensive searches consisting of multiple BOMD runs initiated with different structural motifs to sample the potential energy surface, which are coupled with manual tampering

of geometries. Since the number of possible isomers of a cluster increases exponentially with increasing size of the cluster, an exhaustive search of all possible isomers, especially with *ab-initio* methods is not possible. Hence, in spite of the rigorous efforts invested in locating new GS structures, there remains an inherent finite possibility that the GS located in this work can be made better in a later stage. However, the finite temperature runs carried out using these GS structures were able to reproduce the experimental observations quite reliably. General scheme followed for thermodynamic runs was as follows. The GS structure was slow heated in a single MD run. This was then used to spawn two different MD runs. The first one was a constant temperature MD at the terminal temperature of previous slow heating. The second run was used to continue heating to the next temperature. This template of spawning two MD runs from each slow heating run was repeated up to and beyond the experimental melting temperature of the particular cluster. Interval of slow heating and temperature for constant temperature MD differ for each cluster and was decided in accordance with its melting temperature along with potential energy distribution at a specific temperature. Multiple constant temperature runs varied in length from a minimum of 150 ps to 600 ps, which resulted in a total simulation time varying from 4.3 ns to 7.4 ns. Various qualitative as well as quantitative indicators are computed to analyze the finite temperature behavior of these clusters. For example, distribution of atoms with respect to the center of mass of the cluster at different temperatures and δ_{rms} are analyzed to understand the process of melting. The heat capacity curves were calculated using multiple histogram technique. To scan the potential energy surface and various isomers that cluster visits during finite temperature MD, extensive local optimizations were carried out using the geometries sampled from finite temperature molecular dynamics data. Sampling of geometries was carried out in an unbiased way by choosing geometries from each MD run at equal intervals (3 ps) of time resulting in about 1000 total optimizations with at least 350 distinct isomers for each size. Geometry optimizations as well as BOMD were carried out as implemented in VASP. Nosé thermostat was used to maintain the systems at constant temperatures. Projector Augmented Wave pseudo potential was used to describe the interaction between the core and valence electrons, with Generalized Gradient Approximation and Perdew-Burke-Ernzerhof exchange-correlation functional. Size of the simulation box was chosen such that the distance between adjacent images was at least 12 Å, so as to avoid interaction between images across simulation cells. The criterion for convergence of energy for each self-consistency iteration was 10^{-4} eV. During local optimization the convergence criteria for force on each ion was kept as 0.005 eV/Å.

4.3 Results and discussion

Comparison of the different GS structural motifs of these systems, and their effect on the finite temperature behavior is discussed in detail in the following sections.

4.3.1 The Ground state structures

The GS structures of Ga_n (n = 46, 60, and 94) are shown in Fig. 4.1. The core atoms are shown as white spheres, atoms belonging to shell as red, and the innermost atoms of Ga_{94} as magenta colored spheres, to aid the eye. As labelled in the figure, the structural motifs are classified into three different families. Those are Spherical-Core-Shell (sCS), Elongated-Core-Shell (eCS), and Distorted-Core-Shell (dCS), for n = 46, 60, and 94 respectively. The core structure of these clusters

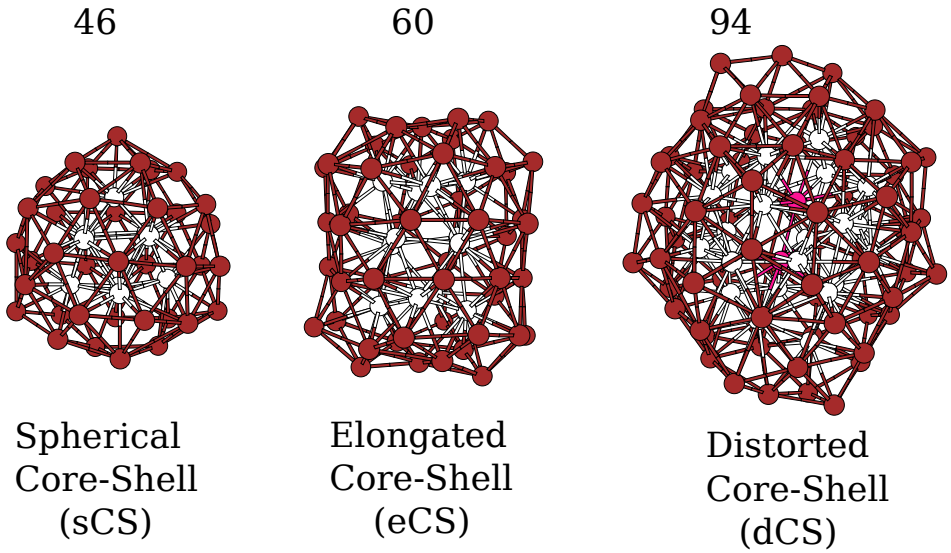

Figure 4.1: *GS structures of Ga_{46}, Ga_{60}, and Ga_{94} labelled along their corresponding structural motifs. Ga_{46} is a Spherical-Core-Shell (sCS) structure, while GS of Ga_{60} is an Elongated-Core-Shell (eCS). Whereas Ga_{94} is a Distorted-Core-Shell (dCS) structure. The core, and shell atoms are represented as white, and red spheres respectively. The two innermost atoms of Ga_{94} are shown as magenta colored sphere.*

is represented in Fig. 4.2. Core of Ga_{46} is a 9-atom trigonal tricapped prism (TTP) which has a C_{3v} symmetry. Core of Ga_{60} is a 12 atom elongated core and is considered as an amalgamation of two TTP units joined along one of its faces. On contrary, the core of Ga_{94} is not hollow, but contains two innermost atoms.

The distinction in these structural motifs is clarified by plotting 2D mapping of the respective structures and is represented in Fig. 4.3. Core and shell of Ga_{46} clearly show as a set of two concentric circles in the 2D mapping, while the elongated shape of Ga_{60} is highlighted by the overall arrangement of 2D data points. Ga_{94} has a core-shell type structure, but its structure is not

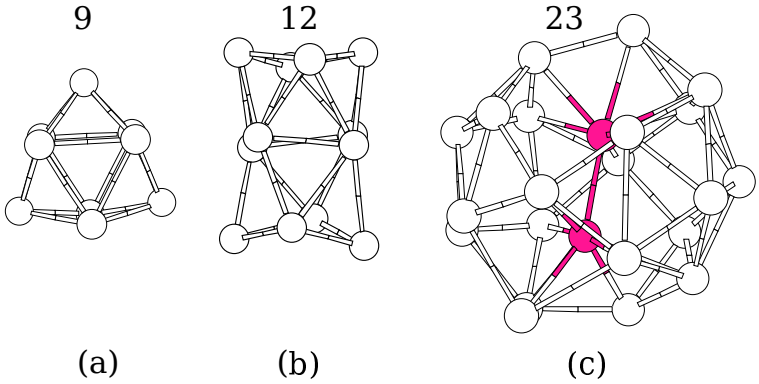

Figure 4.2: *The core structures of (a) Ga_{46}, (b) Ga_{60}, and (c) Ga_{94}, and the number of atoms present in the core is mentioned above the core motif. Except Ga_{94}, all other clusters possess a hollow core structure.*

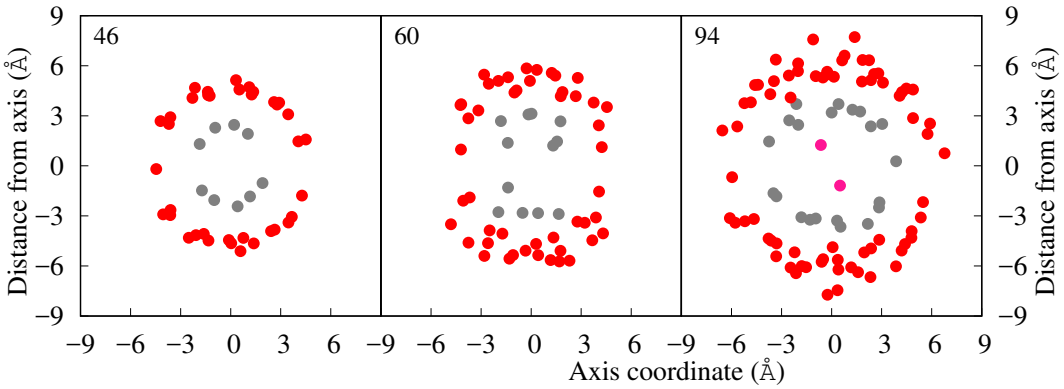

Figure 4.3: *2D-projections of respective GS structures that highlight their structural motifs. Two concentric circles imply that GS of Ga_{46} has two concentric spherical shells of atoms. Elongated GS of Ga_{60} is projected as two elongated sets of points, inner core, and outer shell. The distorted-core-shell motif of Ga_{94} also depicted using 2D projection.*

well ordered, and contains two atoms in its inner shell. Disordered arrangement of atoms with roughly spherical shells is clearly visible in its 2D mapping, hence, Ga_{94} belongs to the 'distorted' core-shell (dCS) motif.

4.3.2 The finite temperature behaviour

Sharp vs Broad transition

The finite temperature behaviour of Ga_{46} and Ga_{60} is compared using various quantities and is presented in Fig. 4.4. The upper panel indicates C_v and δ_{rms} for Ga_{46} (left) and Ga_{60} (right), whereas the lower panel indicates their isomer distribution at different temperatures. Isomers belonging to different families are shown with different colors. Calculated heat capacity curves (C_v, black graphs in upper panels) show that the performed simulations reproduced the

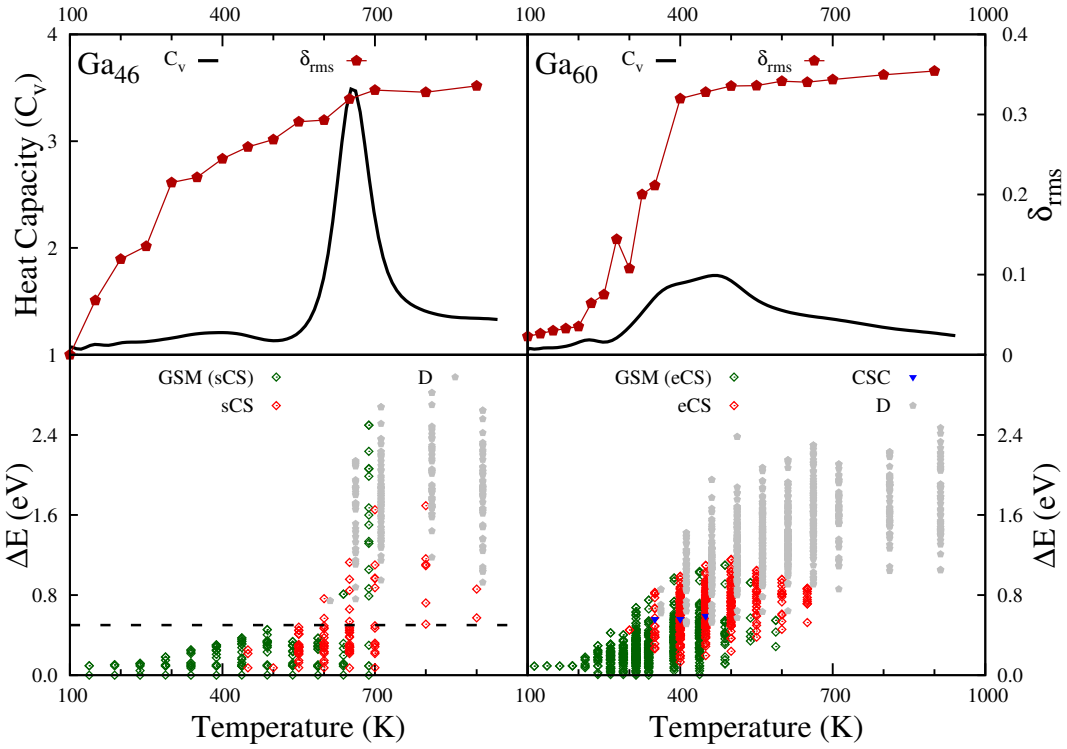

Figure 4.4: *Upper panel: Calculated heat capacity curve (black) along with the δ_{rms} (brown points) for Ga_{46} (left) and Ga_{60} (right). Lower panel: Energies (with respect to the GS energy, ΔE) of different isomer families as a function of temperature at which they occur, for Ga_{46} (left) and Ga_{60} (right). Energies of isomers that occur before melting are limited to below 0.5 eV for Ga_{46}, and rise suddenly at melting temperature, contrary to the gradual and early rise observed in case of Ga_{60}.*

experimentally observed variations in the nature of heat capacity curves, and measured melting temperatures reliably.[38, 39] It is noticed that the melting features of Ga_{60} (upper right panel) are quite contrasting to those of Ga_{46} (upper left panel). While C_v of Ga_{46} has a narrow melting peak at high temperature (700 K), peak in C_v of Ga_{60} is broad (spread over 200 K width), with a lower melting temperature (500 K). Thus, the calculations capture the broadness of experimentally measured C_v of Ga_{60} very well.[38, 39] Furthermore, the calculated melting temperature of Ga_{60} (482 K) is in close agreement with its experimentally measured melting temperature (505 K).[38, 39] The isomer distributions of these two clusters as a function of temperature are shown in the lower panels of Fig. 4.4. These isomers are obtained after optimizing initial geometries selected (unbiased and evenly spaced) from the finite temperature MD data for each temperature. For Ga_{46}, two isomer families exist before the cluster melts. The first one is named as ground state modifications (GSM) where the structural motif along with the number of atoms within each shell remain the same as that of GS (9 core atoms + 37 surface atoms), but the relative orientation of the two spherical shells changes along with the intra-shell diffusion. Till 400 K, this is the only isomer family observed. After 400 K inter-shell diffusion begins, in which the number of atoms within

each shell vary, while keeping the structural motif same (sCS). For Ga_{46}, distorted type isomers (D) appear at and above its melting temperature indicating the destruction of its sCS structural motif. Alike Ga_{46}, there are three dominant isomer families for Ga_{60} as well. First among them is the GSM family, where the number of atoms in each shell remains unchanged, but their relative orientations changes. Another isomer family with similar structural motif but different number of atoms in each shell, elongated core-shell (eCS), dominates after 350 K along with the distorted type isomers. Further, the distorted isomers form a substantial fraction of isomers accessible at these temperatures, contrary to Ga_{46}, where they dominate only after the melting of cluster. Appearance of these two isomer families at much lower temperatures marks the beginning of melting at low temperatures. However, structural identity of the cluster is preserved till 600 K, shown by existence of eCS type isomers till 600 K. Thus, early appearance of distorted isomers

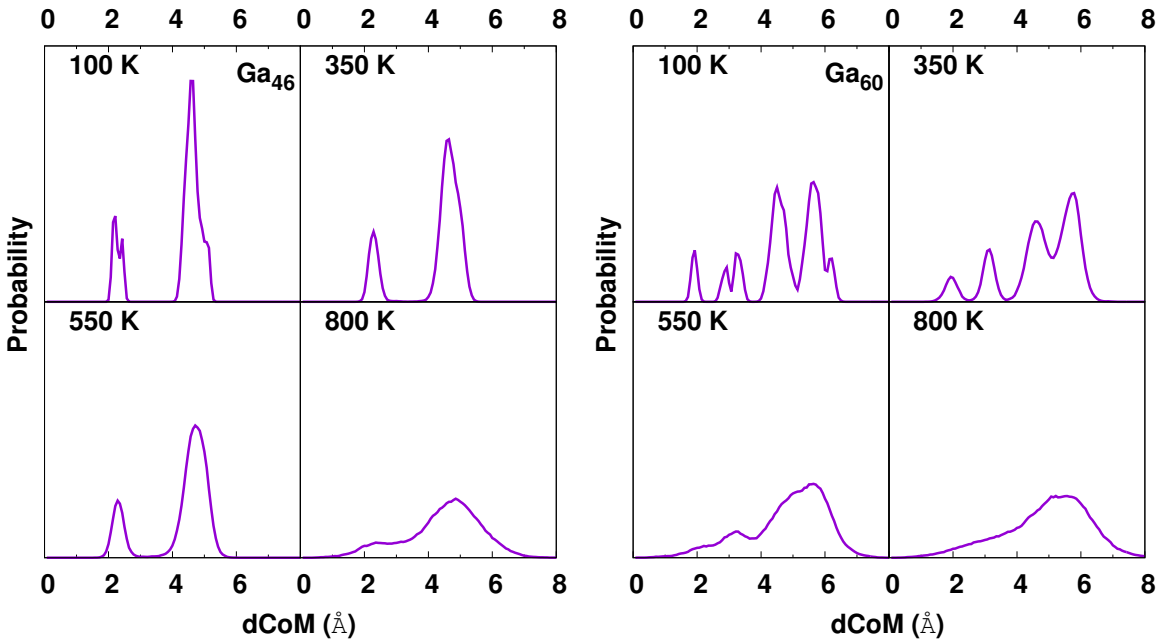

(a) (b)

Figure 4.5: *Distribution of atoms about the center of mass at various temperatures for Ga_{46} and Ga_{60} is plotted in the graphs (a) and (b) respectively. Different isomerisation process at each temperature are indicated from the graphs (See text for further details). The liquid-like state is characterised by the complete structural loss as seen from the plots of 800 K and 550 K for Ga_{46} and Ga_{60} respectively.*

initiates melting at much lower temperatures, while appearance of eCS type isomers up to 600 K delays liquid-like state resulting in a broad transition for Ga_{60}. While δ_{rms} of Ga_{60} (shown in upper right panel of Fig. 4.4) captures the essential features of its melting, it fails to do so for Ga_{46}. Solid-like state of Ga_{60} is signified by the initial constant slope of δ_{rms} till 200 K followed by intermediate stage of isomerization indicated by sudden increase of δ_{rms}. On the other hand δ_{rms} of Ga_{46} shows a continuous increase from 100 K, all the way up to 700 K and beyond.

However, it's C_v signifies a very well defined transition for Ga_{46} and occurs at high temperature around 700 K. Thus, while δ_{rms} captures the premelting diffusion, the actual melting is not well characterized by it.

The observed isomerisation process and the finite temperature behaviour are further clarified by analysing the distribution of atoms about the center of mass of these clusters as a function of temperature. The plots of DCOM at various temperatures for Ga_{46} and Ga_{60} are presented in Fig. 4.5. At a low temperature of 100 K both the systems are in their solid-like state and exhibit a slight thermal broadening due to the oscillations. The GS structural identity is intact even at a temperature of 550 K in case of Ga_{46} though the processes of intra and inter shell diffusions are observed. However, for Ga_{60} at a lower temperature of 350 K the cluster starts to exhibit inter-shell diffusion as seen from the initiation of merging of shells. Further, the complete loss of GS structural motif occurs at a temperature of 550 K and 800 K respectively, for Ga_{60} and Ga_{46} which characterise their liquid-like states.

Low vs high Tm (Ga_{94} vs Ga_{46})

As noted earlier, Ga_{94} is the smallest gallium cluster that melts comparatively at a lower (than that of bulk melting) temperature which is experimentally probed to date. As observed, the T_m of Ga_{94} and Ga_{46} (smallest gallium with comparatively higher T_m) is differ by a value of $\approx$ 500 K. It is interesting to understand the reason behind this large variation. In order to understand this observation, an extensive bondlength analysis is performed on these systems. Since Ga_{94} melts at a temperature lower than the bulk melting temperature, it is preferable to compare the distribution of bondlengths of these clusters with that of Ga-bulk. In case of bulk Ga (α-Ga) the nearest neighbor (NN) distribution consists of a single nearest neighbor at 2.44 Å (one shortest bond), and three pairs of second nearest neighbors (six longish bonds) at distances between 2.69 Å and 2.79 Å. Thus, bulk Ga is composed of short covalent bonds (isolated dimers) connected via longer metallic bonds. That is in bulk the distance between first and second nearest neighbours (three pair) is of the order of 0.2 Å for all the atoms. On a similar note, for the comparison of nearest neighbours distribution, 7NNs of all the atoms in the Ga_{46} and Ga_{94} are calculated, as a function of temperature. In order to compare the NN distribution of these clusters with bulk, the number of atoms in cluster, which behave similar to bulk atoms, are calculated. In simple terms, for a 'XY' pair, the atom 'X' is treated as bulk like if its 1^{st} and 2^{nd} NNs are 0.20 Å apart. The result is pictured in Fig. 4.6 (left panel) for Ga_{46} (red points) and Ga_{94} (green points). The plot indicates that the fraction shows an overall increase with increase in temperature. However, the fraction is slightly larger in case of Ga_{94} for the temperatures in the range 100 K $\leq T \leq$ 600 K. In other words, the fraction is slightly larger after the melting in case of Ga_{46} (simulated T_m of Ga_{46} is 650 K), i.e. in liquid-like state. Further, the fraction reaches a value around 0.40, that means about half of the atoms in these

clusters behave like bulk in their liquid-like state.

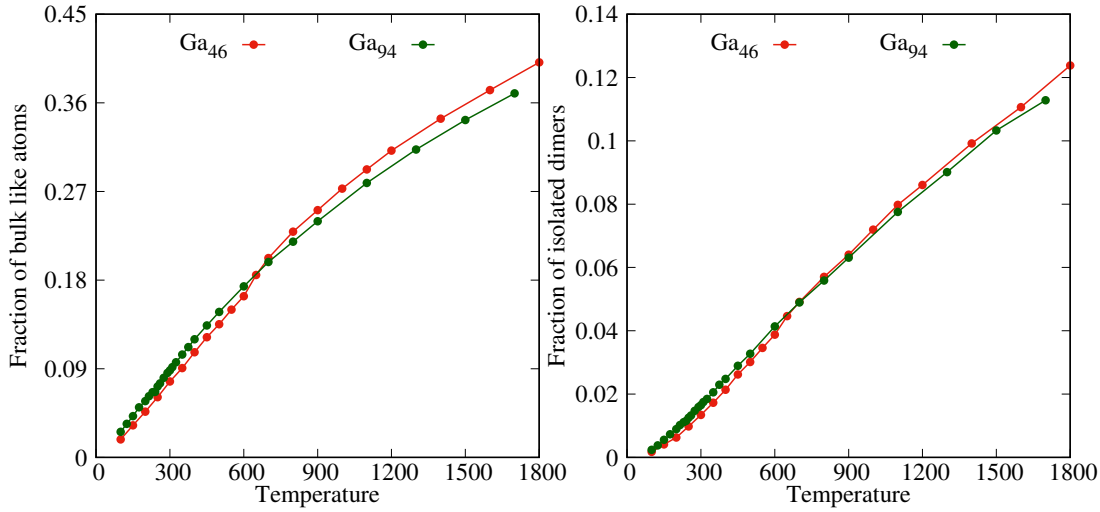

Figure 4.6: *Fraction of bulk like atoms (left panel), and isolated dimers (right panel) as a function of temperature for Ga_{46} (red points) and Ga_{94} (green points).*

Other way to compare the bondlength distributions in clusters with that of bulk is to investigate the formation of isolated dimers. The reason is, in case of bulk all the atoms form an isolated dimer, because their 1^{st} and 2^{nd} NNs are separated by a distance of ≈ 0.2 Å. In clusters the "isolated dimers" are counted by using 0.2 Å as a cutoff for the difference between the first and second nearest neighbours, similar to bulk. For instance, a pair 'XY' is considered as an "isolated dimer" if the 1^{st} and 2^{nd} NNs of both 'X' and 'Y' are separated by a distance greater than 0.2 Å. The fraction of "isolated dimer" as a function of temperature for Ga_{46} (red points) and Ga_{94} (green points), after normalizing with the number of iterations and atoms, is presented in Fig. 4.6 (right panel) As seen from the graph, the trend is quite similar to that of bulk-like atoms (left panel). Though, the fraction is comparatively lower in this case, only 0.12. From this analysis, one could see that the fraction of isolated dimer is comparatively larger for Ga_{94} (similarity with bulk gallium). This may be attributed to the lower than bulk T_m observed in case of Ga_{94}. Furthermore, the bondlength analysis also showed that, 40% of atoms in Ga_{46} have at least two first nearest neighbors (bonds with similar bondlengths), and the number reduces to 20% for Ga_{94}, and in comparison, no atom of bulk-Ga has more than one first nearest neighbor. Thus to conclude, the nearest neighbor distribution of Ga_{94} is closer to bulk in comparison with that of Ga_{46}, which causes Ga_{94} to melt at a temperature comparable to/lower than that of bulk.

Narrow transition in Ga_{94}

Another interesting observation regarding Ga_{94} is, in spite of the distorted nature of its GS, it is observed experimentally that, Ga_{94} exhibits a sharp melting peak in its heat capacity curve.

Calculated C_v of Ga_{94} along with its δ_{rms} are shown in Fig. 4.7. It shows that melting of

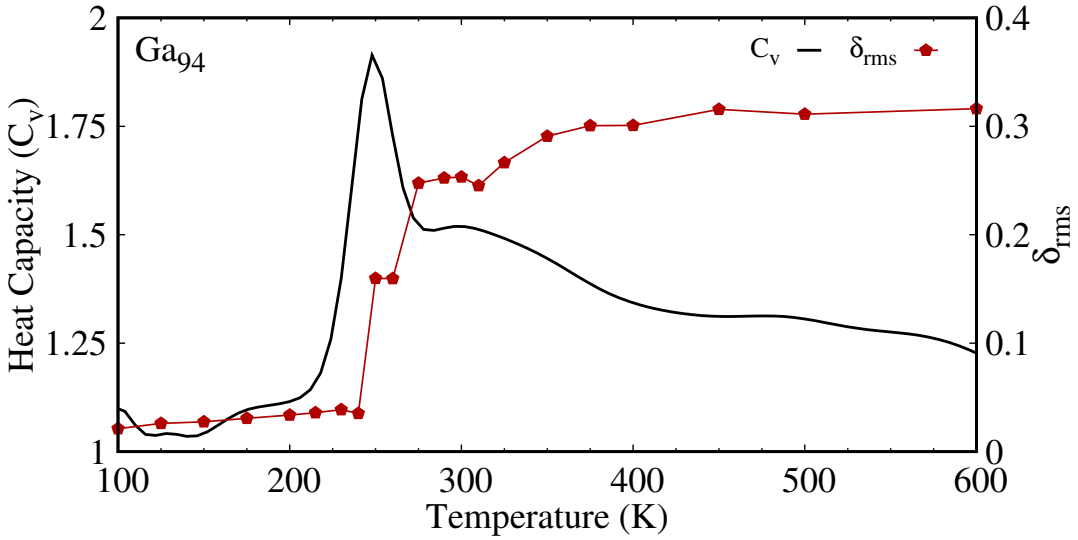

Figure 4.7: *Calculated heat capacity curve (black) of Ga_{94}, along with its δ_{rms} as a function of temperature.*

Ga_{94} occurs quite rapidly with increasing temperature, in agreement with the experimental observation. Melting transition of Ga_{94} occurs over a window of 10 K with a peak at 250 K, which is in close agreement with the measured T_m (286 K). A broad post-melting peak, around 300 K is observed in the C_v of Ga_{94}, which tails gradually till 400 K. An extensive analysis of bondlength distribution (cutoff 2.8 Å) is carried out to understand the sharp vs broad transition in Ga_{94} and Ga_{60}. Bondlengths of Ga_{60} (red graph) along with that of Ga_{94} (green graph) are plotted in Fig. 4.8. Numbers above/below each step in the graph indicate the 'number of atoms' having that particular bondlength. It is seen that for Ga_{94}, size of groups (i.e. number of atoms) with identical bondlengths is extended till 12, while it is lower (1–8 atoms) for Ga_{60}. Thus, although Ga_{94} is disordered, there is an underlying local order in terms of groups of identical bondlengths. Nearly

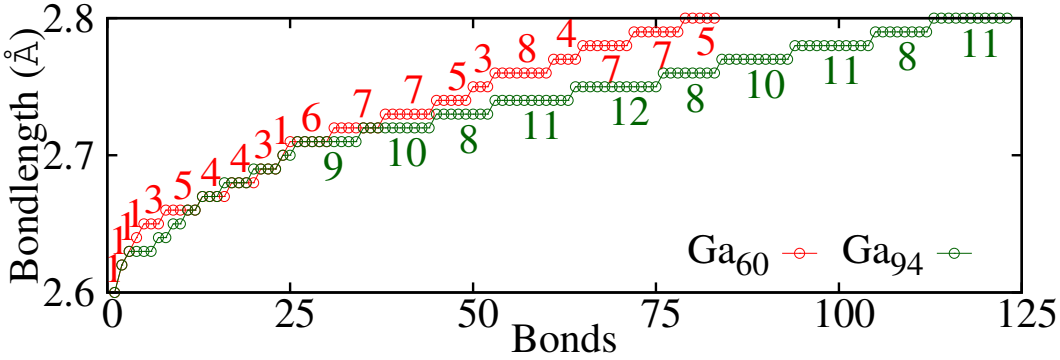

Figure 4.8: *Short bonds of Ga_{60} (red colored points) and Ga_{94} (green colored points). The number of atoms with identical bondlength is mentioned along the groups of identical bondlength for Ga_{60} (top) and Ga_{94} (bottom).*

50% of short bonds of Ga_{94}, which are very crucial in determining the response of a cluster towards temperatures, occur in bunches of 8–12 identical bondlengths. On the contrary, Ga_{60} lacks such grouping of atoms with identical bondlengths. It is worth noting here that, while there are more identical bonds in Ga_{94}, they are not necessarily connected to each other. As has been demonstrated previously, 16 atoms having similar (grouped) bondlengths will respond to external stimulus (like temperature) similarly. Thus, presence of more such atoms, in turn, will leads to a sharper finite temperature transition in clusters like Ga_{94}.

Decrease in Tm with size of the cluster

All the discussions above highlighted the crucial role played by GS motif, in the finite temperature behaviour and isomerisation process of these clusters. A closer look at the different isomer families is presented in Fig. 4.9. Mainly four different isomer families are observed for these clusters, viz., sCS, eCS, Core-Shell-Cap (CSC), and the distorted (D). In all these clusters the first step towards isomerization is ground state modifications. For example, within GSM, a sCS structural motif will retain not only the structural motif but also the distribution of atoms among core and surface shells (green colored bars). The next step is preserving structural motif of the cluster, but variations in the distribution of atoms among different shells (bars with shades of red). Last stage of melting, signified by the distorted isomers (grey colored bars), is common to all three clusters. To make it more clear, the energy span of these different isomer families is

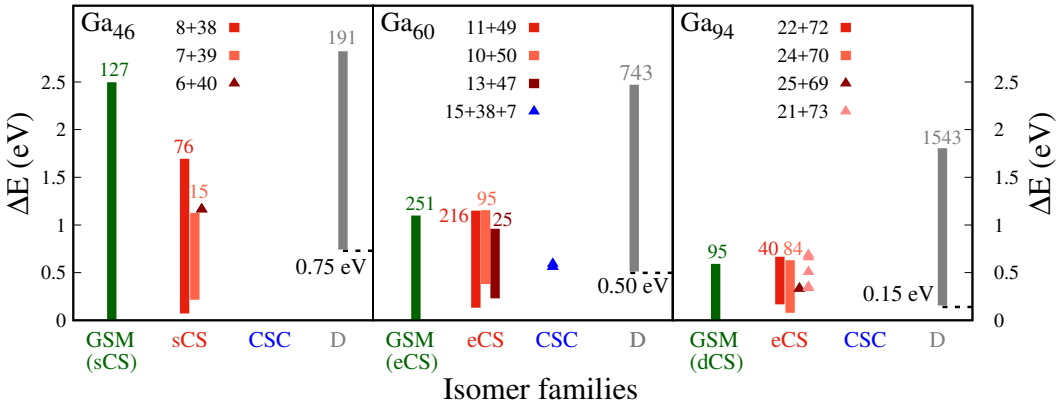

Figure 4.9: *Isomer families of Ga_{46}, Ga_{60}, and Ga_{94} with their energy span with respect to the GS energy (ΔE). Energy required to deform GS like isomers into distorted ones (indicated by a dashed line) decreases, as the size of cluster increases from 46 to 94.*

presented in Fig. 4.9 as histograms. The label (number) adjacent to/atop each bar represents the number of distinct isomers in the respective family. If the number is less than 10, then the family is represented using points (colored triangles), instead of histogram. For Ga_{46}, the isomers are distributed into three main families. First one is the GSM (green bar), followed by sCS (red

bars/points), and distorted isomers (gray bar). The distribution of isomers in sCS shows that the number of core atoms of isomers in this family vary from 6-8 (bars colored in shades of red), which is less than the number of core atoms (9) of Ga_{46} GS, and the isomer with 6 core atoms occurs only once. Also, the energy span of this class is less than that of the GSM family, which reflects the relative high-stability of the sCS motif of Ga_{46} GS. Similar to Ga_{46}, isomers of Ga_{60} are classified into three main families. While GS of Ga_{60} belongs to eCS family, the extended eCS family (red colored bars) is bifurcated into three subclasses. Number of atoms in elongated core vary from 12 in the GS motif, to 10, 11, and 13 atoms in the extended eCS family. The corresponding number of atoms in elongated core and shell is labelled in the graph. Energy span of the three sub-families is comparable to that of the GSM family. This is in general true for other clusters except Ga_{46}. For Ga_{46}, GSM class spans the largest energy range among isomers.Third isomer family of Ga_{60} is CSC (blue triangles), which contains only two members. The distinct isomers of Ga_{94} also distributed in to three different families. The GS of Ga_{94} is dCS and the corresponding GSM family is presented as green histogram along with the number of distinct isomers. The next family of isomers, i.e. eCS and its bifurcations are showed in different shades of red, followed by distorted isomers.

As pointed out previously, appearance of distorted isomers indicates loss of structural identity of the cluster, and its liquid-like state. It is interesting to note that the energy at which the first distorted isomer appears (indicated by a dashed black line in the all three panels of the figure) decreases with increasing size of the cluster. This energy is 0.75 eV for Ga_{46}, 0.5 eV for Ga_{60}, and 0.15 eV for Ga_{94}. Since this energy reflects onset of the liquid-like state, we can directly correlates its decrease with the overall decrease in T_m, as a function of size of the cluster. Another observation, which provides explanation for the observed trend of lowering T_m as a function of size is, based on the bondlength analysis of GS structures of these clusters. The number of shortbonds (cutoff 2.8 Å) per atom reduces from 3 for Ga_{46} to 2.62 for Ga_{94}.

4.4 Summary and conclusions

The difference in structural motif of GS reflects in variation of connectivity of short bonds, as well as the number of short bonds, which are crucial in understanding the finite temperature behavior of clusters. These simulations have reproduced the experimentally observed variations in the melting temperatures as well as melting transitions of gallium clusters. This study explained the underlying process of melting in clusters, and demonstrated that it differs for clusters with different GS structural motifs. The isomerization, which initiates melting in a cluster, does depend upon the structural motif of the respective GS. It is depicted that Ga_{46}, Ga_{60}, and Ga_{94} have different structural motifs which leads to distinct isomerization processes, and in turn different

finite temperature behaviors. Further, the sharper melting transition of Ga_{94} specifically, and in general that of large (100 atoms or more) clusters, is illustrated on the basis of presence of identical bonds, and an inbuilt local order in these large clusters. The lower (than bulk) melting temperature of Ga_{94} is explained on the basis of bondlength distribution closer to that of bulk Ga. Finally, the overall decrease in the T_m with increase in size of the cluster is explained based on the isomer analysis performed on these clusters. Thus, the present study provided a rationale to understand the finite temperature behavior of gallium clusters on the basis of ground state structural motif. This investigation brought out the importance and crucial role of GS in determining the finite temperature behavior of a cluster.

CHAPTER 5

Melting behaviour of clusters with similar ground state structural motif

5.1 Motivation and definition of the problem

The correlation between the GS structural motif and thermodynamic behaviour is demonstrated in the earlier studies and is discussed in the previous chapters. The role of GS structure in the phase transition is also reported in many theoretical investigations.[94, 98, 99, 113, 114, 119, 120] Even if a change in the structural motif of the GS is correlated with variation in the melting temperature, the picture is still not clear. With size of the system, not only the structural motif of the GS changes, but also other factors like, underlying electronic structure, isomer distribution, surface energy, and symmetry of the structure. Thus, even a small variation like addition or removal of a single atom/electron from a cluster results into completely different finite temperature behavior. For example, finite temperature investigations performed on Na_n^q (where q = 0 and $+$, for n = 40 and 41, while for n = 39 the $q = -$, 0 and $+$) clusters showed that the sizes with electronic shell closure, i.e. Na_{39}^-, Na_{40} and Na_{41}^+, melt at a similar temperature of $\approx$ 310 K.[107] Though, the respective GS structures and the nature of transition were different for these clusters. Thus, in this case the T_m was dominantly driven by the electronic structure of the system. Moreover, the electronic stability of Na_{39}^- leads to a sharp peak with high T_m compared to Na_{39} which shares the same GS with Na_{39}^-. Hence, one can see that in the first case, even if the systems possess different GS, the T_m was same (same number of electrons), with slight changes in their nature of C_v. Similarly, in the second example both the nature of transition and melting temperatures were different, despite being the same GS with different charges. Thus in brief, all the factors discussed here as well in previous studies, have complex interdependencies, making it difficult to separate the effect of one factor from the other.

Owing to their interdependencies, it is a challenging task to rationalize the role of structural motif of the GS in the process of melting. However the present investigation addresses this problem by using a system with as many similarities as possible. Al_{36} and Ga_{36} is one such pair of clusters, which possess the same number of atoms, valence electrons, and similar GS structural motif. Thus, the most important factors are same, but with drastically different melting temperatures. The measured melting temperatures of Ga_{36}^{+} and Al_{36}^{+} are 525 K and 834 K, respectively, and are differ by a value of 300 K.[33, 38] Thus, these two systems make a unique pair of clusters to illustrate the exact role of GS motif on the finite temperature behaviour. The extensive thermodynamics performed on these clusters is discussed in the following sections.

5.2 Computational details

BOMD simulations were performed on the neutral systems of Al_{36} and Ga_{36}, as implemented in VASP. PAW method was used for the implementation of pseudo potential formalism. Perdew-Burke-Ernzerhof exchange correlation functional had been used for the clusters. The energy cutoff for each self-consistency iteration was kept as 10^{-4} eV. The GS geometries of Al_{36} and Ga_{36} were reported in the literature. Even if the strategies to locate the GS were different, all the investigations reported the same structure, which is a distorted decahedral fragment.[37, 115, 117, 122, 143] The thermodynamics of both the systems were performed using the reported structural motif. The finite temperature behavior of these clusters was simulated by employing Noŝe thermostat. The initial step of the simulations was a slow heating of the GS from 0 K (T_{ini}) to 100 K (T_{fin}) with a heating rate of 10 K/3 ps. This heating process was repeated by changing the values of T_{ini} and T_{fin}. Then the clusters were maintained at each T_{fin} for at least 150 ps. In the transition regions, the simulation time was more than 400 ps for each temperature. A total of 18 temperatures were simulated for Ga_{36} between 100 K and 900 K, and 19 temperatures for Al_{36} between 100 K and 1200 K, resulting into total simulation time of about 3.8 ns or more for each system. The heat capacity curves were obtained by employing MH technique (See 2.5.3 pg. 32 for details). The finite temperature data was also analyzed using qualitative parameters like root mean square bond length fluctuations (δ_{rms}), mean square displacements, distance of atoms from COM of the cluster, and potential energy distribution as a function of temperature.

5.3 Results and discussion

A comparison study of the ground state structures of Al_{36} and Ga_{36} is presented in the section 5.3.1. Bondlength analysis and the underlying electronic structure also discussed in the section. The finite temperature behaviour along with the simulated C_v and the δ_{rms} is discussed in the section

5.3.2. The isomer analysis is detailed in the section 5.3.3. The outcomes of the present study are discussed in the section 5.4.

5.3.1 The Ground state structure

Similarities

The GS motif found within this simulation study is same as that reported previously. The ground state structure of Ga_{36} and Al_{36} is DDF motif and is shown in Fig. 5.1(a). The distribution of atoms from the COM of the cluster for both the systems is represented in Fig. 5.1(b). The plot clearly confirms that, the GS structure of these two systems is similar. In both the cases the atoms are distributed into three distinct shells and the corresponding shells are labelled accordingly in the graph. The inner and outer shells consist of four atoms and termed as core and edge respectively. The remaining atoms form the surface of the cluster and are distributed into four sub-shells.

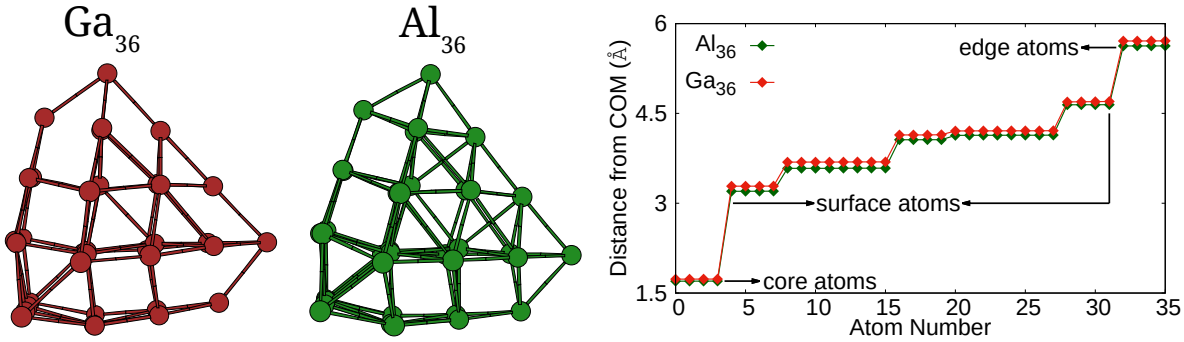

Figure 5.1: *(a) The ground state structure of Ga_{36} and Al_{36}. (b) Distribution of atoms from the center of mass (COM) for Ga_{36} and Al_{36}.*

Differences

Bondlength analysis is performed to understand the underlying bonding present in these clusters, those possess a similar structural motif. The short bonds, i.e. bonds with bondlength $<$ 2.8 Å are presented in the Fig. 5.2(a). Even if both the clusters have the same shortest bond (2.65 Å), the number of short bonds present within the system is different. The plot infers that, Al_{36} possess 92 short bonds, whereas, for Ga_{36} the value reduces to 48. Thus, the number of bonds per atom is 2.5 in Al_{36}, though, for Ga_{36} it is around 1.3 only. Further difference is noticed by examining the distribution of these short bonds within and across the different shells (See Fig. 5.2(b)). The rectangular bars in the graph represent the short bonds present within and between the shells. The color code for each bar is labelled at the top of the graph and the total number of

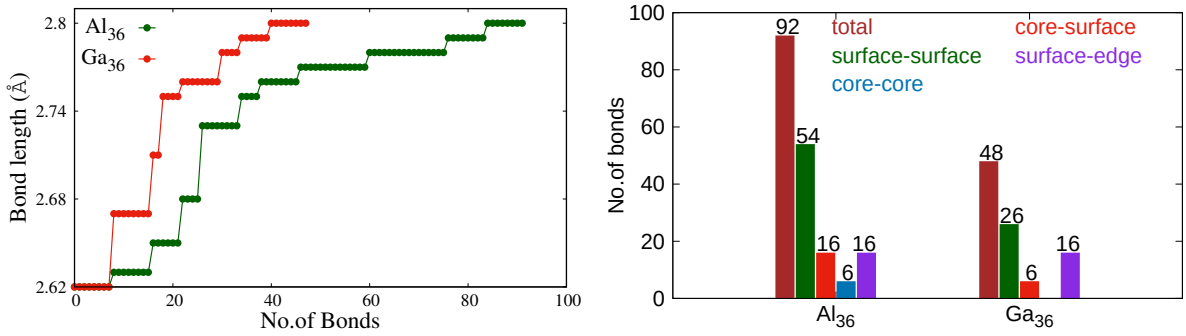

Figure 5.2: *(a) The number of bonds with bondlength less than a value of 2.8 Å for Al_{36} (green graph) and Ga_{36} (red graph). (b) Distribution of short bonds (with cutoff 2.8 Å), between different shells as well as within the shell, for Al_{36} and Ga_{36}.*

the short bonds is marked atop of the corresponding bars. It is seen from the graph, in case of Al_{36} the atoms within the shell and across the different shells are well connected. Though, the connectivity is considerably less for Ga_{36} as seen from the numbers shown in the plot. Further, the core atoms are well connected in case of Al_{36} (6 bonds). On contrary, the core atoms of Ga_{36} are not at all connected, as indicated by a zero value for the core-core connectivity. Thus, even if both the clusters exhibit a same ground state structure, Al_{36} possesses more short bonds which leads to a better connectivity within and between the different shells compared to that of Ga_{36}.

Molecular Orbital (MO) analysis is performed to understand the underlying electronic structure of both the systems. Site projected wavefunction character of each MO, which is calculated by projecting the wavefunctions onto spherical harmonic, is presented in Fig. 5.3. The plot indicates the contribution from 's' and 'p' orbitals towards a particular MO. Hybridisation is observed for a few MOs starting from the 22^{nd} MO, in case of Al_{36} as indicated from the overlap between 's' and 'p' orbitals seen in Fig. 5.3. Whereas, for Ga_{36} there is no overlap between the orbitals, thus no hybridisation. Further, first 15 MOs with atomic 's' as a dominant component clearly follow Jellium like pattern. However, rest of the MOs which are formed out of atomic 's' as well as atomic 'p' do not adhere to the Jellium model very clearly. Out of 54 MOs, both the systems have about 20 MOs similar in character. In short, although the GS of Al_{36} and Ga_{36} has identical structural motif, the underlying electronic structure and resulting bonding is significantly different.

5.3.2 The finite temperature behaviour

Thermodynamic behaviour of these two clusters is simulated to bring out the effects of "similar structural motif with substantially different nature of bonding" on the solid-like to liquid-like transition of these two systems. The phase transition of these systems is characterised by heat capacity curve and δ_{rms} of the clusters, and are shown in Figs. 5.4 and 5.5 respectively.

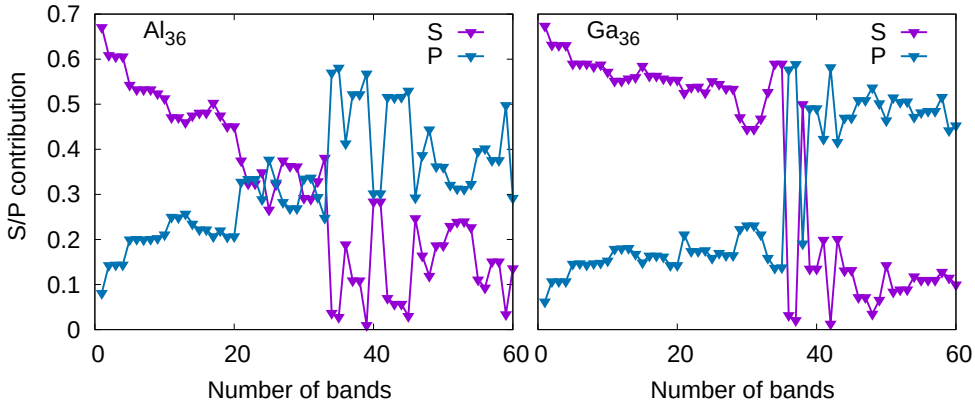

Figure 5.3: *Site projected wave function character of each molecular orbital for Al_{36} and Ga_{36}. The difference in the underlying electronic structure is very clear. For Al_{36} s-p hybridization set in around 22 whereas for Ga_{36} there is no signature of hybridization.*

The simulated melting temperatures of Al_{36} and Ga_{36} are 830 and 580 K respectively, as indicated

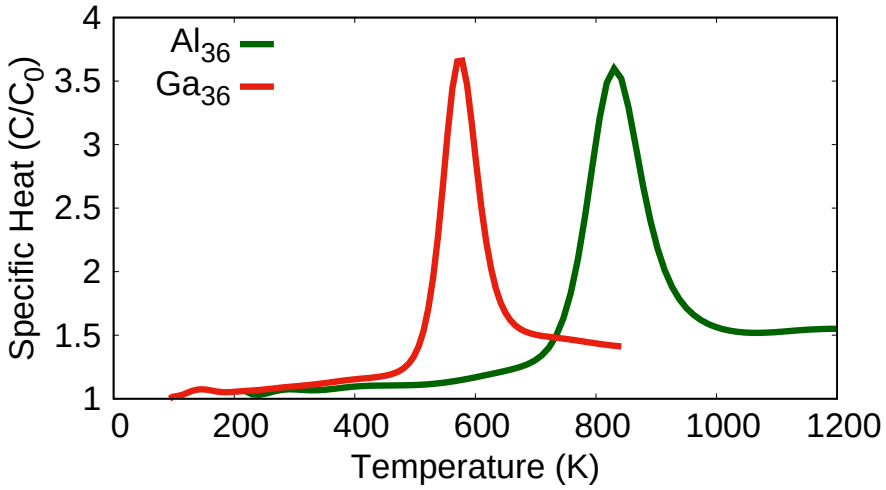

Figure 5.4: *Computed heat capacity curve for Al_{36} and Ga_{36}.*

from the peak of their respective C_v's. Experimentally measured melting temperature of Al_{36} is 834 K, whereas that of Ga_{36} is 525 K which indicates that the first-principle simulations were able to reproduce the experimental trend fairly well. Further, the phase transition is slightly broader for Al_{36} and is more evident from the isomer distribution, which will discuss later. The observed broad transition of Al_{36} is also seen in its δ_{rms} plot. Fig. 5.5 shows the δ_{rms} averaged over 120 ps for each temperature, except for transition region where the averages are taken over 400 ps. The atoms perform oscillations about their mean positions in the solid-like region, and with rise in temperature the amplitude of oscillations increases. This is reflected as a monotonic increment in the value of δ_{rms} and the extend of solid-like region of Al_{36} and Ga_{36} is 700 K and 500 K respectively. The δ_{rms} exceeds a value of 0.1 at temperatures 800 K and 525 K for Al_{36} and Ga_{36},

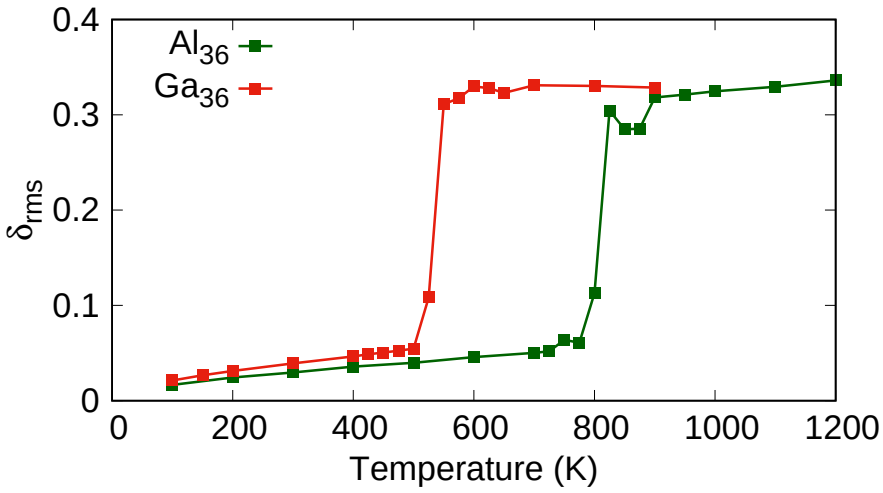

Figure 5.5: *Plot of δ_{rms} as a function of temperature for Al_{36} and Ga_{36}.*

respectively and indicates the isomerisation process. Though, for Al_{36} the isomerisation initiates at a temperature of 750 K which is marked by a small rise seen in the value of δ_{rms}. In both cases, the liquid-like region is identified by the saturation of δ_{rms} and is observed about 900 and 600 K respectively for Al_{36} and Ga_{36}. However, in the transition region, between the solid and liquid like regions, the δ_{rms} shows a fluctuation and the plot indicates a slightly broader transition region for Al_{36} ($\approx$ 750 – 900 K) than Ga_{36} ($\approx$ 525 – 600 K). The HOMO-LUMO gap averaged over the total simulation time for each temperature is shown in the Fig. 5.6. For clarity, the temperatures where the isomerisation sets in, along with those in transition region are highlighted with blue and purple points for Ga_{36} and Al_{36} respectively in Fig. 5.6. The change in the value of averaged

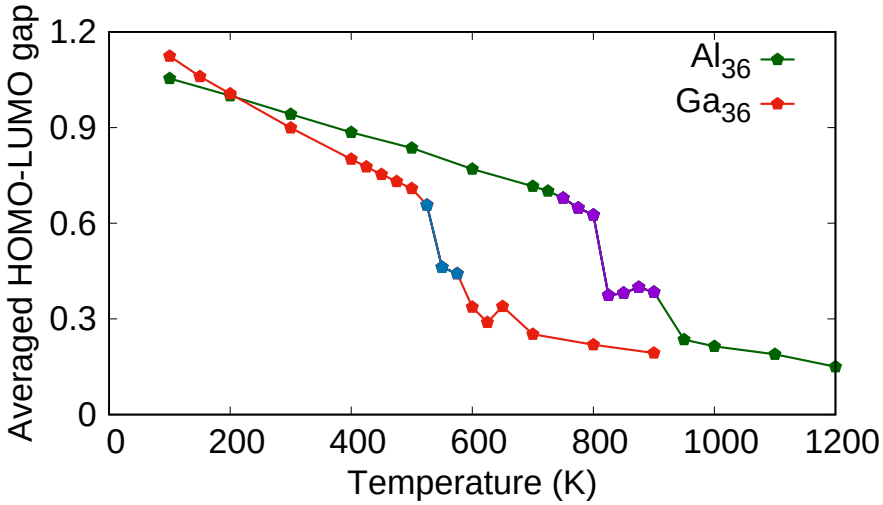

Figure 5.6: *The averaged HOMO-LUMO gap as a function of temperature for Al_{36} and Ga_{36}. The points highlighted with blue and purple color represent the temperatures where the isomerisation begins as well the transition region for Ga_{36} and Al_{36} respectively.*

HOMO-LUMO gap is different at each region. It's value decreases marginally and monotonically in the solid-like region. However, with the isomerisation setting in, i.e. at 750 K and 525 K respectively for Al_{36} and Ga_{36}, the gap decreases rapidly and is steeper in Ga_{36} than Al_{36}. For Ga_{36} till 500 K 54^{th} orbital is HOMO and 55^{th} orbital is LUMO. At 525 K, with on set of isomerisation, for a small fraction of instances (less than 1%), LUMO is shifted to 56^{th} orbital. However, at higher temperatures, there are increasing instances where 54^{th} and 55^{th} orbitals become degenerate and 56^{th} orbital is LUMO. For Ga_{36} at 800 K 26% of times LUMO is shifted to 56^{th} orbital. The analysis also showed that for a very few times (less than 1%) 54^{th}, 55^{th}, and 56^{th} orbitals are degenerate with 57^{th} orbital as LUMO. In case of Al_{36}, before isomerisation sets in, i.e. up to 725 K, HOMO is 54^{th} orbital and LUMO is 55^{th} orbital. With isomerisation, for a small fraction of instances (less than 1%), LUMO is shifted to 56^{th} orbital. This fraction increases at higher temperatures. For example, 41% of times LUMO is located at 56^{th} orbital for Al_{36} at 1100 K. Further, the degeneracy between 54^{th}, 55^{th}, and 56^{th} orbitals is observed with marginally more probability (more than 1%). This is reflected in the averaged HOMO-LUMO gap as shown in Fig. 5.6. The variation in the HOMO-LUMO gap at a specific temperature associates well with the isomerisation pattern observed at that temperature. In short, both the systems have striking similarity in the nature of heat capacity curve, δ_{rms} as well as in the averaged HOMO-LUMO gap. However, the nature of transition is slightly broader for Al_{36} and the temperatures at which different processes occur, like isomerisation and melting, are substantially different for these systems.

5.3.3 The isomer distribution

Extensive isomer analysis is performed to shed more light on the way GS influences the melting transition. The initial geometries are selected from each finite temperature MD run (equally spaced, unbiased). At least 50 local optimizations are carried out per temperatures, though for transition region, the number of local optimizations carried out is about 100 or more, owing to longer MD trajectories. All these local optimizations resulted into at least 300 distinct isomers for each system. It has been confirmed by vibrational analysis that these are indeed local minima. For both the systems, the entire distinct isomers can be grouped into two families and are termed as class-I and class-II. Representative isomers of both the classes are shown in Fig. 5.7 and 5.8. The "class-I" isomers posses the structural motif which is same as that of the GS and are shown in blue color in Fig. 5.7. However, one or two atoms get displaced from their edge position compared to the GS structure. The displaced edge atoms are shown as white spheres in Fig. 5.7. The energy difference with respect to the GS (ΔE measured in eV), is shown at the base. The ΔE of class-I isomers of Al_{36} is shown in green and that of Ga_{36} is shown in red. It is instructive to note that, the 1^{st} isomer

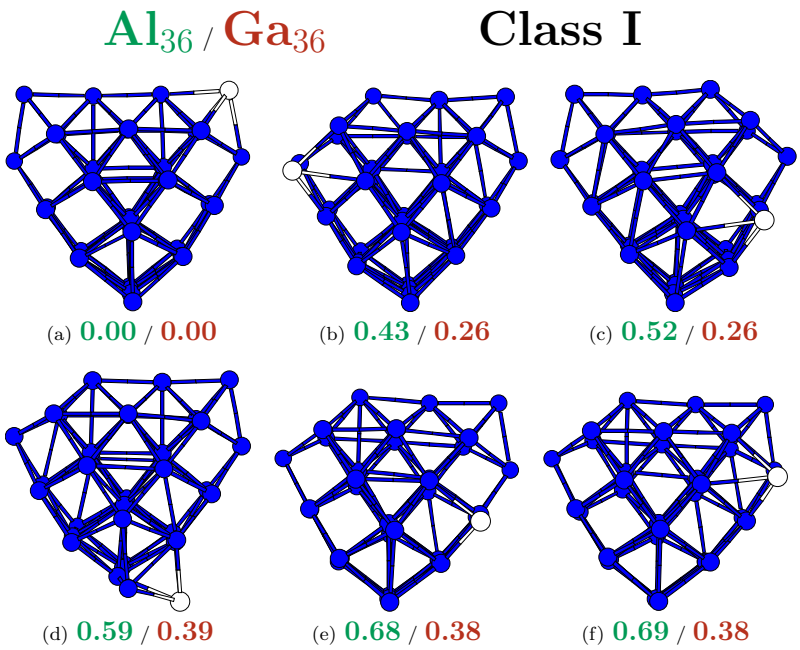

Figure 5.7: *Class-I isomers: isomers having same structural motif as that of GS. The white atom indicates the displaced atom. The numbers at base represent difference in energy with respect to the GS energy in eV and are highlighted by green and red color for Al_{36} and Ga_{36} respectively.*

appears at 0.26 eV above the GS in case of Ga_{36}, and for Al_{36}, the same appears at a higher ΔE of 0.43 eV. One can note the correlation between the ΔE of I^{st} isomer and the short bonds per atom present in the cluster. The number of short bonds per atom for Al_{36} is almost double (2.5) than in Ga_{36} (1.3), similarly the value of ΔE (0.43 eV of Al_{36} is $\approx$ higher, by a factor of two, than 0.26 eV of Ga_{36}). Further, ΔE depends upon the position of the displaced atom, for example, in Ga_{36}, the energy barrier does not depend much on whether the displaced atom resides, on the nearest surface or at the nearest position. However, same situation in case of Al_{36} costs more energy as can be seen from energies shown for class-I isomers in the figure. For Ga_{36}, once the initial barrier is crossed it does not require more energy to hop from one site to other on the same surface (Refer ΔE of Ga_{36} in Fig. 5.7b and c). Though in Al_{36}, hopping from one site to another on the same surface also requires energy of the order of 0.1 eV (Refer ΔE of Al_{36} in Fig. 5.7b and c). Class-II isomers are high energy isomers those occur mainly after the melting process. These isomers posses completely different structural motif than that of the GS and are presented in Fig. 5.8 along with the ΔE of the isomer. The energy at which the class-II isomers appear follows the same trend as observed in case of class-I isomers. In other words, the ΔE of the isomer of Al_{36} is higher in comparison to that of Ga_{36}. For instance, in Ga_{36}, the first isomer from this class appears at 0.67 eV higher than the GS. However, the first isomer belonging to this isomer family appears at 1.2 eV higher than the GS for Al_{36}. In addition to this, the isomer analysis showed that the energy span of class-I isomers for

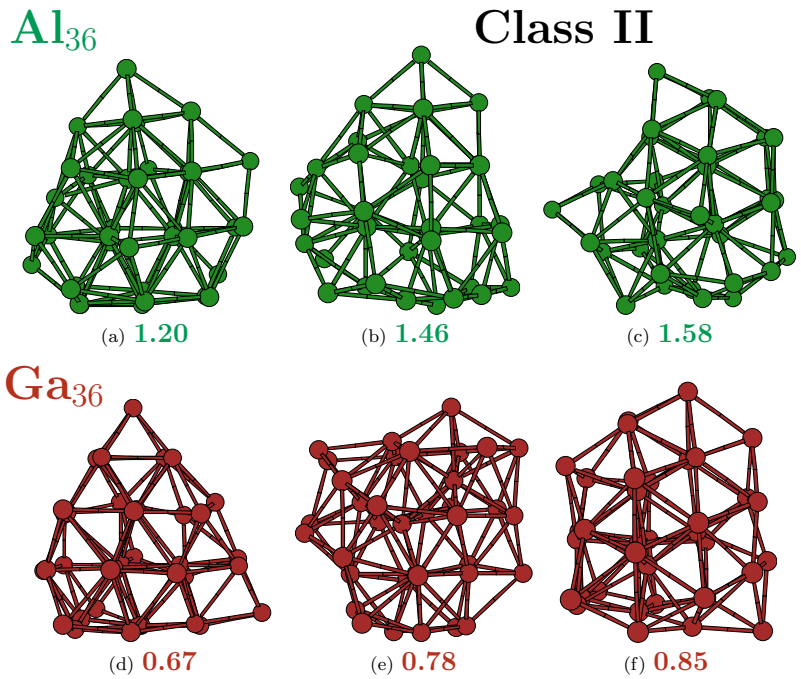

Figure 5.8: *Class-II isomers: High energy isomers of Al_{36} and Ga_{36} are shown in green and red color respectively. The numbers at base represent difference in energy with respect to the GS energy in eV.*

Al_{36} and Ga_{36} are in the order of about 0.9 and 0.5 eV respectively.

The isomer energies (ΔE) as a function of temperature are pictured in Fig. 5.9 for Al_{36} (left panel) and Ga_{36}(right panel). The energy till which the class-I isomers appear is marked by black dotted line in the plots for both systems. From the graph it is seen that, for Al_{36}, the isomerisation begins at 750 K, whereas for Ga_{36}, the first isomer appears at 525 K. Further, in case of Ga_{36}, both families of isomers are accessible at 525 K whereas for Al_{36}, up to 800 K, dominant isomers belong to class-I. These observations are consistent with the δ_{rms} and the slight increase observed at 750 and 775 K in case of Al_{36} is due to the presence of class-I isomers and indicates the beginning of isomerisation. Whereas, the sharp rise at 800 K and 525 K for Al_{36} and Ga_{36} is attributed to the appearance of isomers of both classes. As noted earlier, when the cluster is in liquid-like state, most of the isomers belong to class-II. Additionally, probability to visit GS or class-I isomers is much less in liquid-like state. All these observations are further presented in Figs. 5.10 and 5.11. Thus, this isomer distribution infers about the transition temperatures of both the clusters. For Al_{36}, the transition region is 750 K to 900 K, whereas it is 525 K to 600 K for Ga_{36}. Note that, for Al_{36}, the width of the transition region is almost double than that of Ga_{36}. These observations are also consistent with the δ_{rms} and heat capacity curve of these two systems.

In Figs. 5.10 and 5.11, isomer energies are plotted for three temperatures, which represents the isomerisation, transition region and liquid-like state.The initial geometries for these optimizations

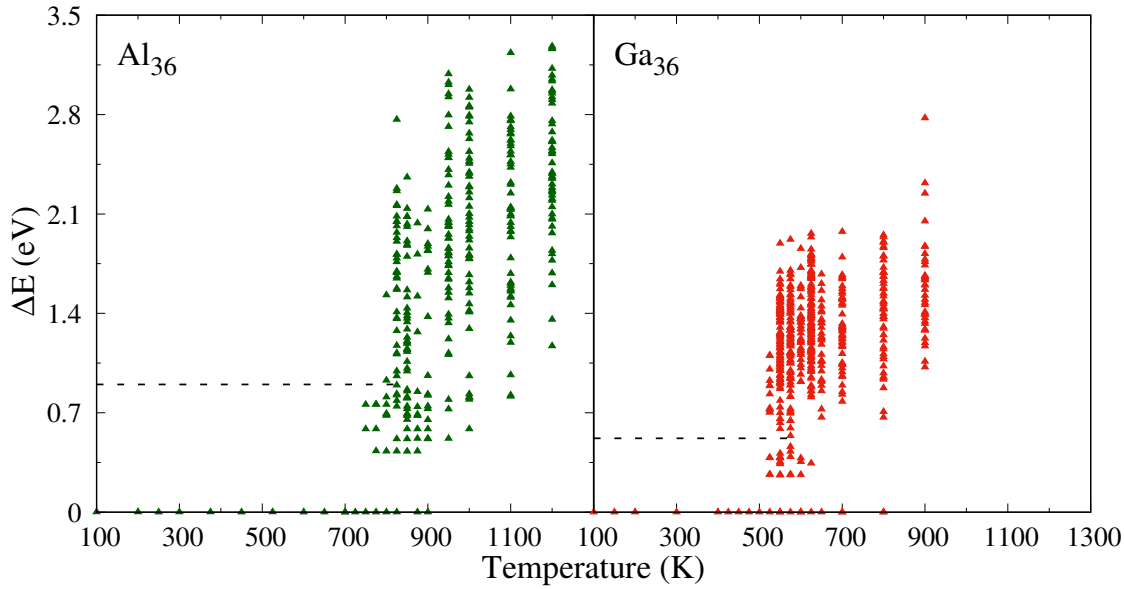

Figure 5.9: *Distribution of distinct isomers at different temperatures for Al_{36} (left panel) and Ga_{36} (right panel). The black dotted lines at 0.9 eV and 0.5 eV represent the energy range till which the class-I isomers appear for Al_{36} and Ga_{36} respectively.*

were picked up (equidistant and unbiased) from the finite temperature data. Hence, the x-axis also represents the time scale. For instance, the initial structure of n^{th} isomer is picked up after $3n$ ps of MD simulation. For Al_{36} (see Fig. 5.10), the selected temperatures are 775 K, 800 K, and 850 K. As noted previously, although the isomerisation begins at 750 K for Al_{36}, up to 800 K, class I isomers ($\Delta E < 1.0$ eV) are dominantly observed, which is evident from the figure (shown with

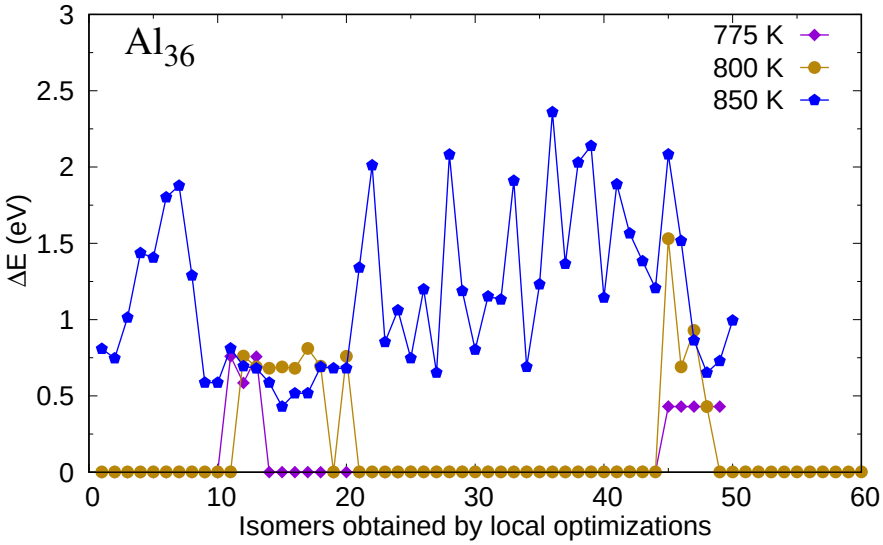

Figure 5.10: *Isomers obtained by local optimization for the temperatures in the transition region and after melting for Al_{36}.*

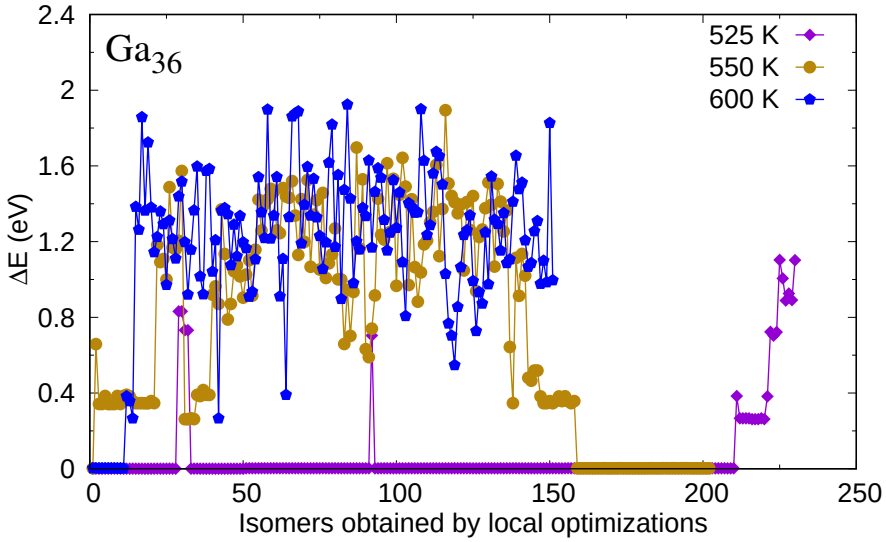

Figure 5.11: *Isomers obtained by local optimization for the temperatures in the transition region and after melting for Ga_{36}.*

golden points in Fig. 5.10). With increasing temperature, class-I isomers become less probable and at 850 K, most of the isomers belong to class-II (shown with blue points in Fig. 5.10). In case of Ga_{36} at 525 K both type of isomer families are present, and is clear from the energy span of the isomers accessible at that temperature (class-I $<$ ΔE $\approx$ 0.5 eV $<$ class-II, purple points). Similar to Al_{36}, at higher temperatures class-II isomers become more frequent. In addition to this, after the complete melting, both the GS and class-I isomers hardly occur. To conclude, the isomer analysis is crucial in understanding the finite temperature behavior of the cluster.

5.4 Summary and conclusions

Extensive finite temperature analysis is performed on two clusters, Al_{36} and Ga_{36}, having identical ground state motif and number of valence electrons. The underlying electronic structure and the bonding are explored by examining different ground state properties. The analysis showed that the atoms in the Al_{36} are highly connected compared to Ga_{36}. Similar to this, a subtle difference is observed in the nature of MOs present in the system. For Al_{36}, a 'sp' hybridisation is observed which is not the case for Ga_{36}. Thus, the study brought out that, even if the systems possess similar GS motif the underlying electronic structure is different. Investigated the effect of the similar structural motif on the finite temperature behavior of the cluster by employing Born-Oppenheimer molecular dynamics simulations. The simulations were able to reproduce the experimentally observed trends quite well. The C_v of Al_{36} is slightly broader and is explained based on the isomer analysis. The detailed isomer analysis revealed that, the isomers which are more probable before cluster melts, have striking similarities and do have strong influence of the

GS structure (class-I). Further, a direct connection is observed between the higher connectivity (more short bonds) and the ΔE of the isomers. For instance, in case of the well connected Al_{36} the isomers appear at a higher ΔE as well the isomerisation begins comparatively at a higher temperature. Moreover, liquid-like state may be characterized by the absence of GS/class-I isomers.

CHAPTER 6

Multifaceted Thermodynamics of Pb_n (n = 16–24) Clusters

6.1 Motivation and definition of the problem

The trends of global minimum energy structures (GS) of small clusters in their thermodynamic analysis exhibit an important and central role as described in the previous chapters. However in those studies the simulations were performed mainly on a few systems which represent the overall behaviour observed in the process of melting. Investigating the thermodynamics of a series of clusters will lead to a better understanding about the process. On these lines, an extensive finite temperature study is performed on nine small lead clusters in the size range, n = 16–24. The motivation for this size range is two fold in nature. Firstly, all the previous investigations about Pb clusters in this size range were concerned with their geometries, bonding, electric dipole moments, and electronic structures.[152–157] However with the exception of work done by Pushpa et al., there exists no first principle studies that discuss the thermodynamics of small Pb clusters.[158] In this study, Pushpa et al. related the stiffness of bonds in small ($<$ 20 atoms) Pb clusters with their melting behaviour. Shorter and stiffer bonds of these clusters in comparison to bulk imply that the clusters melt at temperatures higher than bulk. Accordingly, they proposed that these small Pb clusters will exhibit an elevation in their melting temperatures.[158] Secondly, by means of experimental and theoretical studies it was showed that the nature of bonding in small Pb clusters is different from that of bulk. Furthermore, with increase in size of the cluster, these undergo a non-metal to metal transition. Even if there exist a conflict in the size range at which the bonding changes, it is interesting to understand the impact of change in the nature of bonding on the melting.[159–161] Since the experimental analysis concluded that the transition occurs at a size around 20 atoms,[160] the present study also

considering the same size range.

6.2 Computational details

Finite temperature simulations were performed using BOMD as implemented in VASP. Interactions between the core and valence electrons were described by the PAW pseudopotential, with GGA and the PBE exchange-correlation functional. The valency of Pb atoms was taken as 4, with valence configuration $6s^2$, $6p^2$. All calculations were carried out by incorporating the effect of spin-orbit coupling. The size of the simulation box was 25 Å, which was found to be sufficient for the energy convergence, and the vacuum between two images was 16 Å. The criteria for convergence in energy for each self-consistency iteration was kept as 10^{-4} eV. The canonical ensemble molecular dynamics simulations were performed using a Nosè thermostat. The procedure used for performing finite temperature calculations of these systems was as follows. The simulations were initiated with already published ground state structures of Pb_n clusters, heated to 100 K in 15 ps.[152–156] After the first heating, the rest of the simulations involved two simultaneous simulations as follows. The method was (i) heating the system at a rate of 50 K/15 ps to the next temperature and (ii) maintaining the system at that temperature for at least 210 ps. Since the time needed for thermalization is more in the transition region, the system was maintained for 300 ps or more in this region. It was observed that all clusters undergo fragmentation at higher temperatures, instead of melting. Hence the simulations were performed for a number of temperatures, ranging from 14 to 17 in a temperature range 100 K to the fragmentation temperature (T_{frag}). The resulting total simulation time varied from 3.4 to 5.37 ns for different sizes. Details about number of temperatures and total simulation time for each system, along with their fragmentation temperatures, are presented in Table 6.1. The finite temperature data was analyzed using different tools like δ_{rms}, distribution of atoms with respect to their distance from center of mass of the cluster, MSD, distance-energy plots, and heat capacity curves.

Cluster Size	16	17	18	19	20	21	22	23	24
No. of Temperatures	17	16	15	13	15	12	14	15	15
Total Simulation time (ns)	5.13	4.26	4.09	3.90	3.45	3.30	5.17	4.85	4.92
T_{frag}(K)	900	850	750	650	750	550	700	750	750

Table 6.1: *Details about the simulation data. 1^{st} row is the size of the system. Total number of temperatures for each system with corresponding total simulation time (in ns) are in the 2^{nd} and 3^{rd} row respectively. Last row contains their fragmentation temperatures (T_{frag}).*

Local optimizations were carried out using geometries picked out from the finite temperature MD data. These initial geometries were selected in a manner that they were unbiased and equally

spaced (each geometry after a period of 3 ps) which resulted in at least 1000 initial geometries per system. An extensive isomer analysis was carried out using these optimized structures. For local optimization, the convergence criteria for forces on each ion was taken as 0.005 eV/Å. Vibrational frequencies were calculated for GS of all the sizes, to confirm that the obtained geometries were indeed a local minima.

6.3 Results and discussion

6.3.1 The Ground state structures

The putative global minima for Pb clusters in the size range 16–24, is shown in Fig. 6.1. The GS of all these systems was located by a two step process. In the first step nearly 3-5 ns of BOMD was performed by using the previously published structures.[152–156] In the next step, about a thousand initial positions were optimized from this MD data for each size before concluding the search for their GS. The revised or otherwise, GS structures from this search were used as the starting point of the thermodynamics runs, the details of which are listed in Table 6.1. With such a large data set, the GS structures used to initiate the thermodynamics become most reliable to explain the structure dependent finite temperature properties of these small clusters. The salient features of these structures are interesting by themselves and will be used later to explain their thermodynamic behaviour. A new GS structure is obtained for size 20 in this investigation. It has not been previously reported in the literature. Although the earlier reported structure of Pb_{20} composed of a single added atom at the center of Pb_{19} GS (shown in Fig. 6.1), the newly found structure is without an internal atom, and its energy is 0.17 eV less than that of the previously reported GS.[153, 156] This makes Pb_{20} the only other structure that is without an internal atom, besides Pb_{16}. Pb_{20} is also the only other GS that is not prolate, along with Pb_{17}. The other nonprolate geometry, Pb_{17}, has the most symmetric GS among all other sizes. All the geometries except Pb_{17} and Pb_{20} are prolate and are formed by stacking rings of Pb atoms. Number of atoms in the rings vary as the size changes, and the three stacks of rings grow to four rings and an apex atom as the cluster grows in size from 16 to 24 atoms. The more stable Pb_6 and Pb_7 units are seen in almost all of these structures. In summary, all the studied clusters have a prolate structural motif except Pb_{17} and Pb_{20} with Pb_{17} being the most symmetric structure among all. Pb_{16} and Pb_{20}, are the only ones without any explicit central atom. This specific feature is the cause of the solid-solid transition observed during their thermodynamics, which will be discussed later. Further, the stable Pb units present in their GS has an important influence in their finite temperature behaviour, which will be explained later.

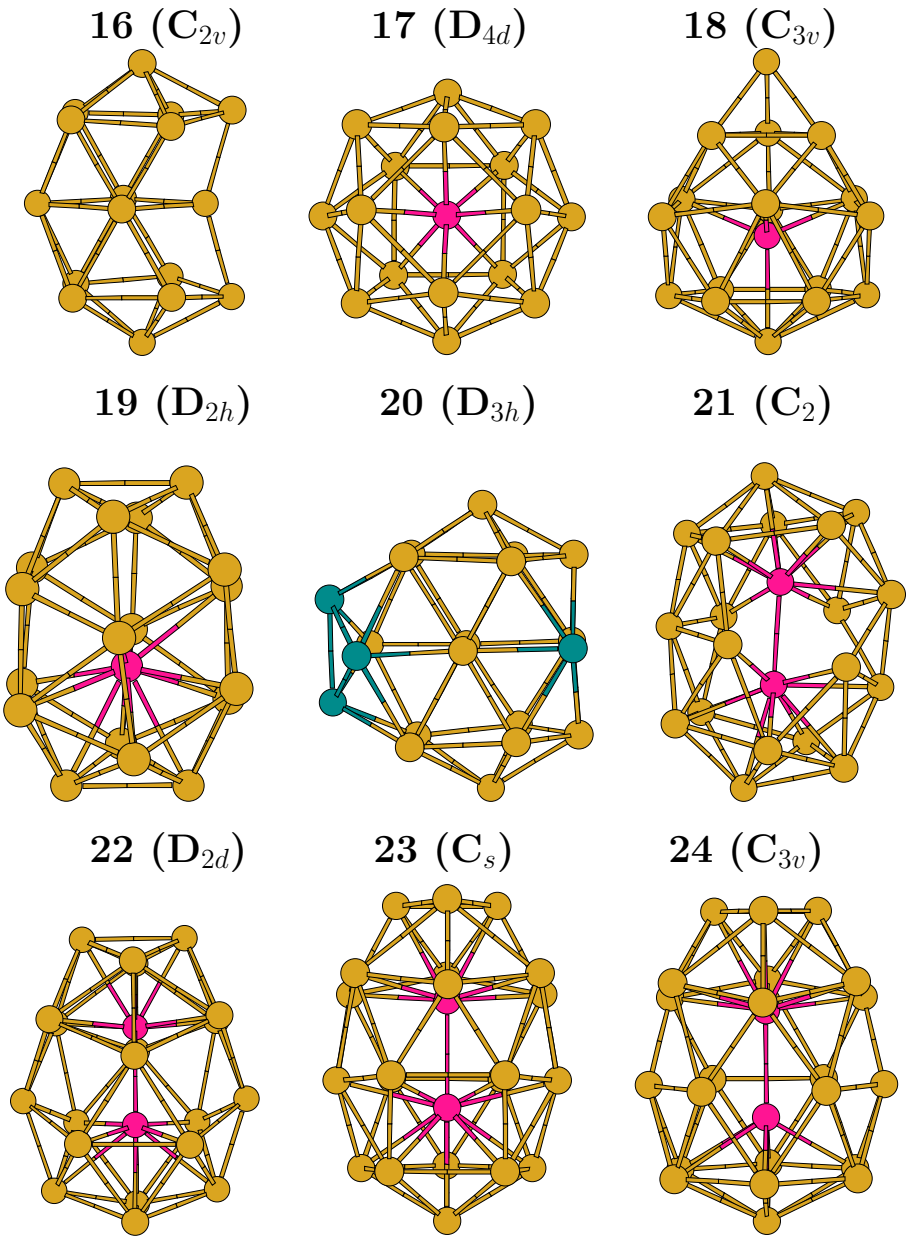

Figure 6.1: *Ground state structures of Pb_n (n = 16–24) clusters. Sizes of clusters are mentioned at the top of each structure, along with their symmetry groups in the parentheses. The internal atoms are shown in pink. In the case of Pb_{20}, the four atoms shown in cyan color are additions to the Pb_{16} motif.*

Bonding

The nature of bonding present in small Pb clusters has been an issue of debate in the past and is not yet resolved.[159–161] An extensive analysis is performed by employing different analysis techniques to gain insight about bonding in Pb clusters. This includes the analysis of molecular orbitals, coordination of atoms within the cluster and electron localization function. The widely accepted model, which is used to conclude whether a system is metallic or not is the Jellium model.

In the present study, two factors are considered to decide whether a cluster follows the Jellium model or not. The first one is the observed degeneracy in eigenvalue spectra and its resemblances with that of Jellium spectra, and the second one is shape of the MOs and their resemblance with the characteristic shapes of Jellium MOs. Hence, if the degeneracy pattern as well as the shape of MOs follow the Jellium trend, then it is concluded that the system under study follows the Jellium model. The analysis showed that MOs formed out of atomic 's' orbitals are the only ones that follow the Jellium model (in terms of degeneracy as well as shape of MOs). The rest of the MOs mostly form p-complexes in accordance with symmetry of the cluster. Since there are two valence 's' electrons per Pb atom, only n orbitals can be occupied by these $2n$'s' electrons in a cluster Pb_n. Table 6.2 gives detailed statistics on the extent to which the MOs of Pb clusters follow Jellium orbitals. It is intriguing to note that, only for Pb_{17}, a maximum of all 17 MOs (formed out of atomic 's' orbitals) follow Jellium orbitals. For rest of them, less than n (between 50% to 90%) MOs (formed out of atomic 's' orbitals) follows Jellium, in an 'n' atom cluster. Interestingly, such

Size	16	17	18	19	20	21	22	23	24
s MOs†	12/16 (75%)	17/17 (100%)	13/18 (72%)	12/19 (63%)	15/20 (75%)	16/21 (76%)	14/22 (63%)	13/23 (57%)	10/24 (42%)
p MOs‡	0	3	1	0	3	0	2	1	3

Table 6.2: *Molecular Orbitals of Pb clusters compared with Jellium MOs. s MOs†: MOs formed out of atomic s, and follow Jellium orbitals. p MOs‡: MOs formed out of atomic p, and follow Jellium orbitals.*

a partial/characteristic similarity of MOs with Jellium has been also seen in clusters of gallium and of aluminum. Thus, similarity of "MOs formed out of atomic s" with those of Jellium orbitals is not just Pb specific but seems to be a trait common to other small clusters. The coordination analysis performed in these clusters is summarized in Fig. 6.2. It plots the fraction of atoms with their coordination number against size of the cluster. The analysis is carried out with a cutoff bond length of 3.8 Å. The cutoff is chosen on the basis of the distribution of bond lengths, which shows a gap at the value of 3.8 Å, indicating the bifurcation of first nearest neighbors from the further nearest neighbors. The number at top of each histogram indicates the coordination and the y-axis plots the fraction of atoms with a specific coordination. For example, in case of Pb_{17}, the same fraction of atoms (8 out of 17) has 5- and 6-coordination. It is noted that the coordination of these clusters shows an increasing trend in general (Fig. 6.2). A lower coordination of 4 occurs only in Pb_{16}, after which the fraction of atoms with coordination 5 or 6 goes on increasing with the cluster size. Since metals possess a higher coordination, it can be concluded that Pb clusters become relatively "more" metallic with increasing size.

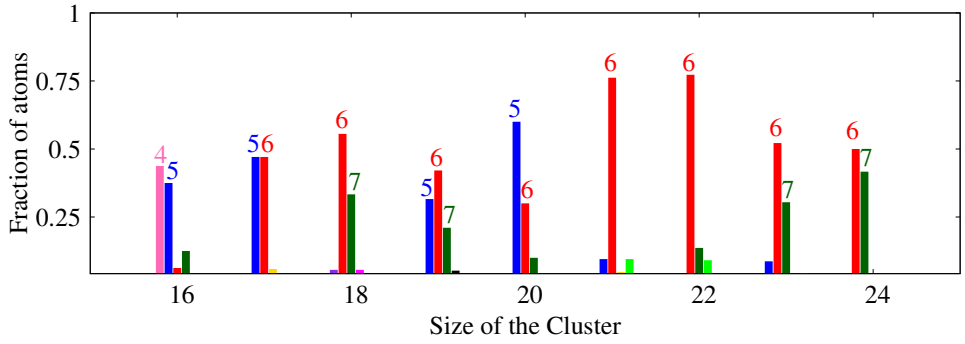

Figure 6.2: *Numbers at the top are the coordination numbers plotted as corresponding colored vertical bars against the fraction of atoms with that coordination for all the clusters.*

6.3.2 The finite temperature behaviour

A detailed account of thermodynamic behavior of these clusters, discerned using different theoretical quantities like the δ_{rms}, radial distribution function about center of mass of the cluster, detailed analysis of MD trajectories, and isomer analysis using DE plots is discussed in the following sections.

Fragmentation

All Pb clusters between sizes 16 and 24 undergo fragmentation at elevated temperatures. Fig. 6.3 shows the fragmentation temperatures of these clusters as a function of their size. It is noted that all these Pb clusters except Pb_{21}, fragment above their bulk melting temperature ($T_{m[bulk]}$). This agrees well with the prediction from the previous work which states that Pb clusters will be stable above $T_{m[bulk]}$.[158] The fragmentation temperatures vary in the range of about 350 K, from 550 K for Pb_{21}, to 900 K for Pb_{16}. The energy needed for the systems to undergo fragmentation, i.e. fragmentation energy (E_{frag}), is calculated. For a cluster of size n that fragments into two smaller clusters of sizes m_1 and m_2, the fragmentation energy is defined as

$$E_{frag} = (E^{GS}_{m_1} + E^{GS}_{m_2}) - E^{GS}_{n},$$

where, $E^{GS}_{m_1}$ and $E^{GS}_{m_2}$ are energies of the GS structures of the fragments of cluster, E^{GS}_{n} is the energy of the GS of cluster of size n, and $n = m_1 + m_2$. A plot of this quantity for all Pb clusters between sizes 16 and 24 is shown in Fig. 6.4. For each of the clusters, different fragmentation channels are observed during MD, represented by bars in Fig. 6.4. The multiple bars for each cluster in the plot imply different possible ways in which a particular cluster has fragmented during the MD. Specifically, Pb_{16} has two possible channels of fragmentation, (7,9) and (8,8). Further, the most probable fragmentation channels have the least fragmentation energy. For

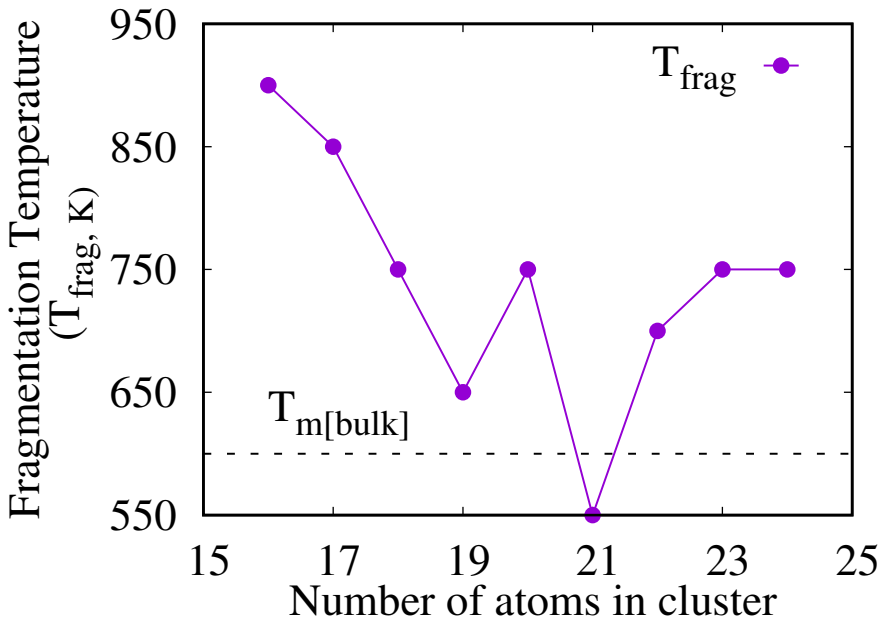

Figure 6.3: *Fragmentation temperatures (T_{frag}) of Pb_n (n = 16–24) clusters. $T_{m[bulk]}$ is the melting temperature of bulk Pb. Fragmentation temperatures for all sizes except Pb_{21} are above that of melting temperature of bulk Pb (600 K).*

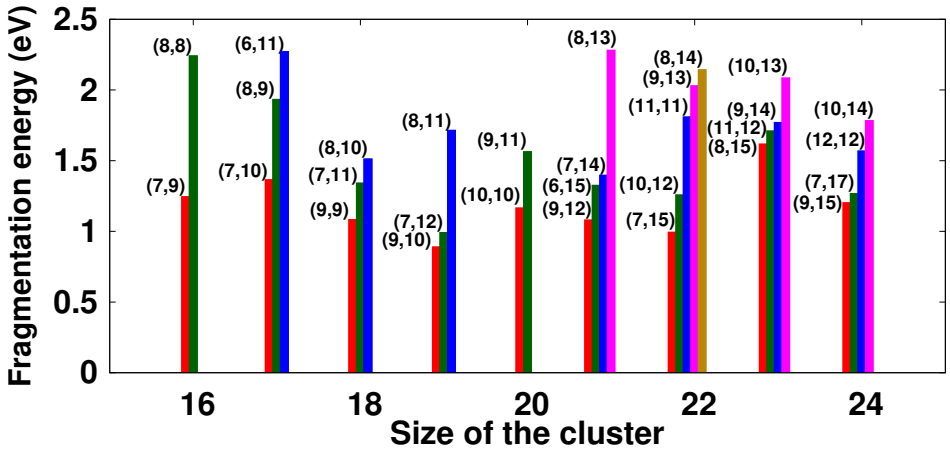

Figure 6.4: *Fragmentation energies of Pb_n ($n = 16 - 24$) clusters. Numbers in the brackets correspond to the sizes of the fragments. Multiple data bars imply that cluster has fragmented in more than one ways during the MD.*

instance, (7,9) is the most probable channel observed in MD simulations in case of Pb_{16} at fragmentation temperature and indeed has much less fragmentation energy compared to any other possible fragment (8,8). However, when the difference in fragmentation energy is less than 0.2 eV the corresponding fragments are observed with the similar probability. For example, in case of Pb_{23}, fragmentation channels (8,15), (11,12), and (9,14) are observed with same probability during the MD. Further the fragments with sizes 7, 9, or 10 are ubiquitously present for all clusters. It has been found experimentally that Pb clusters of sizes 7, 9, and 10 are the most abundant in their

mass spectra, which implies that they are the most stable sizes of Pb clusters.[162]

Root Mean Square Bond Length Fluctuations (δ_{rms})

The δ_{rms} for Pb_n (n = 16–24) clusters, as a function of temperature is plotted in Fig. 6.5. It is interesting to note that these δ_{rms} plots look quite atypical when compared with the schematic shown in Fig. 2.2 in Sec. 2.5.2 (See pg. 32). The solid state of clusters of Pb_{17}, Pb_{18}, and Pb_{20} exists

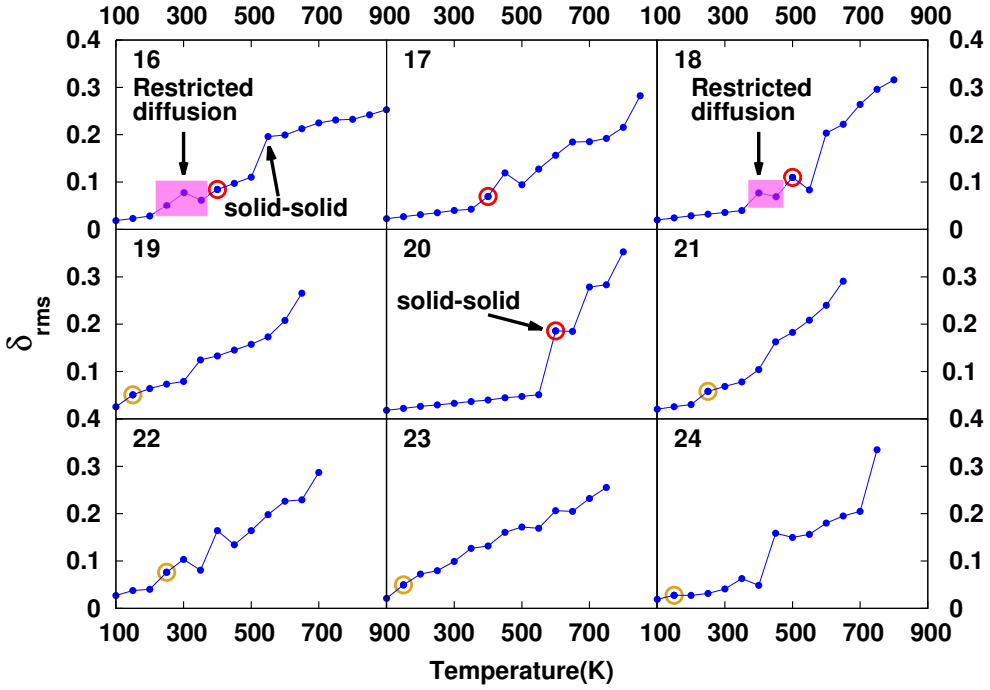

Figure 6.5: *Variation in δ_{rms} of Pb clusters as a function of their temperature. Magenta rectangles (sizes 16 and 18) highlight the temperature ranges in which "restricted diffusion" occurs. Solid-solid transition in Pb_{16} and Pb_{20} are marked with an arrow. Red circles, indicate "high" isomerisation temperatures, whereas golden circles indicate the "low" isomerisation temperatures.*

over an extended range of temperatures. Other clusters either do not exhibit any pronounced solid state, like Pb_{19}, Pb_{23}, and Pb_{24}, or have a very brief one, like Pb_{16}, Pb_{21}, and Pb_{22}. A one-to-one correspondence of $\delta_{rms}$of Pb clusters with the schematic behavior of δ_{rms} ends here because the response of all of these clusters with temperature increases is entirely different thereafter. The thermodynamic behavior of these clusters can be said to follow the general trend:

$$\begin{aligned} &\text{GS geometry/solid state} \rightarrow \text{Marginally modified GS} \\ &\qquad (\text{2–4 atoms displace}) \rightarrow \text{Major rearrangement of atoms} \\ &\qquad\qquad (\sim 50\% \text{ or more atoms displace}) \rightarrow \text{Fragmentation} \end{aligned} \tag{6.1}$$

Each of these transitions ($\rightarrow$) is signified by a jump in δ_{rms}. Except for Pb_{20}, all clusters follow this trend faithfully. The first process observed in the finite temperature behaviour, "marginally modified GS", refers to a class of isomers with a structural motif similar to that of GS, but with minor rearrangements like hopping of a cap atom or rearrangements of atoms due to processes like restricted diffusion (discussed later in the text). In contrast to this, in "major rearrangements" the cluster is "confined" into one kind of structural motif, where although most atoms diffuse, the diffusion is limited to specific parts of cluster, such as its surface, while the cluster preserves its specific structural identity. The solid-solid transition observed in Pb_{16} and Pb_{20} (discussed later in the text), is considered as a "major rearrangements" of atoms since after the transition, the clusters "trapped" in a structure with specific structural arrangements, like the core-shell motif. However, major rearrangements do not imply that the cluster is in liquid-like state where "all" atoms diffuse throughout the cluster, and its shape or structural identity is lost altogether. All these observations are further clarified by MD trajectory analysis and are discussed in the following sections.

The most interesting observations of these clusters as follows: (1) These clusters can be divided into two classes on the basis of the temperature at which their first distinct isomer (T_{iso}) occurs. Sizes 16, 17, 18, and 20 belong to the class of clusters with "high" isomerisation temperature. Distinct isomers of these clusters appear at relatively higher temperatures and are indicated by red circles in Fig. 6.5, whereas the first isomers for remaining sizes occur at much lower temperatures, indicated by golden circles in the figure. (2) Within the "high isomerisation temperature" class, there occurs two interesting cases of "restricted diffusion", for size 16 and 18. The temperature range over which restricted diffusion occurs is highlighted by a magenta rectangle in Fig. 6.5. (3) Solid-solid transition is observed for sizes 16 and 20 and is labeled accordingly in Fig. 6.5. (4) δ_{rms} of Pb_{23} is more or less featureless. In what follows, detailed description of all these observations along with their explanations based on the GS properties will be given . Also, we will elucidate that, for such small clusters, it is not "always" possible to define the liquid-like state of the cluster unambiguously.

High vs Low isomerisation Temperatures

A detailed bondlength analysis of these clusters is carried out to understand the first observation of low versus high isomerisation temperatures. The difference between the two classes begins to emerge when one plots the shortest few bondlengths within the cutoff of 3.8 Å, of the clusters in these groups. Short bonds present in Pb_{20}, which represents the "high isomerisation temperature" class, and Pb_{23} representing the "low isomerisation temperature" class are shown in Fig. 6.6(a). It is evident from the plot that, bonds of Pb_{23} have a continuous distribution of bond lengths, whereas shortest bonds of Pb_{20} occur in discrete groups. This indicates that atoms in Pb_{20} are more organized into "groups" of many atoms experiencing identical environments in terms of bonding

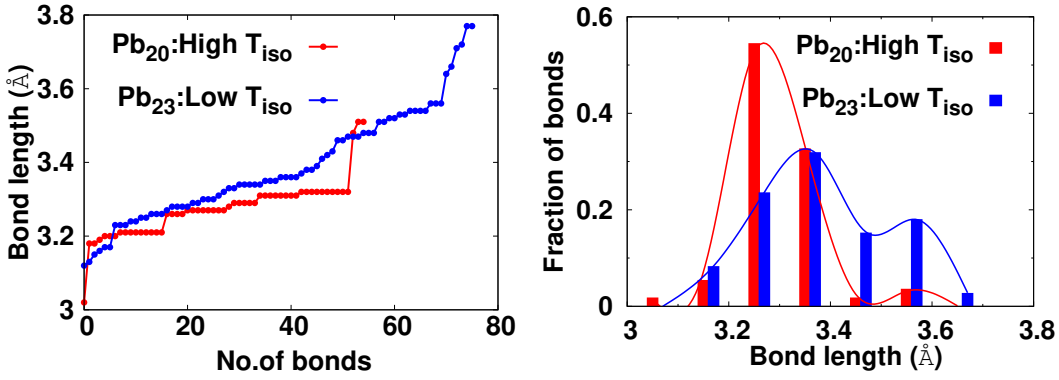

(a) (b)

Figure 6.6: *(a) Bond lengths within a cutoff distance of 3.8 Å for sizes Pb_{20} and Pb_{23} , representing the classes of high and low isomerisation temperature clusters, respectively. (b) Frequency distribution of data from (a), indicating the majority (nearly 55%) of atoms in Pb_{20} possess shorter bond length of 3.25 Å, in comparison to Pb_{23} that has more evenly spread out distribution of its shortest bonds.*

with their neighboring atoms. On the contrary, the shortest bonds of Pb_{23}, exhibit a lack of such grouping with its shortest bonds forming a more or less continuous distribution of bondlengths. The same graph also shows that nearly all short bonds of Pb_{20} are shorter in comparison with the corresponding short bonds of Pb_{23}. Plotting a frequency distribution of these short bonds clears up the picture. Fig. 6.6(b) shows the frequency distribution of bondlengths plotted in Fig. 6.6(a). The plot indicates that maxima of these two distributions lie at 3.25 Å and 3.35 Å for Pb_{20} and Pb_{23} respectively. Also, nearly 55% of the short bonds of Pb_{20} are 3.25 Å in length, whereas about 30% of total short bonds are 3.35 Å in length for Pb_{23}. This makes it clear that the majority of short bonds of Pb_{20} are identical in length (3.25 Å) and shorter than those of Pb_{23}, whereas bond lengths of Pb_{23} are more evenly spread over the first nearest neighbor (1NN) range of 3.8 Å. Thus, the majority of atoms at smaller separation with identical surroundings impart Pb_{20} greater stability than Pb_{23}. This makes Pb_{20} isomerise a at higher temperature than that of Pb_{23}. Similarly, the other clusters present in these two classes also possess the similar kind of bondlength distribution.

Restricted Diffusion

The second interesting observation marked on the δ_{rms} plot is "restricted diffusion", observed in Pb_{16} and Pb_{18}. The temperatures over which this phenomenon occurs are indicated by magenta boxes in Fig. 6.5. In this phenomenon, atoms in one of the two 5-atom rings of Pb_{16} and the 3-atom ring in Pb_{18} swap positions within the ring during the MD. The movement of atoms during this process is pictured in Fig. 6.7. For clarity, atoms in the respective rings of Pb_{16} (a and b in Fig. 6.7) and Pb_{18} (c and d in Fig. 6.7) are highlighted using different colors. Meanwhile, the rest of the atoms in their respective clusters either oscillate about their mean positions or displace

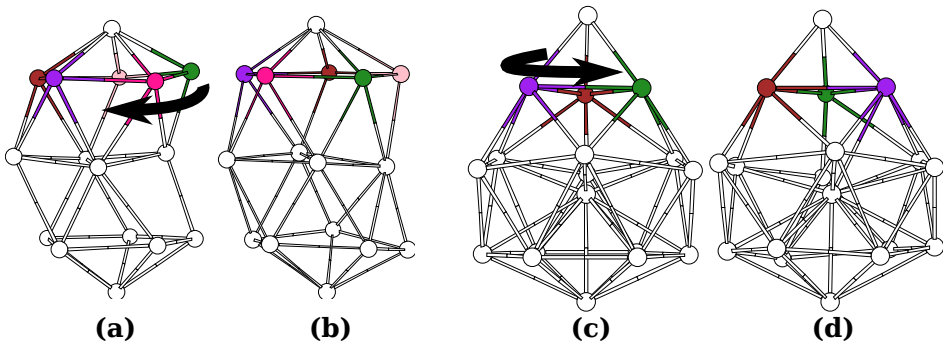

Figure 6.7: *Figures highlighting the motion of atoms during "restricted diffusion" of Pb_{16} (a and b) and Pb_{18} (c and d). The atoms in the 5-atom and 3-atom rings of Pb_{16} and Pb_{18}, which swap their positions, are shown as colored spheres.*

only marginally. In both cases, their geometries are left unaltered once this transition takes place, because swapping of atoms within the ring does not alter the shape of the respective clusters. However, the process of swapping of atoms does give rise to added fluctuations in bondlengths of clusters, which are reflected as the first jump in δ_{rms}, within the magenta boxes of Fig. 6.5.

The reason for occurrence of restricted diffusion is just as interesting as the phenomenon itself. Restricted diffusion is an attempt by ring atoms to increase their coordination dynamically. This can be proved by investigating the coordination of atoms that take part in the process, as a function of simulation time. Fig. 6.8 plots the coordination number of two ring atoms of Pb_{16} during the process of restricted diffusion at 250 K. It is clear that their coordinations swap values from the initial 4 and 5 to 5 and 4 after about 70 ps of MD. Thus, at any instance during the transition, two of the atoms from the 5-membered ring changes their coordination simultaneously. A similar process occurs for ring atoms of Pb_{18} also. Two of the three atoms in the 3-atom ring of Pb_{18} start out with coordination 7, whereas the third one with coordination 6. The graph for the two sets of atoms shows a similar kind of swapping of coordination number, which could be seen if the coordination of atoms present in the 3-atom ring of Pb_{18} is plotted as a function of simulation time. It is noteworthy that swapping of atoms occurs in atoms of both the rings of Pb_{16}, although not simultaneously. The process occurs multiple times during the course of MD, with about a 150 ps interval, and its frequency of occurrence goes on increasing with temperature. It was observed that the motion of atoms in "restricted diffusion" cannot be explained by a single normal mode of vibration, instead requiring 3-4 different normal modes to mimic it. One of the normal modes was found to be the torsion of five-atom ring, but the frequency corresponding to this mode was only second highest among all normal modes, and not a lower one, suggesting that the bonds of ring atoms are stiff modes, and not soft ones. The activation barrier involved in the process of restricted diffusion of Pb_{16} was also estimated using nudged elastic band method. The energy profile of the NEB is given in Fig. 6.9. Geometric configurations corresponding to the intermediate images are

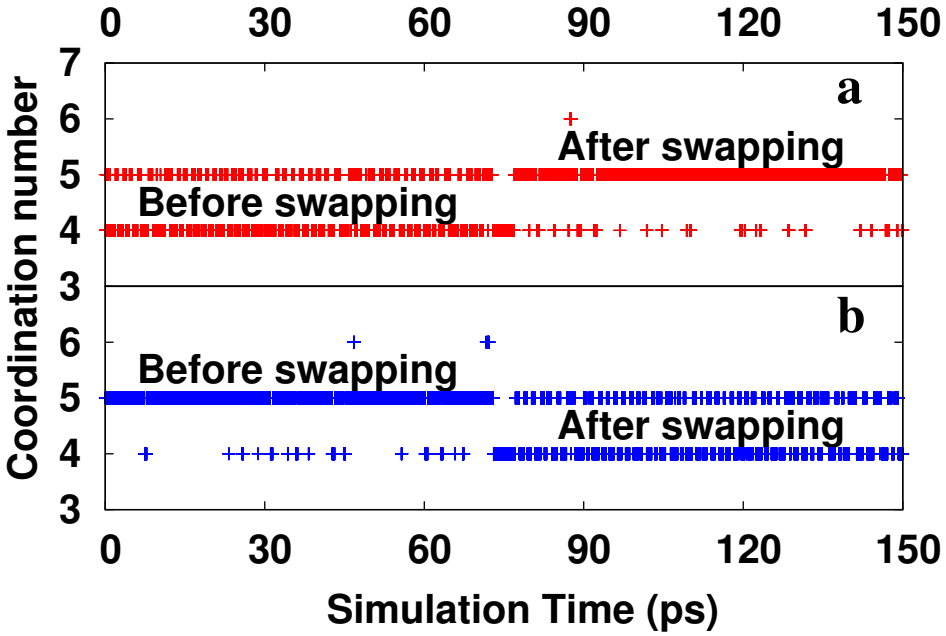

Figure 6.8: *Coordination of two different atoms in the five-atom ring of Pb_{16} over an MD trajectory at 250 K, where restricted diffusion occurs. (a) Coordination of the ring-atom that has coordination 4 at the beginning, which later becomes 5 as the restricted diffusion proceeds. (b) Coordination of ring-atom that has coordination 5 initially, which becomes 4 during restrictive diffusion at the same instant at which that other atom's, (a)'s, coordination increases from 4 to 5.*

displayed overlaid on the graph, where the ring atoms are highlighted in different colors for visual aid. The activation barrier for rotation of ring atoms was found to be about 0.16 eV. On a final note, although restricted diffusion may seem to be specific to Pb_{16} and Pb_{18}, the reason it happens indicates otherwise. Because restricted diffusion is a dynamic attempt of low coordinated atoms to increase their coordination, it is expected to occur in clusters with slight imbalance of coordination in geometrically equivalent atoms. Moreover, it is more likely to take place in small clusters.

Solid-Solid Transition

The third observation noted in the δ_{rms} plots is solid-solid transition, observed only for Pb_{16} and Pb_{20}. During this transition the hollow GS structures of these clusters transform into structures with internal atoms. The distribution of atoms about the center of mass of cluster aids to differentiate this solid-solid transition from liquification. The distribution computed over 240 ps at four different temperatures for Pb_{16} and contrasted it with that of Pb_{17}, in which no such transition occurs, is represented in Fig. 6.10. Fig. 6.10(a) shows the distribution for Pb_{16} at temperatures 100, 500, 550 (solid-solid transition), and 850 K (near fragmentation). At 100 K, the distribution of atoms resembles that of the Pb_{16} GS, with temperature specific broadening that accounts for oscillation of atoms about their mean positions. The corresponding geometry is a hollow structure without

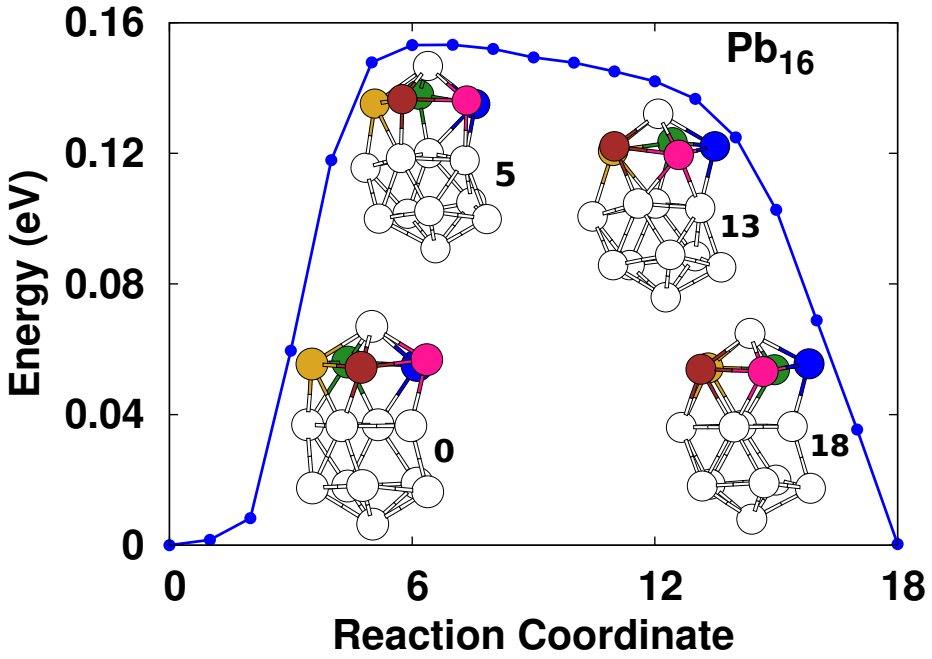

Figure 6.9: *NEB energy profile of the restrictive diffusion of Pb_{16}. Intermediate image geometries, and their corresponding image index, are shown overlaid on the energy profile for representative changes in the structure. Rotation of atoms throughout the ring becomes clear by these 4 configurations, in which the rotating atoms are highlighted in various colors for the visual aid.*

any internal atom, shown alongside the graph of 100 K in the figure. The width of the peaks goes on increasing until 500 K, which is consistent with the appearance of GS type isomers. At 550 K, however, there appears a peak at the COM of the cluster. This is a sign that the geometric structure at 550 K (and thereafter) contains an atom at the COM of cluster, which was absent until 500 K. The transformed geometry with an internal atom is shown alongside the graph of 550 K in the figure and the atom at the COM is colored magenta to aid the eye. Comparing the distribution function at all temperatures indicates that a single broad peak which is the signature of liquid-like state is clearly absent at all these temperatures up to fragmentation of the cluster. Thus, it becomes clear that the observed transition is a solid-solid transition, where the structure switches from the hollow GS motif, to the one with an internal atom, without becoming liquid at any temperatures, up to its fragmentation at 900 K. The new structural motif (with internal atom) remains the same up to 850 K. Isomerisation analysis showed that all isomers after the transition, have at least one internal atom, whereas all isomers before solid-solid transition have no internal atom. The diffusion of surface atoms leads to an increase in δ_{rms} values after this transition, and not the liquification. The same can be said about cluster Pb_{20}, whose geometries correspond to before and after this solid-solid transition are shown in Fig. 6.11. In case of Pb_{20}, the first process that occurs after solid-like state is "major rearrangements of atoms", which results in a solid-solid transition. Moreover, this transition causes a sudden jump in the value of δ_{rms} of Pb_{20} at a temperature of 600 K as seen

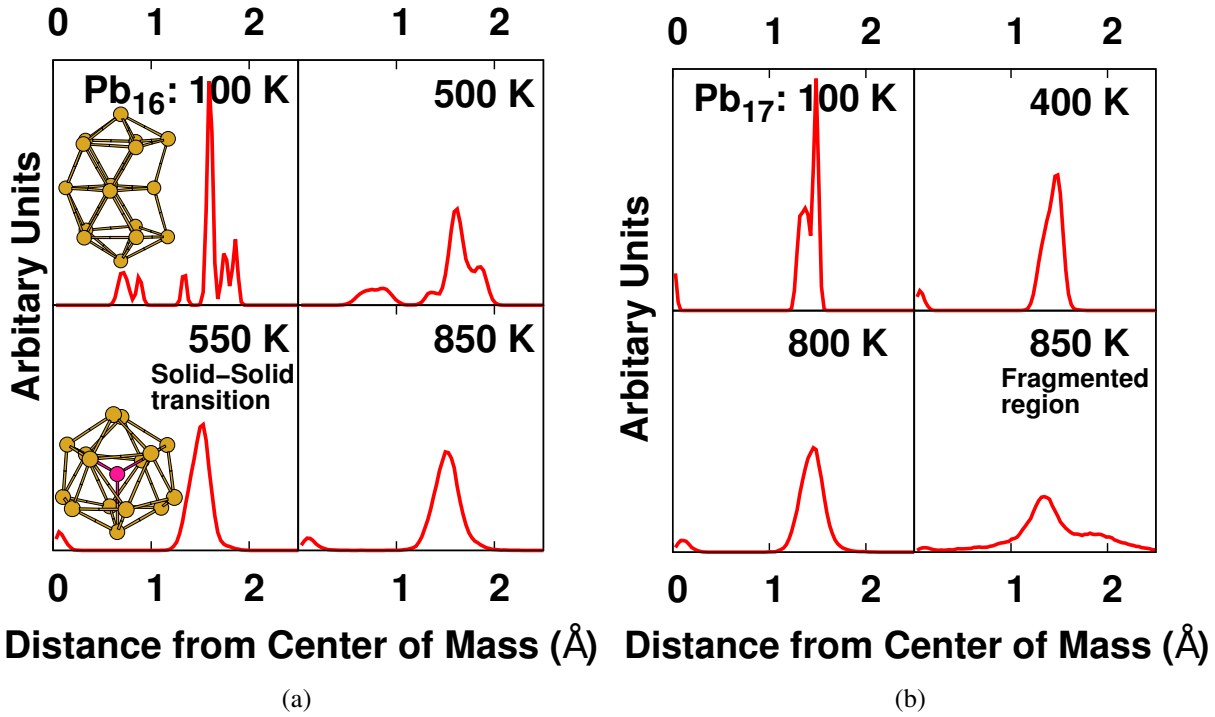

(a) (b)

Figure 6.10: *Graph of probability of finding an atom at a given distance from the center of mass, for Pb_{16} and Pb_{17}. Temperatures for Pb_{16} are chosen, where major rearrangements of atoms occur. GS motif is preserved at 100 K, where actual geometry is shown alongside its graph. At 550 K, only a solid-solid structural transition is seen, and the transformed geometry is shown alongside the 550 K graph. The cluster does not melt at any temperature above 550 K, until it fragments at 900 K. Data are plotted for 240 ps of MD. Similar graphs for Pb_{17} show no such solid-solid transition at any temperature up to its fragmentation.*

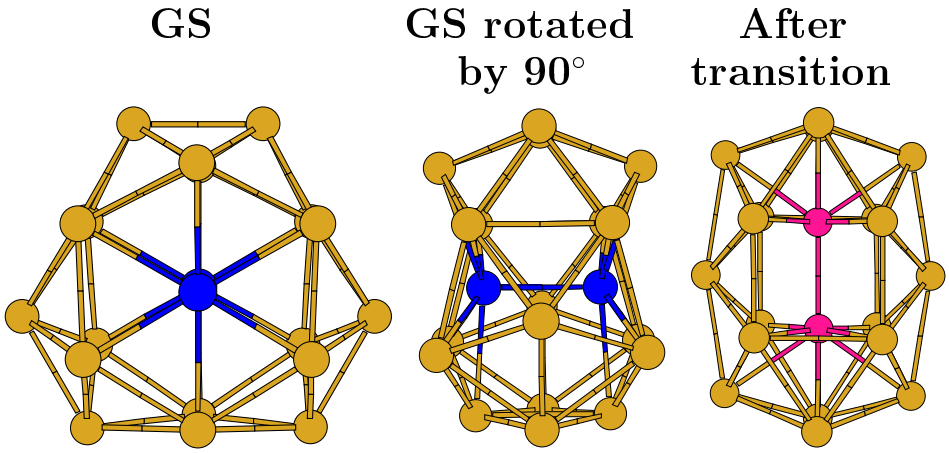

Figure 6.11: *Solid-solid transition in Pb_{20}. Pb_{20} GS, which does not have any enclosed atoms initially, transits into a new motif with two internal atoms, via the solid-solid transition. Blue spheres represent atoms in the GS that are connected by the shortest bond but are not entirely internal to the structure. Magenta spheres, on the contrary, represent the atoms that are completely enclosed inside the transformed structure. Golden spheres represent the atoms on the surface of the structures.*

from Fig. 6.5. After the solid-solid transition the cluster undergoes "marginal modification of the structure" followed by "major rearrangements of atoms" and finally fragmentation. Thus, in case of Pb_{20} the observed trend as mentioned in the Eq. 6.1 is applicable only after the structural transition, while the other systems follow the trend.

A contrasting case of Pb_{17} is shown in Fig. 6.10(b) in which no such transition occurs at any temperature until its fragmentation. The motif of Pb_{17} structure remains the same (one with an internal atom) throughout the range of temperatures from 100 K to its fragmentation at 850 K. The (GS) structural identity collapses only at its fragmentation temperature and is true for all other clusters in this size range. This concludes that in case of this Pb clusters, a well-defined liquid-like state (loosing GS structural identity) is not observed, or that the temperature window over which the state was observed is too narrow to differentiate it from fragmentation. Moreover, the solid-solid transition corresponds to the transition of structural motif of Pb_{16} and Pb_{20} from one without any internal atom, to a structure containing internal atoms. Because this solid-solid transition is an artifact of a specific GS structural motif, it can therefore occurs in clusters that have the GS structure as cages. It is also note that once this transition occurs, the cluster visits the previous motif only once, just before its fragmentation.

The isomer Analysis

The fourth and the last observation in the δ_{rms} plot is the almost featureless increase in δ_{rms} values of Pb_{23}. Although an exact reason behind this feature is not justified, an observation from the DE plots (shown in Fig. 6.12) can be used to explain it. In Fig. 6.12, the distance matrix in the Kohn-Sham eigenspace as defined in Refs [144, 145] is plotted against the energy of isomers with respect to the GS energy, for all sizes. Only the isomers that occur before fragmentation are considered for this purpose. The plot infers that, Pb_{23} shows isomers that are located toward the bottom left corner of the graph, near the origin, whereas other sizes show a lack of it. Isomers of all the sizes show a continuous distribution of energies (x-direction in the DE plots) but exhibit a jump in eigenvalues (y-direction in the DE plots) of their first isomer. Isomers of Pb_{23} exhibit continuity in both directions. Because eigenvalues reflect changes in structure, we believe that there exists a continuity of isomer structures with respect to isomer energies in Pb_{23} that is not present in other sizes. This continuity of Pb_{23} in eigenvalues, as well as total energies, implies that the isomers of Pb_{23} have a more continuous range of structure as well as energy that is not separated from its GS. This avails Pb_{23} a seamless transitions from its GS structure to its isomers, making its δ_{rms} featureless.

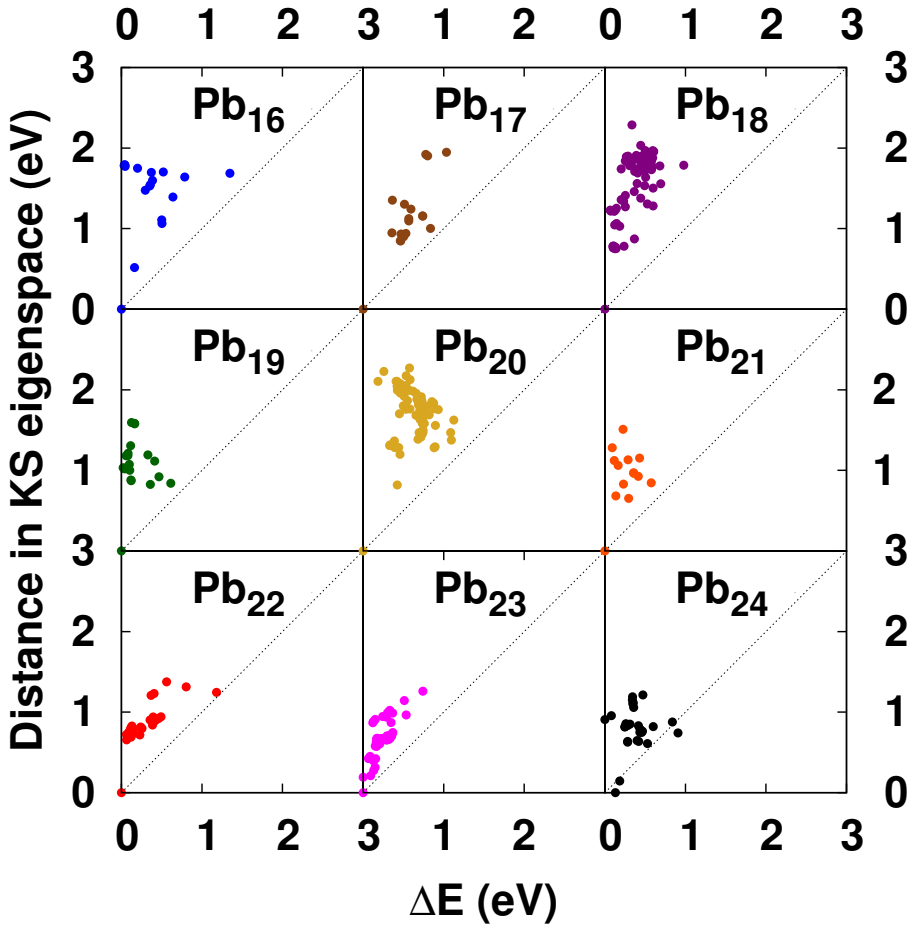

Figure 6.12: *DE plots for Pb_n (n = 16–24). The distance in Kohn-Sham (KS) eigenspace is plotted against the energy of isomers (energy of GS = 0) for respective sizes. All sizes exhibit continuity along x-axis, and a jump from GS to the first isomer along the y-axis, except Pb_{23}. Pb_{23} shows continuity in both directions, in continuum with the GS.*

6.4 Summary and conclusions

The thermodynamics of small Pb clusters is discussed in detail and compared with the general features of thermodynamics of small clusters. Putative global minima of Pb clusters between size 16 and 24 is researched in this study, with a new GS structure found for Pb_{20}. The revised GS structures are used to carry out the thermodynamics of these clusters. All GS structures of these Pb clusters are compact cages with internal atoms, except the GS of Pb_{16} and Pb_{20}. All Pb clusters studied here undergo fragmentation at elevated temperatures and are stable (with an exception of Pb_{21}) above $T_{m[bulk]}$. Thermodynamics of these small Pb clusters usually follows the path from solid state GS structure, to its isomerisation, followed by major rearrangements of atoms, and then fragmentation. Solid-solid transition occurs during the thermodynamics of Pb_{16} and Pb_{20}. The origin of this transition is in their GS structures with all atoms on the surface and it is expected

to occur for other clusters with similar GS structural motifs. Restricted diffusion is observed in clusters with equivalent atoms having a slight imbalance in their coordination, which could be a generic feature of small clusters with unequally coordinated but geometrically equivalent atoms. In this process, a specific subset of atoms swap places during constant temperature MD, preserving the overall shape of clusters. DE plots are used to explain the continuous thermodynamic transition of Pb_{23}. Restricted diffusion and solid-solid transition can be observed in other clusters as well, depending upon the appropriateness of the cluster. However, the fragmentation observed in case of Pb clusters is a characteristic of clusters of group IV elements. The inability of δ_{rms} to characterise the "melting" in finite-size systems is discussed here, which is the prominent tool to characterise the same in bulk systems. The absence of a liquid-like state is also shown through this extensive simulation studies.

CHAPTER 7

Symmetric cages at finite temperatures

7.1 Motivation and definition of the problem

The discovery of C_{60}[163] inspired many investigations, both experimental and theoretical, to find out more such stable hollow cage like structures. These studies came up with many systems of non-carbon elements, both metals and non-metals, similar to that of fullerenes.[164–176] Further, cage like structures in some compounds like B-N, have been synthesized and theoretically studied.[177, 178] These cage-like geometries provide free space to accommodate atoms/molecule inside it, which in turn may lead to better stability while sometimes also modifying their properties.[170, 179] These features were already observed by many investigations and were found to be applicable in many fields.[176, 180, 181] This makes the investigation of hollow cages more appealing. Through the initial studies discussed in the earlier chapters, it is illustrated that the GS motif plays a crucial role and has a direct effect on the finite temperature of a system. Thus, it is interesting to stimulate cage like systems to understand the process of melting in those systems. Till date, Sn_{12}^{2-} and Pb_{12}^{2-} are the smallest hollow cage structures that are stable once experimentally synthesised.[166–168] Doping and the variations in properties with dopants were explored through different theoretical studies.[182, 183] However, temperature dependent behaviour has not been probed till now. Thus, investigations about the thermodynamic behaviour of these clusters will provide a chance to explore their response towards temperature and the influence of cage-like structure in the process of phase transition.

7.2 Computational details

The ground state geometries of these cage structures have already been published.[166–168] The published coordinates were re-optimized using VASP. The re-optimized geometries are the

same as that of the reported ones and are shown in Fig. 7.1. The interactions between the ion and valence electrons were treated using PAW pseudopotential. The exchange correlational functional used was PBE. The size of the simulation box was 24 Å. The criteria used for the energy convergence for each self-consistency iteration was 10^{-4} eV. For optimization, the convergence criteria for force on each ion was taken to be 0.005 eV/Å. The finite temperature behaviour were carried out using Nosè thermostat. Each cluster was maintained at 14 temperatures between 100 K $\leq T_{cluster} \leq$ 1200 K for a period of at least 120 ps or more. Local optimizations were performed using the geometries from the finite temperature data (unbiased and equally spaced) as the initial geometries, after which isomer analysis was performed.

7.3 Results and discussion

These cages possess a highly symmetrical, I_h hollow cage structure as their GS (Refer Fig. 7.1). These systems are stable as noted by the large HOMO-LUMO gap of 1.44 and 1.38 eV respectively, for Sn_{12}^{2-} and Pb_{12}^{2-}. Interestingly, all (25) MOs of both the clusters follow the Jellium pattern faithfully and their ordering is tabulated in the Table. 7.1. It is noted that out of the 25 MOs, the order in which the first 17 MOs appear is the same for both cages, while the rest exhibit a swap in their order. Thus, even if the cages have same GS structure, the electronic structure of

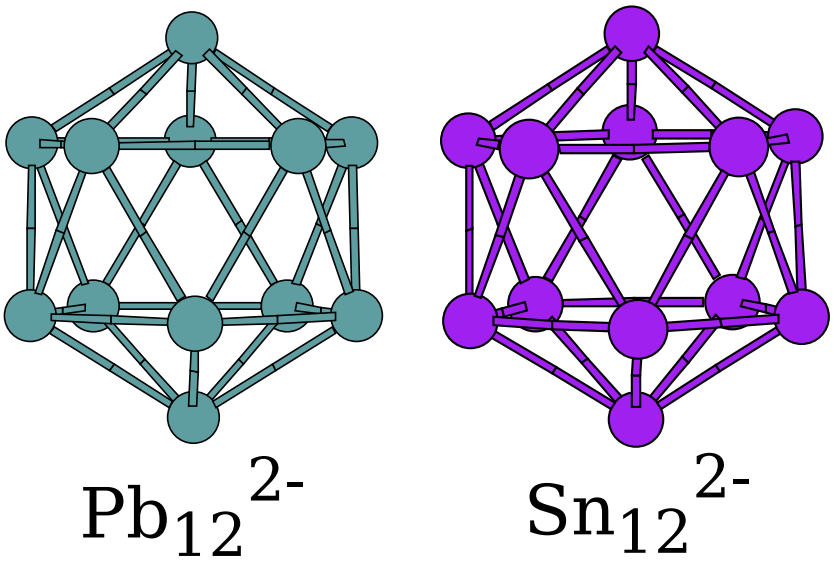

Figure 7.1: *GS structures of Pb_{12}^{2-} and Sn_{12}^{2-}.*

both clusters is slightly different. Hence, these two systems become another pair of clusters similar to that of Al_{36} and Ga_{36}. So, these cages provide one more opportunity to understand the nature of transition of two systems which have similar GS with an equal number of atoms and valence electrons, but with slightly different electronic structure. The thermodynamic

Sn_{12}^{2-}	$1S^1$	$1P^3$	$1D^5$	$1F^3$	$2S^1$	$1F^4$	$2P^3$	$1G^5$
Pb_{12}^{2-}	$1S^1$	$1P^3$	$1D^5$	$1F^3$	$2S^1$	$1F^4$	$1G^5$	$2P^3$

Table 7.1: *Comparison of the valence MOs of Sn_{12}^{2-} and Pb_{12}^{2-}. The ordering is different for Pb_{12}^{2-} and is highlighted in red.*

investigations have showed that these cages prefer fragmentation over melting. Furthermore, an interesting observation is marked in their finite temperature behaviour. It is noticed that at a particular temperature termed as transition temperature (T_r) the cage structures switch between two states. At the transition temperature these clusters swap between a cage structure and a non-cage structure. This structural transition is accompanied by a change in their HOMO-LUMO gap. Before the transition temperature, these clusters are in solid-like state, performing oscillations about their mean position. However, after the T_r the cages are at the verge of fragmentation. Also, the extensive simulations performed for a range of temperatures confirmed that, this type of transition is not seen at any temperature before and after the T_r. The temperature at which this transition occurs is system dependent. For Sn_{12}^{2-} this transition occurs at 950 K, but for Pb_{12}^{2-} the same occurs at a temperature of 1000 K. The cage to non-cage to cage transition for these cages is shown in Fig. 7.2, with region of this transition is labelled to aid the eye. The potential energy distribution is plotted with red lines. The observed fluctuations in the HOMO-LUMO gap is also represented in the same figure with blue lines. The plot clearly indicates a distinct transition between two states, both in energy and HOMO-LUMO gap. Further, the isomer analysis indicated that, the non-cage structure appears at a higher ΔE (energy difference w.r.t GS) for both the clusters, which infers the higher stability of this hollow cage structures. For instance, it is noted that the first isomer occurs at a ΔE of 0.7 and 1.3 eV for Sn_{12}^{2-} and Pb_{12}^{2-} respectively. Moreover, the isomer analysis showed that the distinct isomers that appear in the fragmented region are mainly composed of stable units that contain 7 or 9 atoms. In conclusion, these simulations indicated that these stable cage structures exhibit similar thermodynamics behaviour. The different processes involved as a function of temperature are similar for both clusters. These systems display a distinct structural (cage-to-non-cage) phase transition just after their respective solid-like state regions. A fragmentation region follows this transition region, where a majority of the structures are mainly composed of similar units (7 or 9 or 10) for both systems. For these small systems, the entire thermodynamics is mainly dependent on the highly symmetrical hollow cage structure.

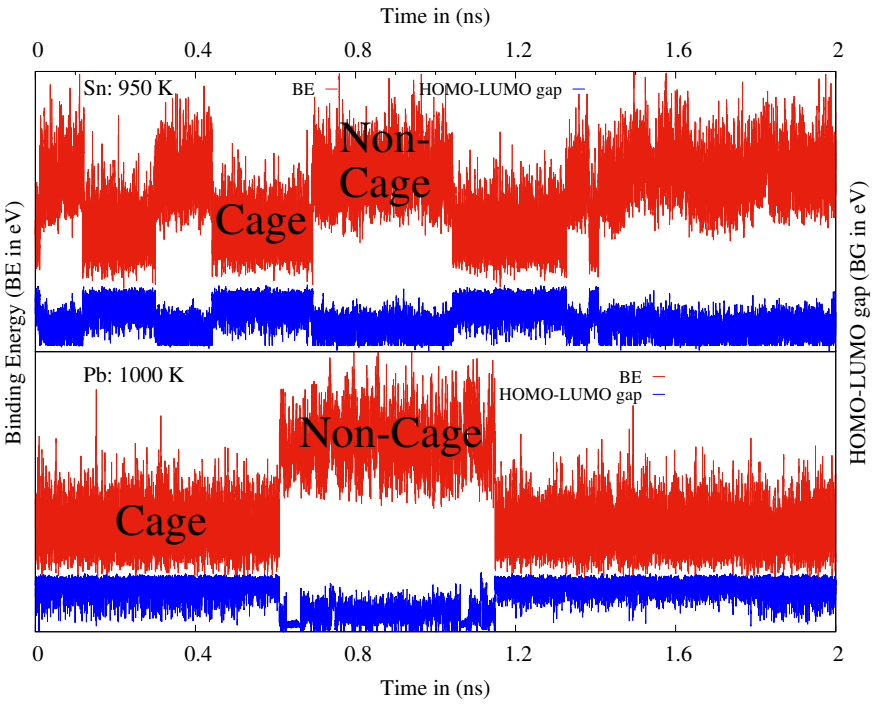

Figure 7.2: *Potential energy distribution (BE, red graph) in eV, for Sn_{12}^{2-} at 950 K, and Pb_{12}^{2-} at 1000 K, showing the cage-noncage-cage transition during their constant temperature dynamics. The accompanied variation in the HOMO-LUMO gap also plotted in the same graph (blue lines).*

7.4 Summary and conclusions

A distinct phase transition, which is accompanied by a substantial change in the HOMO-LUMO gap (electronic property) is observed in 12 atom symmetrical cages. Although, the feature is not reasoned out, this may be considered as the smallest system which exhibits a distinct phase transition as a function of temperature. This opens up a chance to explore the thermodynamics of other stable hollow cage structures, which may lead to the discovery of a few more interesting characteristics of these finite-size systems.

CHAPTER 8

Summary and future scope of the work

The interesting features observed in solid-like to liquid-like transition of finite size systems are addressed through the present investigation. To an extent these simulations were able to explain the experimental observations in the process of melting. The correlation between the ground state motif of small clusters and the size dependent variations in phase transition is demonstrated through these studies. The different melting behaviour of clusters are also explained based on the ground state structure. Bondlength and isomer analysis performed on these clusters spelled out the different characteristics of phase transition in these systems. Further, the central role of ground state motif in the process of melting is demonstrated by performing finite temperature studies on a unique pair of systems which possess similar ground state structural motif. Thus, this analysis provides a better understanding of the process of melting in small clusters.

In the context of clusters, the concept of 'melting' is different. One needs to modify the term in comparison with that of bulk. In order to verify the melting process, one should consider parameters like, heat capacity curve and δ_{rms}, similar to that of bulk. These tools are found to be useful, providing a clear interpretation in case of macroscopic materials. Though, through our extensive finite temperature investigations it is spelled out that one could not directly apply these tools to predict the melting behaviour in clusters. These studies illustrated the drawback of the thermodynamic parameter like δ_{rms} while explaining the phase transition in case of finite size systems.

A few interesting phenomena observed through these simulations signify the outlook of the field. For instance, the studies illustrated that a small system with 12 atom could exhibit distinct structural transitions. The property change which accompanies this transition could be useful in the field of phase change materials. This kind of phase change materials in nanoregime is observed through experimental studies also, as a function of temperature.[126] This suggest the possibility of studying the dynamical processes in small clusters with temperature. Further, an

enhancement in cluster reactivity when the system in the liquid-like state is demonstrated through a few experimental studies.[184–188] Investigations demonstrated that clusters of aluminium in liquid-like state, with sizes 44 and 100, were able to activate small molecules like N_2 and CO_2. The studies also showed that the activation energy for the reaction between Al_{100}^{+} and N_2 dropped by a value of 1 eV when the cluster is in its liquid-like state.[184] This opens up a new way to study liquid-like states in clusters and their future applications in the field of catalysis.

List of publications

- "Correlation between the variation in observed melting temperatures and structural motifs of the global minima of gallium clusters: An ab initio study", A. Susan, A. Kibey, V. Kaware, and K. Joshi; J. Chem. Phys. 138, 014303 (2013).

- "Rationalizing the role of structural motif and underlying electronic structure in the finite temperature behavior of atomic clusters", A. Susan and K. Joshi; J. Chem. Phys. 140, 154307 (2014).

- "Multifaceted Thermodynamics of Pb_n (n = 16–24) Clusters: A Case Study", A. Susan, V. Kaware, and K. Joshi; J. Phys. Chem. C 119, 23698 (2015).

- "Ground State Motif: Master Key to Understand Process of Melting in Clusters", A. Susan, V. Kaware, and K. Joshi; Manuscript under preparation.

References

[1] Kondow, T.; Mafuné, F. *Progress in experimental and theoretical studies of clusters*; World Scientific, 2003; Vol. 13.

[2] Jena, P.; Castleman Jr, A. W. *Nanoclusters: A bridge across disciplines*; Elsevier, 2010.

[3] Alonso, J. A. *Structure and properties of atomic nanoclusters*; World Scientific, 2005.

[4] Astruc, D. *Nanoparticles and catalysis*; Wiley Online Library, 2008; Vol. 1.

[5] Haruta, M.; Kobayashi, T.; Sano, H.; Yamada, N. *Chem. Lett.* **1987**, 405–408.

[6] Bond, G.; Sermon, P. *Gold Bulletin* **1973**, *6*, 102–105.

[7] Haruta, M. *Catal. Today* **1997**, *36*, 153–166.

[8] Cox, A.; Louderback, J.; Bloomfield, L. *Physical review letters* **1993**, *71*, 923.

[9] Cox, A.; Louderback, J.; Apsel, S.; Bloomfield, L. *Phys. Rev. B* **1994**, *49*, 12295–12298.

[10] Kumar, V.; Kawazoe, Y. *Eur. Phys. J. D* **2003**, *24*, 81–84.

[11] Louderback, J.; Cox, A.; Lising, L.; Douglass, D.; Bloomfield, L. *Zeitschrift für Physik D Atoms, Molecules and Clusters* **1993**, *26*, 301–303.

[12] Bucher, J. P.; Douglass, D. C.; Bloomfield, L. A. *Phys. Rev. Lett.* **1991**, *66*, 3052–3055.

[13] Billas, I. M.; Chatelain, A.; de Heer, W. A. *Science* **1994**, *265*, 1682–1684.

[14] Schmidt, M.; Haberland, H. *C. R. Phys.* **2002**, *3*, 327 – 340.

[15] Aguado, A.; Jarrold, M. F. *Annu. Rev. Phys. Chem.* **2011**, *62*, 151–172.

[16] Pawlow, P. *Z. Phys. Chem* **1909**, *65*, 1–35.

[17] Pawlow, P. *Z. Phys. Chem* **1909**, *65*, 545–548.

[18] Takagi, M. *Journal of the Physical Society of Japan* **1954**, *9*, 359–363.

[19] Peppiatt, S. J. *Proc. R. Soc. London, Ser. A* **1975**, *345*, 401–412.

[20] Buffat, P.; Borel, J.-P. *Phys. Rev. A* **1976**, *13*, 2287–2298.

[21] Couchman, P. R.; Jesser, W. A. *Nature* **1977**, *269*, 481–483.

[22] Lai, S.; Guo, J.; Petrova, V.; Ramanath, G.; Allen, L. *Phys. Rev. Lett.* **1996**, *77*, 99–102.

[23] Breaux, G. A.; Benirschke, R. C.; Sugai, T.; Kinnear, B. S.; Jarrold, M. F. *Phys. Rev. Lett.* **2003**, *91*, 215508–215511.

[24] Breaux, G. A.; Neal, C. M.; Cao, B.; Jarrold, M. F. *Phys. Rev. B* **2005**, *71*, 073410–073413.

[25] Martin, T. P.; Näher, U.; Schaber, H.; Zimmermann, U. *J. Chem. Phys.* **1994**, *100*, 2322–2324.

[26] Shvartsburg, A. A.; Jarrold, M. F. *Phys. Rev. Lett.* **2000**, *85*, 2530–2532.

[27] Shvartsburg, A. A.; Jarrold, M. F. *Phys. Rev. A* **1999**, *60*, 1235–1239.

[28] Schmidt, M.; Kusche, R.; Kronmüller, W.; von Issendorff, B.; Haberland, H. *Phys. Rev. Lett.* **1997**, *79*, 99–102.

[29] Chirot, F.; Feiden, P.; Zamith, S.; Labastie, P.; L'Hermite, J.-M. *J. Chem. Phys.* **2008**, *129*, 164514–1–164514–9.

[30] Neal, C. M.; Starace, A. K.; Jarrold, M. F. *J. Am. Soc. Mass Spect.* **2007**, *18*, 74 – 81.

[31] Schmidt, M.; Kusche, R.; von Issendorff, B.; Haberland, H. *Nature* **1998**, *393*, 238–240.

[32] Kusche, R.; Hippler, T.; Schmidt, M.; Von Issendorff, B.; Haberland, H. *Eur. Phys. J. D* **1999**, *9*, 1–4.

[33] Neal, C. M.; Starace, A. K.; Jarrold, M. F. *Phys. Rev. B* **2007**, *76*, 054113 – 054122.

[34] Breaux, G. A.; Neal, C. M.; Cao, B.; Jarrold, M. F. *Phys. Rev. Lett.* **2005**, *94*, 173401–173404.

[35] Starace, A. K.; Cao, B.; Judd, O. H.; Bhattacharyya, I.; Jarrold, M. F. *J. Chem. Phys.* **2010**, *132*, 034302–034310.

[36] Jarrold, M. F.; Cao, B.; Starace, A. K.; Neal, C. M.; Judd, O. H. *J. Chem. Phys.* **2008**, *129*, 014503–1–014503–10.

[37] Starace, A. K.; Neal, C. M.; Cao, B.; Jarrold, M. F.; Aguado, A.; Lopez, J. M. *J. Chem. Phys.* **2009**, *131*, 044307–044317.

[38] Breaux, G. A.; Hillman, D. A.; Neal, C. M.; Benirschke, R. C.; Jarrold, M. F. *J. Am. Chem. Soc.* **2004**, *126*, 8628–8629.

[39] Pyfer, K. L.; Kafader, J. O.; Yalamanchali, A.; Jarrold, M. F. *J. Phys. Chem. A* **2014**, *118*, 4900–4906.

[40] Cotterill, R.; Kristensen, W. D.; Martin, J.; Pedersen, L. B.; Jensen, K. *Comput. Phys. Commun.* **1973**, *5*, 28–31.

[41] McGinty, D. J. *J. Chem. Phys.* **1973**, *58*, 4733–4742.

[42] Lee, J. K.; Barker, J.; Abraham, F. F. *J. Chem. Phys.* **1973**, *58*, 3166–3180.

[43] Briant, C.; Burton, J. *Nature* **1973**, *243*, 100–102.

[44] Kristensen, W. D.; Jensen, E.; Cotterill, R. M. *J. Chem. Phys.* **1974**, *60*, 4161–4169.

[45] Briant, C.; Burton, J. *J. Chem. Phys.* **1975**, *63*, 2045–2058.

[46] Kaelberer, J.; Etters, R. *J. Chem. Phys.* **1977**, *66*, 3233–3239.

[47] Etters, R.; Kaelberer, J. *J. Chem. Phys.* **1977**, *66*, 5112–5116.

[48] Freeman, D. L.; Doll, J. D. *Annu. Rev. Phys. Chem.* **1996**, *47*, 43–80.

[49] Natanson, G.; Amar, F.; Berry, R. S. *J. Chem. Phys.* **1983**, *78*, 399–408.

[50] Berry, R. S.; Jellinek, J.; Natanson, G. *Phys. Rev. A* **1984**, *30*, 919–931.

[51] Berry, R. S.; Jellinek, J.; Natanson, G. *Chem. Phys. Lett.* **1984**, *107*, 227–230.

[52] Davis, H. L.; Jellinek, J.; Berry, R. S. *J. Chem. Phys.* **1987**, *86*, 6456–6464.

[53] Berry, R. S. *J. Chem. Soc., Faraday Trans.* **1990**, *86*, 2343–2349.

[54] Cheng, H.-P.; Li, X.; Whetten, R. L.; Berry, R. S. *Phys. Rev. A* **1992**, *46*, 791–800.

[55] Cheng, H.-P.; Berry, R. S. *Phys. Rev. A* **1992**, *45*, 7969–7980.

[56] Berry, R. S. *Microscale Thermophys. Eng.* **1997**, *1*, 1–18.

[57] Berry, R.; Smirnov, B. M. *Phys. Usp.* **2005**, *48*, 345–388.

[58] Proykova, A.; Berry, R. *J. Phys. B: At., Mol. Opt. Phys.* **2006**, *39*, R167–R202.

[59] Berry, R.; Smirnov, B. *Low Temp. Phys.* **2009**, *35*, 256–264.

[60] Berry, R.; Smirnov, B. M. *Phys. Usp.* **2009**, *52*, 137–164.

[61] Rose, J. P.; Berry, R. S. *J. Chem. Phys.* **1993**, *98*, 3262–3274.

[62] Kunz, R. E.; Berry, R. S. *Phys. Rev. Lett.* **1993**, *71*, 3987–3990.

[63] Wales, D. J.; Berry, R. S. *Phys. Rev. Lett.* **1994**, *73*, 2875–2878.

[64] Kunz, R. E.; Berry, R. S. *Phys. Rev. E* **1994**, *49*, 1895–1908.

[65] Proykova, A.; Pisov, S.; Berry, R. S. *J. Chem. Phys.* **2001**, *115*, 8583–8591.

[66] Komatsuzaki, T.; Berry, R. S. *Proc. Natl. Acad. Sci.* **2001**, *98*, 7666–7671.

[67] Berry, R. S.; Smirnov, B. M. *Int. J. Mass Spectrom.* **2009**, *280*, 204–208.

[68] Berry, R. S.; Smirnov, B. M. *Entropy* **2010**, *12*, 1303–1324.

[69] Güvenç, Z. B.; Jellinek, J. *Z. Phys. D: At., Mol. Clusters* **1993**, *26*, 304–306.

[70] Calvo, F.; Spiegelmann, F. *Phys. Rev. Lett.* **1999**, *82*, 2270–2273.

[71] Bulgac, A.; Kusnezov, D. *Phys. Rev. Lett.* **1992**, *68*, 1335–1338.

[72] Bulgac, A.; Kusnezov, D. *Physical Review B* **1992**, *45*, 1988–1997.

[73] Ju, N.; Bulgac, A. *Phys. Rev. B* **1993**, *48*, 2721–2732.

[74] Calvo, F.; Spiegelmann, F. *J. Chem. Phys.* **2000**, *112*, 2888–2908.

[75] Calvo, F.; Spiegelman, F. *J. Chem. Phys.* **2004**, *120*, 9684–9689.

[76] Haberland, H.; Hippler, T.; Donges, J.; Kostko, O.; Schmidt, M.; von Issendorff, B. *Phys. Rev. Lett.* **2005**, *94*, 035701–1–035701–4.

[77] Noya, E. G.; Doye, J. P.; Wales, D. J.; Aguado, A. *Eur. Phys. J. D* **2007**, *43*, 57–60.

[78] Zamith, S.; Labastie, P.; Chirot, F.; L'Hermite, J.-M. *J. Chem. Phys.* **2010**, *133*, 154501–1–154501–5.

[79] Lloyd, L. D.; Johnston, R. L. *Chem. Phys.* **1998**, *236*, 107–121.

[80] Werner, R. *Eur. Phys. J. B* **2005**, *43*, 47–52.

[81] Noya, E. G.; Doye, J. P. K.; Calvo, F. *Phys. Rev. B* **2006**, *73*, 125407–125412.

[82] Zhang, W.; Zhang, F.; Zhu, Z. *Phys. Rev. B* **2006**, *74*, 033412–1–033412–4.

[83] Zhang, W.; Zhang, F.; Zhu, Z. *Eur. Phys. J. D* **2007**, *43*, 97–100.

[84] Cleveland, C.; Luedtke, W.; Landman, U. *Phys. Rev. B* **1999**, *60*, 5065–5077.

[85] Wilson, N.; Johnston, R. *Eur. Phys. J. D* **2000**, *12*, 161–169.

[86] Yildirim, E.; Guvenç, Z. *Modell. Simul. Mater. Sci. Eng.* **2006**, *14*, 947–961.

[87] Manninen, K.; Rytkönen, A.; Manninen, M. *Eur. Phys. J. D* **2004**, *29*, 39–47.

[88] Ballone, P.; Andreoni, W.; Car, R.; Parrinello, M. *Europhys. Lett.* **1989**, *8*, 73–78.

[89] Röthlisberger, U.; Andreoni, W. *J. Chem. Phys.* **1991**, *94*, 8129–8151.

[90] Foley, M.; Smargiassi, E.; Madden, P. *J. Phys. Cond. Matter* **1994**, *6*, 5231–5241.

[91] John, S. T.; Klug, D. D. *J. Chem. Phys.* **1994**, *101*, 473–475.

[92] Rytkönen, A.; Häkkinen, H.; Manninen, M. *Euro. Phys. J. D* **1999**, *9*, 451–454.

[93] Aguado, A.; López, J. M.; Alonso, J. A.; Stott, M. *J. Phys. Chem. B* **2001**, *105*, 2386–2392.

[94] Aguado, A.; López, J. M. *Phys. Rev. Lett.* **2005**, *94*, 233401–1–233401–4.

[95] Chacko, S.; Kanhere, D. G.; Blundell, S. A. *Phys. Rev. B* **2005**, *71*, 155407–155412.

[96] Ghazi, S. M.; Zorriasatein, S.; Kanhere, D. *J. Phys. Chem. A* **2009**, *113*, 2659–2662.

[97] Lee, M.-S.; Chacko, S.; Kanhere, D. *J. Chem. Phys.* **2005**, *123*, 164310–1–164310–7.

[98] Zorriasatein, S.; Lee, M.-S.; Kanhere, D. G. *Phys. Rev. B* **2007**, *76*, 165414–165421.

[99] Lee, M.-S.; Kanhere, D. *Phys. Rev. B* **2007**, *75*, 125427–1–125427–6.

[100] Kostko, O.; Huber, B.; Moseler, M.; von Issendorff, B. *Phys. Rev. Lett.* **2007**, *98*, 043401–1–043401–4.

[101] Aguado, A.; López, J. M.; Alonso, J. A.; Stott, M. J. *J. Chem. Phys.* **1999**, *111*, 6026–6035.

[102] Rytkönen, A.; Häkkinen, H.; Manninen, M. *Phys. Rev. Lett.* **1998**, *80*, 3940–3943.

[103] Aguado, A.; Molina, L.; López, J.; Alonso, J. *Eur. Phys. J. D* **2001**, *15*, 221–227.

[104] Aguado, A.; López, J. M. *Phys. Rev. B* **2006**, *74*, 115403–115413.

[105] Hock, C.; Bartels, C.; Straßburg, S.; Schmidt, M.; Haberland, H.; von Issendorff, B.; Aguado, A. *Phys. Rev. Lett.* **2009**, *102*, 043401–043404.

[106] Aguado, A. *J. Phys. Chem. C* **2011**, *115*, 13180–13186.

[107] Ghazi, S. M.; Lee, M.-S.; Kanhere, D. *J. Chem. Phys.* **2008**, *128*, 104701–1–104701–7.

[108] Aguado, A. *Phys. Rev. B* **2001**, *63*, 115404–1–115404–9.

[109] Lu, Z.-Y.; Wang, C.-Z.; Ho, K.-M. *Phys. Rev. B* **2000**, *61*, 2329–2334.

[110] Joshi, K.; Kanhere, D.; Blundell, S. *Phys. Rev. B* **2002**, *66*, 155329–1–155329–5.

[111] Joshi, K.; Kanhere, D. G.; Blundell, S. A. *Phys. Rev. B* **2003**, *67*, 235413–235420.

[112] Krishnamurty, S.; Joshi, K.; Kanhere, D.; Blundell, S. *Phys. Rev. B* **2006**, *73*, 045419–1–045419–11.

[113] Neal, C. M.; Starace, A. K.; Jarrold, M. F.; Joshi, K.; Krishnamurty, S.; Kanhere, D. G. *J. Phys. Chem. C* **2007**, *111*, 17788–17794.

[114] Kang, J.; Wei, S.-H.; Kim, Y.-H. *J. Am. Chem. Soc.* **2010**, *132*, 18287–18291.

[115] Starace, A. K.; Neal, C. M.; Cao, B.; Jarrold, M. F.; Aguado, A.; López, J. M. *J. Chem. Phys.* **2008**, *129*, 144702–1–144702–10.

[116] Akola, J.; Manninen, M. *Phys. Rev. B* **2001**, *63*, 193410–1–193410–4.

[117] Aguado, A.; López, J. M. *J. Phys. Chem. Lett.* **2013**, *4*, 2397–2403.

[118] Kang, J.; Kim, Y.-H. *ACS Nano* **2010**, *4*, 1092–1098.

[119] Joshi, K.; Krishnamurty, S.; Kanhere, D. G. *Phys. Rev. Lett.* **2006**, *96*, 135703–135706.

[120] Krishnamurty, S.; Joshi, K.; Zorriasatein, S.; Kanhere, D. G. *J. Chem. Phys.* **2007**, *127*, 054308–054314.

[121] Chacko, S.; Joshi, K.; Kanhere, D. G.; Blundell, S. A. *Phys. Rev. Lett.* **2004**, *92*, 135506–135509.

[122] Nunez, S.; Lopez, J. M.; Aguado, A. *Nanoscale* **2012**, *4*, 6481–6492.

[123] Steenbergen, K. G.; Gaston, N. *Nano Lett.* **2015**, *16*, 21–26.

[124] Steenbergen, K. G.; Gaston, N. *Phys. Chem. Chem. Phys.* **2013**, *15*, 15325–15332.

[125] Steenbergen, K. G.; Schebarchov, D.; Gaston, N. *J. Chem. Phys.* **2012**, *137*, 144307–144317.

[126] Soares, B. F.; Jonsson, F.; Zheludev, N. I. *Phys. Rev. Lett.* **2007**, *98*, 153905–1–153905–4.

[127] Martin, R. M. *Electronic structure: basic theory and practical methods*; Cambridge university press, 2004.

[128] Payne, M. C.; Teter, M. P.; Allan, D. C.; Arias, T.; Joannopoulos, J. *Rev. Mod. Phys.* **1992**, *64*, 1045–1097.

[129] Kohanoff, J.; Gidopoulos, N. *Handbook of molecular physics and quantum chemistry* **2003**, *2*, 532–568.

[130] Marx, D.; Hutter, J. *Modern methods and algorithms of quantum chemistry* **2000**, *1*, 301–449.

[131] Born, M.; Oppenheimer, R. *Annalen der Physik* **1927**, *389*, 457–484.

[132] Hohenberg, P.; Kohn, W. *Phys. Rev.* **1964**, *136*, B864–B871.

[133] Kohn, W.; Sham, L. J. *Phys. Rev.* **1965**, *140*, A1133–A 1138.

[134] Kresse, G.; Hafner, J. *Phys. Rev. B* **1994**, *49*, 14251–14269.

[135] Kresse, G.; Furthmüller, J. *Phys. Rev. B* **1996**, *54*, 11169–11186.

[136] Kresse, G.; Furthmüller, J. *Comput. Mater. Sci.* **1996**, *6*, 15–50.

[137] Perdew, J. P.; Burke, K.; Ernzerhof, M. *Phys. Rev. Lett.* **1996**, *77*, 3865–3868.

[138] Perdew, J. P.; Burke, K.; Ernzerhof, M. *Phys. Rev. Lett.* **1997**, *78*, 1396–1396.

[139] Blöchl, P. E. *Phys. Rev. B* **1994**, *50*, 17953–17979.

[140] Kresse, G.; Joubert, D. *Phys. Rev. B* **1999**, *59*, 1758–1775.

[141] Kanhere, D. G.; Vichare, A.; Blundell, S. A. *Reviews of Modern Quantum Chemistry*; World Scientific, 2002; Chapter 52, p 1568.

[142] Silvi, B.; Savin, A. *Nature* **1994**, *371*, 683–686.

[143] Susan, A.; Kibey, A.; Kaware, V.; Joshi, K. *J. Chem. Phys.* **2013**, *138*, 014303–1–014303–7.

[144] Sadeghi, A.; Ghasemi, S. A.; Schaefer, B.; Mohr, S.; Lill, M. A.; Goedecker, S. *J. Chem. Phys.* **2013**, *139*, 184118–1–184118–11.

[145] De, S.; Schaefer, B.; Sadeghi, A.; Sicher, M.; Kanhere, D. G.; Goedecker, S. *Phys. Rev. Lett.* **2014**, *112*, 083401–1–083401–5.

[146] Sheppard, D.; Terrell, R.; Henkelman, G. *J. Chem. Phys.* **2008**, *128*, 134106–1–134106–10.

[147] Henkelman, G.; Jónsson, H. *J. Chem. Phys.* **2000**, *113*, 9978–9985.

[148] Henkelman, G.; Uberuaga, B. P.; Jónsson, H. *J. Chem. Phys.* **2000**, *113*, 9901–9904.

[149] Ma, L.; Issendorff, B. v.; Aguado, A. *J. Chem. Phys.* **2010**, *132*, 104303–1–104303–6.

[150] See http://www-wales.ch.cam.ac.uk/CCD.html for coordinates of geometries optimized using empirical potentials.

[151] Kaware, V.; Joshi, K. *The Journal of chemical physics* **2014**, *141*, 054308–1–054308–9.

[152] Rajesh, C.; Majumder, C.; Rajan, M.; Kulshreshtha, S. *Phys. Rev. B* **2005**, *72*, 235411–1–235411–8.

[153] Li, X.-P.; Lu, W.-C.; Zang, Q.-J.; Chen, G.-J.; Wang, C.; Ho, K. *J. Phys. Chem. A* **2009**, *113*, 6217–6221.

[154] Kelting, R.; Otterstätter, R.; Weis, P.; Drebov, N.; Ahlrichs, R.; Kappes, M. M. *J. Chem. Phys.* **2011**, *134*, 024311–1–024311–11.

[155] Rajesh, C.; Majumder, C. *J. Chem. Phys.* **2007**, *126*, 244704–1–244704–8.

[156] Li, X.-P.; Lu, W.-C.; Wang, C.; Ho, K. *J. Phys. Condens. Matter* **2010**, *22*, 465501–1–465501–6.

[157] Schafer, S.; Heiles, S.; Becker, J. A.; Schafer, R. *J. Chem. Phys.* **2008**, *129*, 44304–1–044304–7.

[158] Pushpa, R.; Waghmare, U.; Narasimhan, S. *Phys. Rev. B* **2008**, *77*, 045427–1–045427–6.

[159] Wang, B.; Zhao, J.; Chen, X.; Shi, D.; Wang, G. *Phys. Rev. A* **2005**, *71*, 033201–1–033201–7.

[160] Senz, V.; Fischer, T.; Oelßner, P.; Tiggesbäumker, J.; Stanzel, J.; Bostedt, C.; Thomas, H.; Schöffler, M.; Foucar, L.; Martins, M. *Phys. Rev. Lett.* **2009**, *102*, 138303–1–138303–4.

[161] Li, H.; Ji, Y.; Wang, F.; Li, S.; Sun, Q.; Jia, Y. *Phys. Rev. B* **2011**, *83*, 075429–1–075429–9.

[162] Mühlbach, J.; Pfau, P.; Sattler, K.; Recknagel, E. *Z. Phys. B: Condens. Matter* **1982**, *47*, 233–237.

[163] Kroto, H. W.; Heath, J. R.; OḂrien, S. C.; Curl, R. F.; Smalley, R. E. *Nature* **1985**, *318*, 162–163.

[164] Zhao, J.; Ma, L.; Tian, D.; Xie, R. *J. Comput. Theor. Nanosci.* **2008**, *5*, 7–22.

[165] Chaur, M. N.; Melin, F.; Ortiz, A. L.; Echegoyen, L. *Angew. Chem. Int. Ed.* **2009**, *48*, 7514–7538.

[166] Cui, L.-F.; Huang, X.; Wang, L.-M.; Li, J.; Wang, L.-S. *J. Phys. Chem. A* **2006**, *110*, 10169–10172.

[167] Cui, L.-F.; Huang, X.; Wang, L.-M.; Zubarev, D. Y.; Boldyrev, A. I.; Li, J.; Wang, L.-S. *J. Am. Chem. Soc.* **2006**, *128*, 8390–8391.

[168] Cui, L.-F.; Wang, L.-S. *Int. Rev. Phys. Chem.* **2008**, *27*, 139–166.

[169] Zhai, H.-J.; Zhao, Y.-F.; Li, W.-L.; Chen, Q.; Bai, H.; Hu, H.-S.; Piazza, Z. A.; Tian, W.-J.; Lu, H.-G.; Wu, Y.-B. *Nat. Chem.* **2014**, *6*, 727–731.

[170] Hiura, H.; Miyazaki, T.; Kanayama, T. *Phys. Rev. Lett.* **2001**, *86*, 1733–1736.

[171] Kumar, V.; Singh, A. K.; Kawazoe, Y. *Nano Lett.* **2004**, *4*, 677–681.

[172] Khanna, S.; Rao, B.; Jena, P. *Phys. Rev. Lett.* **2002**, *89*, 016803–1–016803–4.

[173] Chen, Q.; Li, W.-L.; Zhao, Y.-F.; Zhang, S.-Y.; Hu, H.-S.; Bai, H.; Li, H.-R.; Tian, W.-J.; Lu, H.-G.; Zhai, H.-J. *ACS Nano* **2014**, *9*, 754–760.

[174] Bulusu, S.; Li, X.; Wang, L.-S.; Zeng, X. C. *Proc. Natl. Acad. Sci.* **2006**, *103*, 8326–8330.

[175] Li, J.; Li, X.; Zhai, H.-J.; Wang, L.-S. *Science* **2003**, *299*, 864–867.

[176] Kim, S.-W.; Kim, M.; Lee, W. Y.; Hyeon, T. *J. Am. Chem. Soc.* **2002**, *124*, 7642–7643.

[177] Oku, T.; Nishiwaki, A.; Narita, I. *Sci. Tech. Adv. Mater.* **2004**, *5*, 635–638.

[178] Stephan, O.; Bando, Y.; Loiseau, A.; Willaime, F.; Shramchenko, N.; Tamiya, T.; Sato, T. *Appl. Phys. A Mater. Sci. Process* **1998**, *67*, 107–111.

[179] Singh, A. K.; Kumar, V.; Kawazoe, Y. *J. Phys. Chem. B* **2005**, *109*, 15187–15189.

[180] Weintraub, K. *Nature* **2013**, *495*, S14–S16.

[181] Gao, Y.; Shao, N.; Bulusu, S.; Zeng, X. C. *J. Phys. Chem. C* **2008**, *112*, 8234–8238.

[182] Chen, X.; Deng, K.; Liu, Y.; Tang, C.; Yuan, Y.; Tan, W.; Wang, X. *J. Chem. Phys.* **2008**, *129*, 094301–094301.

[183] Chen, X.; Deng, K.; Liu, Y.; Tang, C.; Yuan, Y.; Hu, F.; Wu, H.; Huang, D.; Tan, W.; Wang, X. *Chem. Phys. Lett.* **2008**, *462*, 275–279.

[184] Cao, B.; Starace, A. K.; Judd, O. H.; Jarrold, M. F. *J. Am. Chem. Soc.* **2009**, *131*, 2446–2447.

[185] Cao, B.; Starace, A. K.; Judd, O. H.; Bhattacharyya, I.; Jarrold, M. F.; López, J. M.; Aguado, A. *J. Am. Chem. Soc.* **2010**, *132*, 12906–12918.

[186] Leslie, K. L.; Shinholt, D.; Jarrold, M. F. *J. Phys. Chem. A* **2012**, *117*, 1053–1058.

[187] Leslie, K. L.; Jarrold, M. F. *J. Phys. Chem. A* **2013**, *117*, 2075–2081.

[188] Cao, B.; Starace, A. K.; Judd, O. H.; Bhattacharyya, I.; Jarrold, M. F. *J. Chem. Phys.* **2014**, *141*, 204304–1–204304–6.